Department of Physics
University of Jyväskylä
Research Report No. 14/2016

Extending Physics Potential of Large Liquid Scintillator Neutrino Detectors

by
Kai Loo

Academic Dissertation
for the Degree of
Doctor of Philosophy

To be presented, by permission of the
Faculty of Mathematics and Natural Sciences
of the University of Jyväskylä,
for public examination in Auditorium FYS 1 of the
University of Jyväskylä on 16th December, 2016
at 12 o'clock noon

Jyväskylä, Finland
December 2016

Preface

The work presented in this theses has been carried out at the Department of Physics of University of Jyväskylä as a contribution to the pan-European LAGUNA and LAGUNA-LBNO Desing Studies during the years 20010 to 2014.

First I would first address my gratitude to my supervisors Doc. Wladyslaw Trzaska and Professor Jukka Maalampi for the guidance and for giving me an opportunity to work in rapidly developing international project. All the work, I have done, has been team work. I want to thank Prof. Michael Wurm for steering the liquid scintillator physics working group within the LAGUNA-LBNO project and all the members of that group, especially Dr. Dominikus Hellgartner, Dr. Randolph Möllenberg, Dr. Björn Wonsak and Dr. Sebastian Lorenz, being my closest collaborators. I would also like to express my gratitude to Prof. emeritus Franz von Feilitzch, Prof. Lothar Oberauer, Prof. Achim Stahl and Prof. Caren Hagner for sharing their expertise and support for the liquid scintillator working group.

The local team, the underground physics research group in Pyhäsalmi, deserves to be acknowledged as well. The Pyhšalmi mine has offered an extraordinary environment to widen my scientific perspective, to conduct some practical work where the progress is clearly visible, and work in totally different "laboratory" conditions compared to any other laboratory I know. Especially, I want to thank Dr. Timo Enqvist organising the first funding at the beginning of my doctoral studies and steering me towards the scientific carrier. To the group members Mr. Maciej Slupecki, Mr. Tuomo Kalliokoski, Mr. Jukka Sorjonen from University of Jyväskylä, Dr. Pasi Kuusiniemi, Dr. Tomi Räihä, Dr. Juho Sarkamo and Mr. Jari Joutsenvaara, Ms. Katja Mankinen, from University of Oulu and Mr. Antto Virkajärvi from Lappeeranta Technical University, it has been pleasure to work, but also spend free time, with the people like you. I want also express my gratitude to Dr. Marko Aittola and Mrs. Johanna Kutuniva, especially for all the discussions during the darkest hours of the nights, but also for the efforts they have made during the LAGUNA project.

I would like to thank our Russian collaborators, especially Dr. Leonid Bezrukov, Dr. Bayarto Lubsandorzhiev and Dr. Lev Inzhechik for their ideas and valuable contributions to the EMMA experiment and the upcoming C14 experiment in the Pyhäsalmi mine and the Muon Monitor experiment in Canfranc laboratory in Spain, as well as, Prof. Yuri Novikov and Dr. Mikhail Smirnov for our effort on neutrino oscillometry studies.

Finally, I would like to thank my parents for all the support and encouragement throughout my life and my friends, especially Mr. Jari Karjalainen, Mrs. Anna-Kaisa Tuomaala, Mr. Jukka Luomajoki and Mr. Teemu Nyländen for reminding me every now and then, that there might be life outside the office.

Jyväskylä, December 2016

Kai Loo

Author

Kai Loo
Department of Physics
University of Jyväskylä
Finland

Supervisors

Dr. Wladyslaw Trzaska
Department of Physics
University of Jyväskylä
Finland

Prof. Jukka Maalampi
Department of Physics
University of Jyväskylä
Finland

Reviewers

Prof. Dr. Livia Ludhova
III. Physikalisches Institut B
RWTH Aachen University
Germany

Dr. Sandra Zavatarelli
Instituto Nazionale di Fisica Nucleare-
Sezione di Genova
Italy

Opponent

Prof. Seon-Hee Seo
Department of Physics and Astronomy
Seoul National University
Korea

Acknowledgements

This work has been supported by EU within the FP7 Design Studies LAGUNA (Grant Agreement No. 212343 FP7-INFRA-2007-1) and LAGUNA-LBNO (Grant Agreement No. 284518 FP7- INFRA-2011-1). The author of this work expresses gratitude for the financial support from the Jenny and Antti Wihuri Foundation and the rector of the University of Jyväskylä. The Graduate School in Particle and Nuclear Physics (GRASPANP), Magnus Ehrnrooth Foudation and Kerttu Saalasti Foundation is acknowledged for financing the travelling to various conferences and schools. The CSC IT Center for Science in Espoo, Finland is acknowledged for allocation of sufficient computing resources.

Contents

List of Tables

List of Figures

1. Introduction

In recent years the field of the experimental neutrino physics has developed extremely rapidly. At the beginning of the studies reported in this thesis, the liquid scintillator detector LENA (Low Energy Neutrino Astronomy) [1] was considered the strongest candidate for the large next-generation neutrino detector in Europe. Since that time, the measurement of non-zero and relatively large neutrino mixing angle θ_{13} made it possible to probe CP-violation with neutrino oscillation experiments. The proper measurement of the CP-violation phase requires the determination of neutrino mass hierarchy and the value and octant of the mixing angle θ_{23} which still remain unknown.

The development, described above, has lead to many different proposals to measure the mass hierarchy. Among these are the medium baseline reactor experiment with liquid scintillator technique (JUNO [2]) in China, which is under construction, and the long-baseline neutrino beam program utilising liquid Argon technique at Fermilab, called DUNE [3], initiated recently. The neutrino oscillation experiment with sufficiently long baseline can be sensitive to both neutrino mass hierarchy and the CP-violation phase. This development has not diminished the importance of the next-generation neutrino telescope observing the neutrinos coming from the astrophysical or terrestrial sources and the studies related to physics potential or construction of such detector are still valid and utilisable in the future. The present work evaluates selected aspects of the physics performance of a large, liquid scintillator-based neutrino observatory of the next generation.

LENA would be a multipurpose detector with 50 kiloton fiducial mass of liquid scintillator aimed mainly for the studies related to low-energy neutrinos. The best performance is reached in the energy region from couple of hundreds of keV up to few hundreds of MeV. This energy range is well suited for studies related to astrophysical sources like solar and supernova neutrinos, especially diffuse supernova neutrino background, and the geoneutrinos. Although the main motivation of LENA is to observe neutrinos coming from these kinds of natural sources, it would also have the sensitivity to probe the fundamental neutrino physics topics, like the mass hierarchy, CP-violation or the existence of sterile neutrinos by using neutrinos coming from the accelerators or high-intensity radioactive sources.

The performance of LENA on various physical phenomena have been studied in context of LAGUNA and LAGUNA-LBNO Design Studies between 2008-2014 [4].The

main goal of the design studies was to find the best location and detector technology combination to cover as large physics potential as possible for the next-generation neutrino observatory inside Europe. The LENA was the low-energy candidate in the program. The other technologies considered were the water-Cherenkov detector (MEMPHYS) [5] and the liquid Argon time projection chamber (GLACIER) [6]. The feasibility of seven possible locations, including road tunnels and mines inside the Europe to host one or more gigantic detector setups were performed. Due to the excellent infrastructure and rock conditions, and the relatively low reactor neutrino background level, the preferred location for LENA is the Pyhäsalmi mine in Finland.

During the doctoral studies (2010-2015), the author has contributed to various studies related to the physics potential and background evaluations of the LENA experiment within the both LAGUNA Design Studies (Part III). The major topics of the work can be summarised as the following:

- The neutrinos emitted from the nuclear reactors cause unavoidable background signal for geoneutrino measurement. The author has independently evaluated the reactor neutrino background level for all the LAGUNA sites with the current status of reactors in the world. The impact to the geoneutrino measurements with LENA at the Pyhäsalmi mine has been evaluated, taking into account the new reactor to be constructed at the distance of 130 km from the Pyhäsalmi mine.

- From the point of view of the fundamental neutrino physics, author has participated in the studies related to the mass hierarchy and CP-violation determination capability of the LENA with the high-energy neutrino beam from CERN to Pyhäsalmi mine. The work was related to the detector performance simulations of LENA for the high-energy neutrino interactions in energy range of 1-10 GeV. The mass hierarchy determination relies on the identification of the interacting neutrino flavor and its energy. An algorithm to look for the light emission inside the detector (rudimentary tracking) has been developed and its performance for the particle flavor determination has been evaluated.

- During the LAGUNA-LBNO it became clear that the sensitivity of LENA to probe the CP-violation would be limited, mainly due to background rejection capability. The focus shifted to the low-energy solution of using several cyclotrons producing pion decay-at-rest neutrino beam with LENA to probe the CP-violation. The author has verified the calculations of the Daeδalus collaboration with the recent detector performance parameters of LENA.

- Recently updated results of the neutrino production at nuclear reactors have again livened the discussion about the additional sterile neutrino flavor(s), risen earlier from the discrepancies between expected and observed neutrino events in the source calibrations of Gallium-based solar neutrino experiments

SAGE [7] and Gallex [8] and the controversial results from accelerator neutrino experiments LSND [9] and MiniBooNE [10]. Taking as an assumption the 3+1 neutrino flavor scenario, the author has evaluated the potential to measure the parameters, mixing angle and mass squared difference with man-made radioactive sources following the baseline design of LENA experiment.

- In addition to the previous, the author has contributed to the issues related to technical design of LENA, for instance the possible top muon veto and deck structure. These issues are beyond the scope of this thesis.

The majority of the work presented in this thesis has originally appeared as a part of the following publications and conference proceedings and presentations

K. Loo *et al.*, Reactor neutrino background at the proposed LAGUNA sites Nucl.Phys.Proc.Suppl. 229-232 (2012) 518. XXIV International Conference of Neutrino Physics and Astrophysics (Neutrino 2010), Athens

K. Loo *et al.*, Hunt for Theta(13) with LENA, J.Phys.Conf.Ser. 375 (2012) 042053, 12th International Conference on Topics in Astroparticle and Underground Physics (TAUP 2011), Munich

M. Wurm *et al.* [LENA Collaboration], The next-generation liquid-scintillator neutrino observatory LENA, Astropart.Phys. 35 (2012) 685-732

K. Loo on behalf of LENA Collaboration, "LENA as a far detector for neutrino beams" (poster), XXV International Conference of Neutrino Physics and Astrophysics (Neutrino 2012), Kyoto.

K. Loo on behalf of LENA Collaboration, Event reconstruction of high-energy neutrino interactions in large liquid scintillator detectors (poster) XXVI International Conference of Neutrino Physics and Astrophysics (Neutrino 2014), Boston.

K. Loo on behalf of LENA Collaboration, Neutrino Flavor Sensitivity of Large Liquid Scintillator Detectors, Phys.Procedia 61 (2015) 488-494, 13th International Conference on Topics in Astroparticle and Underground Physics (TAUP 2013), Asilomar

M.V. Smirnov, K.K. Loo, Yu.N. Novikov, W.H. Trzaska, M. Wurm, A search for neutrino-antineutrino mass inequality by means of sterile neutrino oscillometry, Nucl. Phys. B 900 104, 2015

K.K. Loo, Yu.N.Novikov, M.V. Smirnov, W.H. Trzaska, and M. Wurm, Omnibus experiment: CPT and CP violation with sterile neutrinos, Journal of Physics: Conference Series 718 (2016) 062063, 14th International Conference on Topics in Astroparticle and Underground Physics (TAUP 2015), Torino.

In addition, the results of the present work has been presented in the Annual Conferences of the Finnish Physical Society and various LAGUNA/LAGUNA-LBNO General Meetings throughout the years 2010-2015. The complete list of the publications and presentations is given in appendix A.

The first part (Part I) of thesis starts with the short introduction to the neutrinos in Standard Model of particle physics (Chapter 2), followed by the descriptions of different kinds of sources of neutrinos (Chapter 3). The basic formalism of the neutrino oscillation phenomena accompanied by the experimental approaches to probe neutrino mass hierarchy, CP-violation phase and sterile neutrino flavors with oscillation experiments is introduced in Chapter 4.

The Part II of the thesis is dedicated to the liquid scintillator technique. The Chapter 5 covers the basic principle of neutrino detection, particle interactions and gives examples and outlook of the liquid scintillator technique in neutrino physics. After that the LENA-project is briefly introduced in Chapter 6 including the baseline design of the detector and the proposed physics programme. Last section in this chapter briefly describes the simulation environment developed mainly during the LAGUNA design studies and the most relevant results on the detector response which forms the basis of the results described in Part III.

The Part III covers the studies, in which the author have contributed the most. The reactor neutrino background levels of the proposed LAGUNA sites and especially the future situation in the Pyhäsalmi site are covered in Chapter 7. The effect of the reactor neutrino background to the geoneutrino measurement in Pyhäsalmi mine is discussed in Chapter 8. The Chapter 9 introduces the experimental scheme to look for the sterile neutrino flavors and the sensitivities for the parameters governing the oscillation assuming 3+1 scenario are reported.

When the neutrino mass hierarchy is studied with high-energy neutrinos, the flavor discrimination is one of the key issues. In Chapter 10 an attempt to define rudimentary event topology with the so-called backtracking algorithm is described and it is applied to the flavor determination is reported in the case of simple event topologies resembling the quasi-elastic scattering events. Finally, the Chapter 11 discusses the low-energy method of probing CP-violation phase. Instead of utilising the high-energy neutrino beam the neutrinos from pion decay-at-rest beams are used. The results to verify the calculations by Daeδalus collaboration in the context of LENA are presented.

The last chapter summarises the work presented in this thesis and discusses the future prospects for that to the upcoming experiments utilising the liquid scintillator technique.

Part I.

Physics & Phenomenology

2. Neutrinos in Standard Model

The concept of neutrino dates back to the 1930, when Wolfgang Pauli introduced it as a solution to the energy and spin conservation dilemma in β-decay process [11]. The theory was developed further by Enrico Fermi and by 1934 he included the massless and chargeless neutrino in the theory of weak interactions [12]. This development led to the possibility of neutrino detection followed by the first observation by F. Reines and C. Cowan in 1956 [13]. Later on, the construction of the models describing the properties and behaviour of neutrinos have challenged the particle physicists. In this chapter the basic properties and interactions of neutrinos are illustrated.

2.1. Standard Model of Particle Physics

The Standard Model (SM) is the theory that classifies the known elementary particles and their interactions. The spin-1/2 particles in the theory are quarks (u, d, c, s, t, b) and leptons $(e, \mu, \tau, \nu_e, \nu_\mu, \nu_\tau)$, which are considered as the building blocks of the matter. Between these particles there are three interactions: electromagnetic, strong and weak interaction mediated by the force carrier particles (gauge bosons): photon (γ) for electromagnetic, gluons for strong and intermediate vector bosons (W^+, W^-, Z_0) for weak interaction. In addition there is at least one scalar boson (Higgs boson) which gives the mass for the fermions.

The Standard Model is a quantum field theory based on the $SU(3)_c \times SU(2)_L \times U(1)_Y$ gauge symmetry. The charged weak interactions (observed in e.g. β decays) are associated with the $SU(2)$ symmetry generated by the weak isospin. However, to describe the structure of the weak interactions properly requires the extension of the gauge symmetry to $SU(2)_L \times U(1)$, as is done in the so-called electroweak theory of Weinberg and Salam [14] [15], which combines the weak and electromagnetic interactions. In order the theory to be consistent with the observed short range of weak interactions, the $SU(2) \times U(1)$ symmetry is broken spontaneously so that the mediators of the weak interactions, the W and Z bosons, get a mass. The spontaneous breaking is arranged with the Higgs mechanism [16] [17] [18]. That breaks the $SU(2) \times U(1)$ symmetry to $U(1)_{\mathrm{em}}$, the gauge symmetry of the electromagnetic interaction, leaving the one of the gauge bosons, the photon, massless. The $SU(3)_c$ part of the gauge symmetry is associated with strong interactions, and is the basis of the theory known as quantum chromodynamics (QCD).

The weak interactions have been observed to break the parity symmetry, so that the left-handed chiral component of the leptons and quarks have charged weak interactions, i.e. only couples to the W boson. This means that all right-handed fermions are singlets under the $SU(2)_L$ symmetry while the left-handed fermions transform non-trivially. In electroweak theory the left-handed fermions are arranged in doublet representations of $SU(2)_L$, for example leptons appear in the doublet

$$\begin{pmatrix} \nu_{lL} \\ l_L^- \end{pmatrix}, \ (l = e, \mu, \tau). \tag{2.1}$$

It has also been observed that in processes, where parity is broken, also the charge conjugation symmetry breaks, while the combined CP-symmetry seems to hold in most of the them. Curiously enough, the CP violation has been observed so far only in quark interactions [19] [20] [21]. One of the goals of the future neutrino experiments is to detect CP violation also in lepton sector.

2.2. Neutrinos

In the Standard Model (SM) neutrinos are massless and Goldhaberchargeless particles which interact solely via weak interaction. The mediators of the weak interaction, $W^{\pm}$ and Z^0, couple only to left-handed neutrinos or right-handed antineutrinos. Hence, the neutrino (antineutrino) is always purely left-handed (right-handed) and right-handed neutrinos (left-handed antineutrinos) are actually not supposed to exist in the framework of the SM.

The neutrino helicity was determined by the Goldhaber *et al.* in 1958 [22]. The helicity turned out to be negative, or H=-1, if the neutrino mass was assumed to be zero. A helicity -1 state has left-handed chirality, as a massless particle moves with the velocity of light, neutrino if massless, stays left-handed in every frame of reference. Hence, if there existed right-handed massless neutrinos they would be totally separated from the left-handed ones. However, the observation of neutrino oscillations (Super-Kamiokande [23]) implies that the neutrinos do have mass, albeit small. This indicates that right-handed neutrinos should exist, as any mass term flips the chirality of the neutrino.

To generate neutrino mass, the minimal Standard Model must be extended. Two mass schemes are possible, Dirac and Majorana scheme. In the Dirac scheme the right-handed neutrino is added into the theory to allow the mass term $\bar{\nu}_R \nu_L$. In this case the neutrinos obtain their masses via usual Higgs mechanism, similarly as the other fermions. A problem in this scenario is that right-handed neutrinos have not yet been observed. In the Majorana scheme, the mass term has the form $\bar{\nu}_R^C \nu_L$. This mass term is possible for neutral fermions. The origin of Majorana mass

term is not directly connected with the standard Higgs boson and the mass scale (m $\sim m_{q,l}$) related to it, but with the beyond SM physics and a mass scale M much larger than m. The existence of two widely different mass scales offers an explanation for the lightness of neutrinos allowing $m_\nu \sim m^2/M << m$ (the so-called see-saw mechanism [24]).

All three neutrino flavors (ν_e, ν_μ, ν_τ) have been experimentally confirmed to exist. The electron antineutrino was observed by F. Reines and C. Cowan in 1956 [13]. They used nuclear reactor (Savannah River) as a source of neutrinos and observed expected delayed coincidence signals from the antineutrino interaction on proton ($\bar{\nu}_e + p \rightarrow n + e^+$). In 1962 the other kind of neutrino, ν_μ appearing along with muons, was observed in Brookhaven National Laboratory [25]. Much more recently, in 2000, the third neutrino, related to tau, ν_τ was observed by the DONUT collaboration in Fermilab [26].

The total number of light neutrino species can be measured in collider experiments with the SM interactions. The LEP experiment showed that the number of light neutrino species is 3 ($N_\nu = 2.984 \pm 0.008$.) [27]. In cosmology, the recent analysis of the Planck satellite data set the effective number of neutrinos to $N_{\text{eff}} = 3.15 \pm 0.23$ [28] and that is compatible with 3 neutrino species.

As the interactions of neutrinos with matter are very weak, they can travel long distances undisturbed and carry information of their birth processes and environment in distant objects in space. For example, stars emit great amount of neutrinos originating from the fusion processes, in core-collapse supernovae the most of the gravitational binding energy is released in the form of neutrinos. The β-radioactivity also has a role in the heat flux driving the plate tectonics inside the Earth. Neutrinos also played a crucial role in the early universe e.g. by affecting the creation of light elements.

2.3. Neutrino Interactions

2.3.1. Weak Interactions

The theory of weak interactions developed by Fermi [12], resembles the theory of electromagnetic interaction. The interactions were presented in terms of currents. Fermi's goal was to explain the interaction behind the beta decay in terms of hadron current involving the proton (p), and the neutron (n) and lepton current involving the electron (e) and the electron neutrino (ν_e). The interaction happens in one point (contact interaction), and the Hamiltonian is expressed as a product of the two

currents

$$\mathcal{H}_{\text{weak}} = \frac{G_F}{\sqrt{2}} \bar{\psi}_p \gamma_\mu \psi_n \bar{\psi}_e \gamma^\mu \psi_{\nu_e}. \tag{2.2}$$

Here $G_F = 1.166 \cdot 10^{-5} \text{GeV}^{-2}$ is called the Fermi coupling constant and, it describes the strength of the interaction.

The weak interactions differ from the electromagnetic interactions in that there a particle can transform to another particle. The mediators of the weak interaction (charged W^+, W^- and neutral Z^0) are called intermediating vector bosons. The reactions which happen by exchanging $W^\pm$ bosons are called charged current (CC) interactions shown in Figure 2.2, and by exchanging Z^0 as neutral current (NC) interactions as depicted in Figure 2.3. In charged current interactions the electric charge is transferred and the final state particles are different compared to initial state particles. In neutral current interactions the particle flavor does not change. Intermediate vector bosons are heavy ($m_W \approx 80.4$ GeV, $m_Z \approx 91.2$ GeV) and hence the range of weak interactions is short.

The Fermi theory is an effective theory applicable only at low energies. In the SM, which is valid in all energies, the interactions are presented in terms of gauge bosons intermediate between fermion currents. The four-fermion Fermi coupling depicted in Figure 2.1 is replaced in the SM by the W-mediated interaction between a du quark current and $\nu_e e$ lepton current depicted in Figure 2.2.

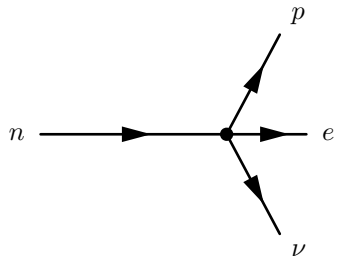

Figure 2.1.: The Feyman diagram of the β-decay of the Fermi's theory (point interaction)

The effective low-energy Hamiltonian of weak interactions can be written in the form

$$\mathcal{H}_{\text{weak}} = \frac{4G_F}{\sqrt{2}} [J^\mu(x) J^\dagger_\mu(x) + \rho K^\mu(x) K_\mu(x)], \tag{2.3}$$

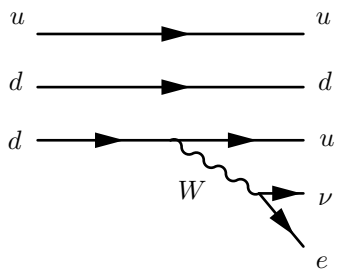

Figure 2.2.: The Feyman diagram of β decay.

where $G_F = g^2/8M_W^2$ (g is the gauge coupling constant associated with $SU(2)_L$ and

$$J_\mu(x) = \bar{u}\gamma_\mu LVd + \bar{\nu}\gamma_\mu Ll \tag{2.4}$$

$$K_\mu(x) = \sum_q [\epsilon_L(q)\bar{q}\gamma_\mu Lq + \epsilon_R(q)\bar{q}\gamma_\mu Rq]$$

$$+\frac{1}{2}\sum_\nu \bar{\nu}\gamma_\mu L\nu + \frac{1}{2}\sum_l \bar{l}\gamma_\mu[g_V(l) - \gamma_5 g_A(l)]l \tag{2.5}$$

are the charged and neutral weak currents respectively. The g_V and g_A are the coupling constants for vector and axial vector currents and

$$L = \frac{1}{2}(1-\gamma_5), \quad R = \tfrac{1}{2}(1-\gamma_5) \tag{2.6}$$

are the projection operators. We have denoted

$$u = \begin{pmatrix} u \\ c \\ t \end{pmatrix}, d = \begin{pmatrix} d \\ s \\ b \end{pmatrix}, \nu = \begin{pmatrix} \nu_e \\ \nu_\mu \\ \nu_\tau \end{pmatrix}, l = \begin{pmatrix} e \\ \mu \\ \tau \end{pmatrix}. \tag{2.7}$$

In the charged current J_μ, V is the CKM (Cabibbo-Kobayashi-Masakawa) matrix, which describes the mixing of the quarks.

2.3.2. Interactions of Low-energy Neutrinos

In this thesis the main emphasis is on neutrinos and their interactions with matter. In the following we will consider the neutrino interactions the most relevant for the present work.

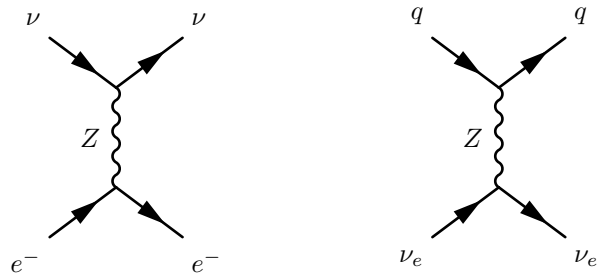

Figure 2.3.: Elastic scattering processes mediated by Z_0

Neutrino-Electron Scattering

Neutrino-electron elastic scattering

$$\nu_l + e^- \rightarrow \nu_l + e^- \ (l = e, \mu, \tau). \tag{2.8}$$

is the main channel to detect the low-energy electron neutrinos, like solar neutrinos, with liquid scintillator detector. The reaction is similar to the Compton scattering of γ rays. For ν_μ and ν_τ this process is possible via NC interactions only. For the electron neutrino ν_e also CC interaction contributes, making the cross section $\sigma(\nu_e e \rightarrow \nu_e e)$ larger than $\sigma(\nu_{\mu,\tau} e \rightarrow \nu_{\mu,\tau} e)$.

The differential cross section $d\sigma_{\nu e}/dT_e$ of neutrino-electron elastic scattering is given by

$$\frac{d\sigma_{\nu e}}{dT_e} = \frac{G_F^2 m_e}{2\pi}\left[A_0 + B_0(1 - \frac{T_e}{E_\nu})^2 + C_0\frac{m_e T_e}{E_\nu^2}\right], \tag{2.9}$$

where T_e is the kinetic energy of the electron and

$$A_0 = (g_V + g_A)^2, B_0 = (g_V - g_A)^2, C_0 = g_A^2 - g_V^2 \tag{2.10}$$

$$g_V = 2\sin^2\theta_W + 1/2, g_A = +1/2 \text{ for } \nu_e \tag{2.11}$$

$$g_V = 2\sin^2\theta_W - 1/2, g_A = -1/2 \text{ for } \nu_\mu \text{ and } \nu_\tau, \tag{2.12}$$

where θ_W is the Weinberg angle.

Due to the kinematics of the reaction in Equation 2.8, the maximum kinetic energy for the recoil electron is

$$T_{max} = \frac{E_\nu}{1 + m_e/2E_\nu} \tag{2.13}$$

For neutrino energies $E_\nu >> m_e$, the total cross section can be approximated as:

$$\sigma_{\nu_e} = 9.2 \cdot 10^{-45} \frac{E_\nu}{\text{MeV}} \text{cm}^2 \tag{2.14}$$

$$\sigma_{\nu_x} = 1.5 \cdot 10^{-45} \frac{E_\nu}{\text{MeV}} \text{cm}^2 \tag{2.15}$$

Neutrino-proton scattering

The elastic scattering can also occur on proton, i.e.

$$\nu_l + p \rightarrow \nu_l + p \ (l = e, \mu, \tau), \tag{2.16}$$

but since the proton mass is over three orders of magnitude larger, the recoil energy is small and the detection of such low energies would be challenging. This reaction could still give additional information at higher neutrino energies, for instance, about the muon and tau neutrino fluxes from a supernova burst.

Inverse β Decay Reaction on Proton

The inverse β-decay (IBD)

$$p + \bar{\nu}_e \rightarrow n + e^+ \tag{2.17}$$

is the main detection channel of low-energy electron antineutrinos $\bar{\nu}_e$. This is a charged current (CC) process with threshold energy of 1.806 MeV. The cross section is given by

$$\sigma(E_e) = \kappa p_e E_e (1 + \delta_{\text{rec}} + \delta_{\text{wm}} + \delta_{\text{rad}}), \tag{2.18}$$

where p_e is the momentum and E_e the energy of the positron and δ_{rec}, δ_{wm} and δ_{rad} the energy dependent neutron recoil as the nucleon is not infinitely heavy, weak magnetism from the parity violating interference between the weak magnetic moment of a nucleon and its axial current, and radiative corrections respectively. These corrections decrease the total cross section by 2% [29]. The factor κ stands for

$$\kappa = \frac{2\pi^2}{m_e^5 f^R \tau_n} \approx 9.52 \times 10^{-44} \text{cm}^2, \tag{2.19}$$

where τ_n is the neutron mean lifetime, and $f^R = 1.71465$ is the phase-space factor for β-decay of a free neutron taken. The relation between the positron energy and neutrino energy is given by

$$E_\nu = E_e + \Delta + \frac{E_e(E_e + \Delta)}{M} + \frac{1}{2}\frac{(\Delta^2 - m_e^2)}{M} \tag{2.20}$$

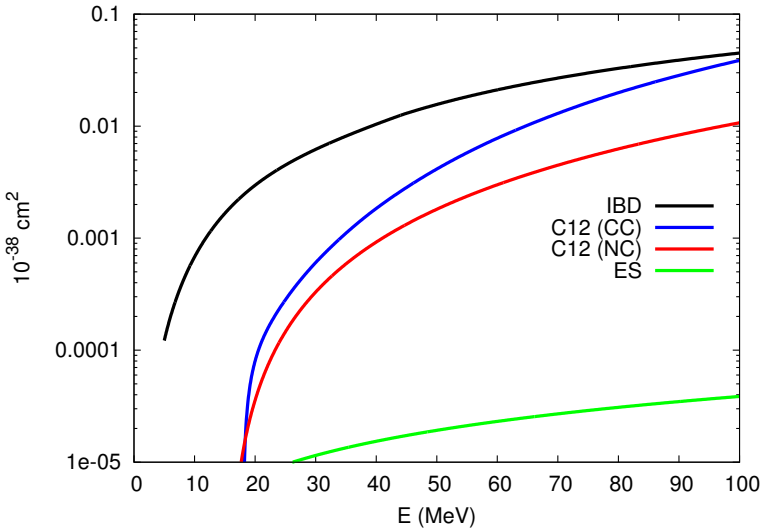

Figure 2.4.: Cross sections for different electron antineutrino interactions as a function of neutrino energy (E). Plotted are the cross sections for Inverse β-decay (IBD), charged current and neutral current interactions with ^{12}C and elastic scattering (ES) on electrons.

where $\Delta = m_n - m_p$ and M is the proton mass.

In the computer simulations performed in this work the IBD cross section was approximated by

$$\sigma_{IBD}(E_\nu) = 9.52 \times (E_\nu - 1.29)^2 \times 10^{-44} \text{ cm}^2, \tag{2.21}$$

where E_ν is the energy of neutrino expressed in units MeV.

Compared to the interactions of electron antineutrino on carbon or electron, the IBD has cross section considerably larger at low energies (< 100 MeV) as shown in Figure 2.4. This makes IBD the golden channel for detecting electron antineutrinos. The IBD is the main detection channel for geoneutrinos, reactor neutrinos, and diffuse supernova background neutrinos, as well as, for the low-energy sterile neutrinos in liquid scintillators.

Reactions on Carbon

For higher energy neutrinos also reactions with carbon become possible. The following CC and NC scatterings with ^{12}C are relevant:

$$^{12}\mathrm{C} + \nu_\mathrm{e} \rightarrow ^{12}\mathrm{N} + \mathrm{e}^- \quad (17.34\ \mathrm{MeV}) \tag{2.22}$$
$$^{12}\mathrm{C} + \bar{\nu}_\mathrm{e} \rightarrow ^{12}\mathrm{B} + \mathrm{e}^+ \quad (13.37\ \mathrm{MeV}) \tag{2.23}$$
$$^{12}\mathrm{C} + \nu_\mathrm{l} \rightarrow ^{12}\mathrm{C}^* + \nu_\mathrm{l} \quad (15.11\ \mathrm{MeV}) \tag{2.24}$$
$$^{12}\mathrm{C} + \bar{\nu}_\mathrm{l} \rightarrow ^{12}\mathrm{C}^* + \bar{\nu}_\mathrm{l} \quad (15.11\ \mathrm{MeV}) \tag{2.25}$$

The threshold energies of these reactions are rather high and the cross sections are roughly one to two orders of magnitudes lower than that of IBD reaction. Nevertheless, in the first and the second reaction the subsequent final state nuclei decays of ^{12}N via β^+ ($\mathrm{T}_{1/2} = 11.0$ ms) and ^{12}B via β^- ($\mathrm{T}_{1/2} = 20.2$ ms) may offer the delayed coincidence signature and could be used in case of supernova neutrinos. In the two last reactions the exited carbon deexcites by gamma emission.

As the organic scintillator is made of natural carbon that contains 1% of ^{13}C isotope, the following reactions are possible:

$$^{13}\mathrm{C} + \nu_\mathrm{e} \rightarrow ^{13}\mathrm{N} + \mathrm{e}^- \tag{2.26}$$
$$^{13}\mathrm{C} + \nu_\mathrm{l} \rightarrow ^{13}\mathrm{C}^* + \nu_\mathrm{l} \tag{2.27}$$
$$\tag{2.28}$$

In the first reaction the produced radioactive isotope ^{13}N decays via β^+ with rather long half-life of $\mathrm{T}_{1/2} = 862$s. The low threshold energies of these reactions 2.22 MeV and 3.68 MeV respectively make these reactions interesting. This makes possible to use the first reaction to probe solar ^{8}B neutrinos and low-energy neutrinos from supernovae [30].

2.3.3. Interactions of High-Energy Neutrinos

The CC reactions that are important in detecting neutrinos in the energy range from 1 GeV to 10 GeV include quasi-elastic scatterings (QEL)

$$\nu_\mu + n \rightarrow p + \mu^- \quad \text{and} \quad \bar{\nu}_\mu + p \rightarrow n + \mu^+ \tag{2.29}$$
$$\nu_e + n \rightarrow p + e^- \quad \text{and} \quad \bar{\nu}_e + p \rightarrow n + e^+, \tag{2.30}$$

the resonant pion production reactions (RES), for example

$$\nu_\mu + n \rightarrow \Delta^+ + \mu^- \rightarrow p + \pi^0 + \mu^-, \tag{2.31}$$

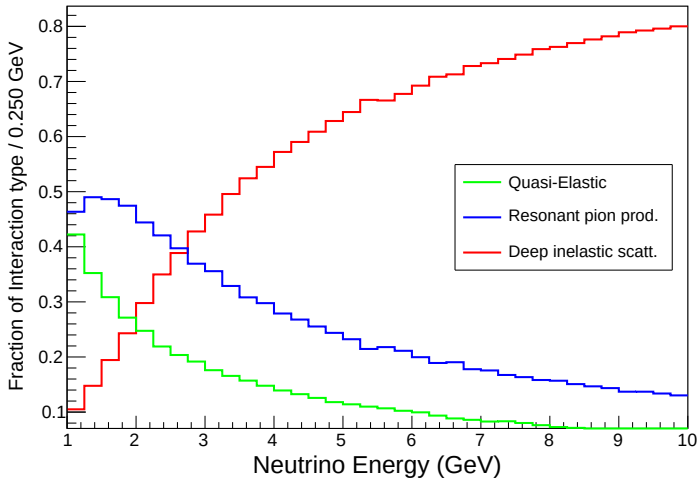

Figure 2.5.: The fractions of different neutrino interaction categories (QEL, RES,DIS) in Linear-alkyl-benzene (LAB, $C_{18}H_{30}$) in the energy range relevant to high-energy neutrino beam.

and the deep inelastic scatterings (DIS) which at these energies are essentially a multipion processes (N_π is the number of pions)

$$\nu_\mu + n \to p + N_\pi \pi + \mu^-. \tag{2.32}$$

In addition, there are neutral current (NC) interactions with similar kind of signatures except that the final state charged leptons are replaced by the neutrino. The quasi-elastic interactions (QEL) dominate at lower energies, the resonant pion production (RES) - at energies $\sim$ 2 GeV and deeply inelastic scatterings (DIS) above - 3 GeV. The fractions of these interaction types with respect to energy are depicted in Figure 2.5 for the linear-alkyl-benzene scintillator. The high-energy interactions are important in the measurement of atmospheric neutrinos whose energy ranges from tens of MeV to several GeV and different kinds of high-energy beam neutrinos whose energy ranges from several hundreds of MeV to tens of GeV depending on the physics goal. The indirect search of dark matter from by detecting neutrinos produced in the annihilations of dark matter particles in the centre of the Sun also belongs to this high-energy neutrino region.

3. Sources of Neutrinos

The large-scale neutrino detectors considered in this thesis are planned to detect neutrinos from many different natural sources as well as man-made neutrinos from particle accelerators and nuclear reactors. In this chapter an overview is made on these different neutrino sources and the prospects of using them in the next-generation experiments. The ordering of the presentation follows roughly the energies of produced neutrinos. Figure 3.1 presents the energy spectrum of neutrinos produced in a variety of sources, showing the wide energy range they cover.

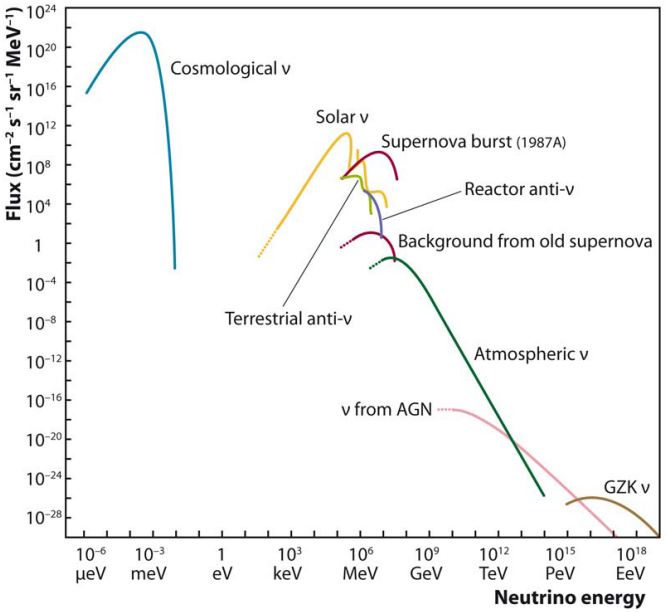

Figure 3.1.: The energy ranges and intensities of the neutrinos from natural sources.[1]

[1] http://www.aspera-eu.org/images/stories/files/Roadmap.pdf

3.1. Radioactive Decays

Without a need of external energy the neutrinos are produced in radioactive decay processes of β^--decay, β^+-decay, also called the positron emission, and the electron capture (EC):

$$n \rightarrow p + e^- + \bar{\nu}_e, \tag{3.1}$$

$$p \rightarrow n + e^+ + \nu_e, \tag{3.2}$$

$$p + e^- \rightarrow n + \nu_e. \tag{3.3}$$

Due to the lepton number conservation, neutrinos originating from these natural processes are electron neutrinos. Their energies ranges from keV to several MeV. In the case of β-decays, the energy spectrum is continuous and goes up to the endpoint energy (Q-value) of the decay. In electron capture processes, with two particles in final state, mono-energetic electron neutrinos are produced.

The processes (3.1)-(3.3) are relevant for production of geoneutrinos and high-intensity radioactive neutrino sources, which belongs to the scope of this thesis. Geoneutrinos are produced by the isotopes, most important being the ones from the decay chains of ^{238}U and ^{232}Th, present in Earth's crust and mantle. High-intensity radioactive sources are produced usually by neutron bombardment in nuclear reactor. Both of the sources are discussed more thoroughly in later chapters; geoneutrinos in Chapter 8 and high intensity radioactive neutrino sources in Chapter 9.

3.2. Fission and Fusion Processes

In fission a nucleus splits into lighter nuclei spontaneously or induced by other particle or nucleus. The fissile isotopes are heavy and often neutron rich. The resulting daughter nuclei are also neutron rich and emit the excess of neutrons via (chains of) β decays 3.1 where also electron antineutrinos are produced. Nuclear power reactors are for this reason high-intensity electron antineutrino sources (see Chapter 7).

Another nuclear process where neutrinos are produced is fusion. The nuclei created in a fusion are often radioactive, and when they decay through β-decay or react with other nuclei, they produce neutrinos.

A well-known example of the neutrinos originating in fusion are the solar neutrinos. They are born in the fusion processes happening at the core of the Sun. There are two fusion chains both releasing neutrinos in different stages of the chains. In context of the Sun the main energy chain is the so called pp-chain, in which hydrogen is fused to helium. The chain is illustrated in left panel of Figure 3.2. The other fuel cycle is called CNO-cycle, illustrated in right panel of Figure 3.2. This cycle has minimal

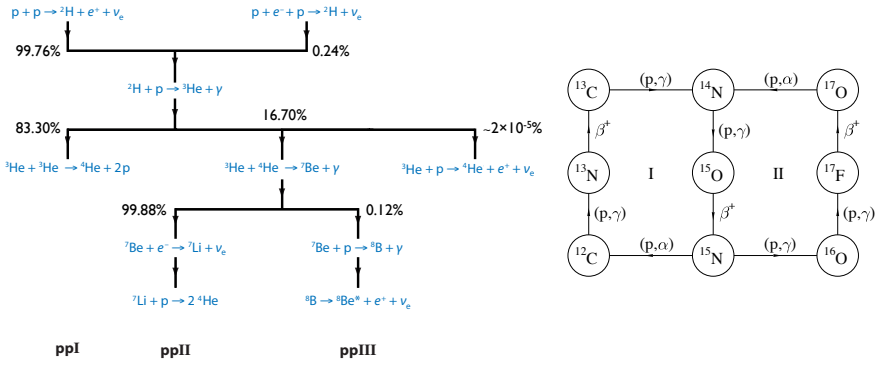

Figure 3.2.: Neutrino production in the Sun. The left panel shows the principal chains (ppI,ppII, ppIII). The right panel shows the CNO cycle. [34]

effect to the energy production in the Sun contributing only $\sim 1.5\%$, but in heavier stars this cycle has a higher importance.

As shown in Figure 3.2, the solar neutrinos are electron neutrinos by birth. Their energies are relatively small, up to ~ 18 MeV. The energy spectrum of solar neutrinos is depicted in Figure 3.3.

The pp-fusion chain results in the reaction

$$4p + 2e^- \rightarrow^4 \mathrm{He} + 2\nu_e + 26.731\mathrm{MeV}. \tag{3.4}$$

From the measured luminosity of the Sun $L_\odot = 2.4 \times 10^{39}$ MeV/s, one can predict the solar neutrino flux, which is large enough to be measured and is also measured in many experiments (Homestake [31], Kamiokande, [32], GNO [33], SAGE [7]).

3.3. Neutrinos from Astrophysical Sources

As discussed above the neutrinos and antineutrinos produced in radioactive processes have electron flavor. This is due to the fact that the energy of the process is too low as the normal matter contains only u- and d-quarks ($m_u = 2.3$ MeV, $m_d = 4.8$ MeV). Additional energy is needed to have a more massive charged lepton ($m_\mu = 105.7$ MeV, $m_\tau = 1.78$ GeV) in the final state.

The suitable conditions for production of all neutrino flavors require higher energy densities. Sufficient high densities can occur naturally in supernova explosions where the great amount of the energy is released in the form of neutrinos. Neutrinos

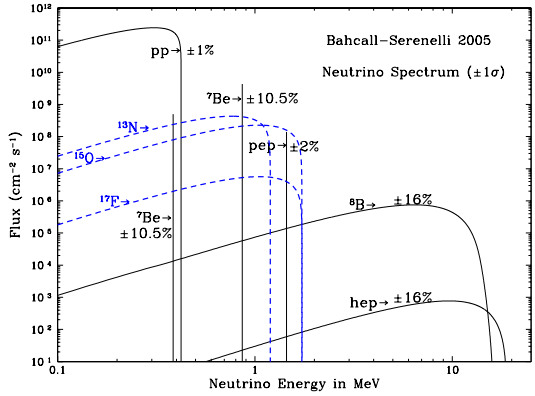

Figure 3.3.: Predicted energy spectrum of solar neutrinos. [35]

originate also from particle collisions, where the final state particles can already be neutrinos or some unstable particle, like pion, which produces neutrinos when decaying. As the decay of a particle is a two-body phenomena and the decay can occur in flight, the final state neutrino could reach high energies.

3.3.1. Supernova Neutrinos

Core-collapse supernova can happen when the electron pressure in a star ($m \leq 8m_{\odot}$) can not anymore compensate the inward gravitational pressure due to the declining fusion activity in the core of the star. The core collapses and when it reaches nuclear density, the still collapsing outer layers bounce back from the dense core and form a shock front. The bounce ejects the outer layers of the star to the surrounding space.

In the collapse phase of the core, the energy density increases and protons start to convert to neutrons by combining with electron resulting also in neutrino in the final state. This is called a neutronization burst. Neutrinos are the only particles, due to the weakness of their interactions, which can escape from this ultra dense core during the collapse phase.

After the collapse the cooling phase of the neutron star starts. Because of the high density, the neutrino-antineutrino pair production is the most efficient way to cool it down. About 99% of the gravitational binding energy of the collapsing star is released in the form of neutrinos.

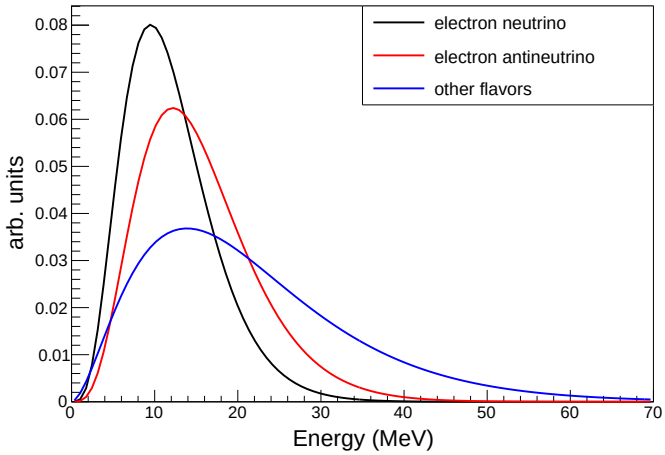

Figure 3.4.: Example of estimated energy spectra for different neutrino flavors in core-collapse supernovae. Parameterisation of Lawrence Livermore group is used. [40]

The energy spectrum of the supernova neutrinos has not yet been measured, due to the lack of supernovae sufficiently close to the Earth i.e in the Milky Way. The only detection of supernova neutrinos dates back to year 1987 when the neutrinos from the supernova SN1987A were observed in IMB, Kamiokande and Baksan neutrino detectors [36] [37] [38]. In total just 24 neutrino events were recorded, not giving any useful information about the neutrino spectra. Hence, the energy spectra of different neutrino flavors have been estimated with Monte Carlo simulations. The spectra can be parameterised in following way [39]:

$$\frac{dN_\nu}{dE_\nu} = \frac{(1+\beta_\nu)^{1+\beta_\nu} L_\nu}{\Gamma(1+\beta_\nu)\,\langle E_\nu\rangle^2} \left(\frac{E_\nu}{\langle E_\nu\rangle}\right)^{\beta_\nu} e^{-(1+\beta_\nu)E_\nu/\langle E_\nu\rangle}. \tag{3.5}$$

Here L_ν is the expected neutrino luminosity, $\langle E_\nu\rangle$ is the mean energy of the spectrum and β_ν is the shape factor. These parameters are determined with simulations. The spectra of different neutrino flavors are shown in Figure 3.4. As it is shown in the plot, energies of supernova neutrinos are in the range of 0-100 MeV. Note that in the spectra shown the oscillation effects caused by the dense core and the stellar medium through which the neutrinos traverse are not taken into account.

During the history of the Universe a countless number of supernovae collapses have taken place and as they are powerful neutrino sources, a background flux of

neutrinos from these explosions is expected. This is called diffuse supernova neutrino background (DSNB), and it has not been detected so far. The stringiest upper limit for the DSNB flux comes from the Super-Kamiokande experiment being less than 3.1 $\bar{\nu}_e$ cm^{-2}s^{-1} for $E_{\bar{\nu}_e} > 17.3$ MeV with 90% C.L. [41].

3.3.2. Atmospheric Neutrinos

The atmosphere of the Earth is constantly bombarded by high-energy particles from the outside space. These, so-called cosmic-rays, are mainly charged particles and nuclei and their composition is roughly 75% of protons, 15% of helium and 10% heavier nuclei, up to iron. Figure 3.5 shows the measured cosmic-ray energy spectrum. Indicated are also the two characteristic features of the spectrum, the knee and the ankle, the areas of abrupt change in the energy profile.

Interactions of the primary cosmic-rays with the atmosphere produce mainly pions and kaons, which produce subsequently secondary particles either via decay or via further interactions with atoms. The atmospheric neutrinos originate primarily from the pion and kaon decays. This flux of neutrinos is called conventional atmospheric neutrino flux. The neutrino producing chain of charged pions is

$$\begin{aligned} \pi^{\pm} \rightarrow \quad & \mu^{\pm} \quad + \nu_{\mu}(\bar{\nu}_{\mu}) \\ & \downarrow \\ & e^{\pm} \quad + \nu_e(\bar{\nu}_e) + \bar{\nu}_{\mu}(\nu_{\mu}) \end{aligned}$$

This process dominates over the corresponding electronic channel of pion decay. From these decays, the expected ratio between muon and electron type neutrinos is two. Corresponding neutrino producing channels are also available for kaons (with 63.4 % branching ratio):

$$K^{\pm} \rightarrow \mu^{\pm} + \nu_{\mu}(\bar{\nu}_{\mu}) \tag{3.6}$$

Also the following decay of neutral kaon produces neutrinos:

$$K_L^0 \rightarrow \pi^{\pm} + e^{\pm} + \bar{\nu}_e(\nu_e) \tag{3.7}$$

This channel has a branching ratio of 40.5%.

In addition to the conventional flux, a small amount of neutrinos can also result from the decays of charmed mesons e.g. D and B. This flux is called the prompt atmospheric neutrino flux. So far it has not been observed [43].

The spectrum of atmospheric neutrinos is defined by the interactions and decays of the pions and kaons. The critical energy ϵ is the energy at which the decay length of the particle is equal to the scale height of the atmosphere. The critical energy sets

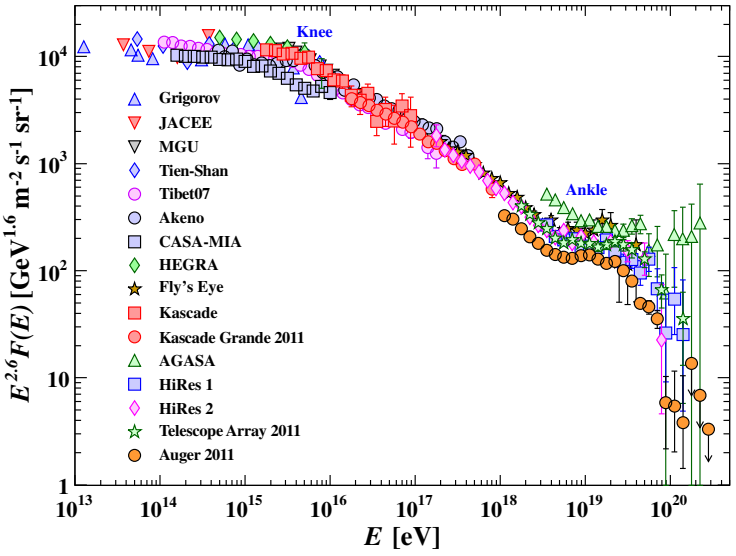

Figure 3.5.: Measured all-particle spectrum of the primary cosmic-rays [42]. The spectrum follows a power law, where $dN/dE \propto E^{-2.7}$ up to energies around 1 PeV, where it becomes steeper $dN/dE \propto E^{-3}$. This feature is called the "knee". Around 4×10^6 TeV the spectrum becomes harder again, so-called "ankle". Finally at the highest energies the spectrum is suppressed due to the interaction with the cosmic microwave photons (GZK cutoff).

Particle	ϵ (GeV)
$\mu^{\pm}$	1.0
$\pi^{\pm}$	115
$K^{\pm}$	850
K_L^0	205
$D^{\pm}$	4.3×10^7
D^0	9.2×10^7

Table 3.1.: Critical energies of various particles.

the limit above which the parent particle is more likely to interact with atmosphere than decay and this affects the energy spectrum of atmospheric neutrinos. At low energies such that $E << \epsilon/\cos\theta$, where θ is the zenith angle of the direction of the parent particle (π, K), the decay length is short and particles will decay before they have a chance to interact. The energy of neutrinos created in these decays is related to the parent particle and the spectrum follows the one of the initial cosmic-ray particle. At high energies $E >> \epsilon/\cos\theta$, the decay length becomes long and particles are likely to interact before they can decay. That leads to the energy spectrum of neutrinos typically one power steeper than that of the parent particles and primary cosmic-rays. The critical energies of particles important for atmospheric neutrinos are given in Table 3.1.

To calculate the flux and the energy spectrum of the atmospheric neutrinos more realistically, the nucleon and meson distributions containing interaction and decay lengths must be folded with the energy spectrum of neutrinos created in from meson decays. This is usually done using Monte Carlo techniques. The energy spectrum of total atmospheric neutrino flux evaluated this way are shown Figure 3.6 for three locations, Pyhäsalmi, South Pole and the planned Indian-based neutrino observatory detector site. The azimuth and zenith angle dependencies are shown in Figure 3.7 and in Figure 3.8 respectively.

3.3.3. Ultra-high Energy Neutrinos

In addition to the atmospheric neutrinos originating from cosmic-ray particle interactions with the Earth's atmosphere, the neutrinos can originate in proton interactions with matter or radiation via following pion producing reactions:

$$p + \text{nucleus} \rightarrow \pi + X, (\pi = \pi^{\pm}, \pi^0) \tag{3.8}$$

$$p + \gamma \rightarrow \Delta^+ \rightarrow \begin{cases} p + \pi^0 \\ n + \pi^+ \end{cases} . \tag{3.9}$$

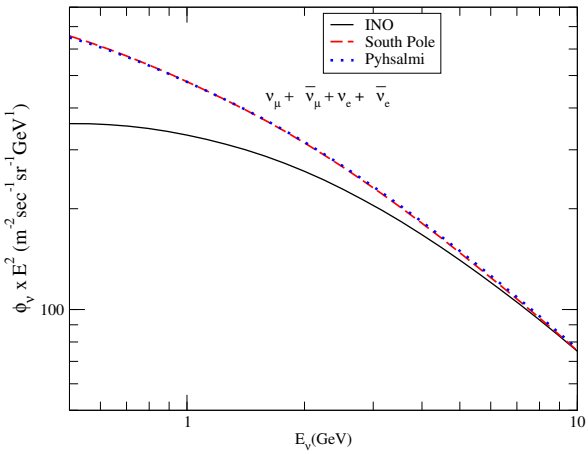

Figure 3.6.: The total atmospheric neutrino flux integrated over all zenith and azimuth angles and summed over all neutrino flavors ($\nu_\mu + \bar{\nu}_\mu + \nu_e + \bar{\nu}_e$) for the INO, South Pole and Pyhäsalmi sites. [44]

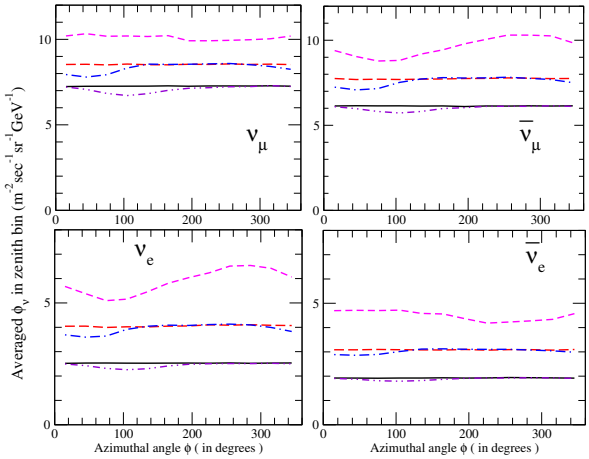

Figure 3.7.: The azimuth angle dependence of atmospheric neutrino flux, averaged over zenith angle bins of $1 > \cos\theta > 0.6$ (solid line), $0.6 > \cos\theta > 0.2$ (long dashed), $0.2 > \cos\theta > -0.2$ (short dashed), $-0.2 > \cos\theta > -0.6$(dashed-dotted), and $-0.6 > \cos\theta > -1$ (dashed double-dotted), calculated for the Pyhäsalmi site at (anti)neutrino energy E = 3.2 GeV. [44]

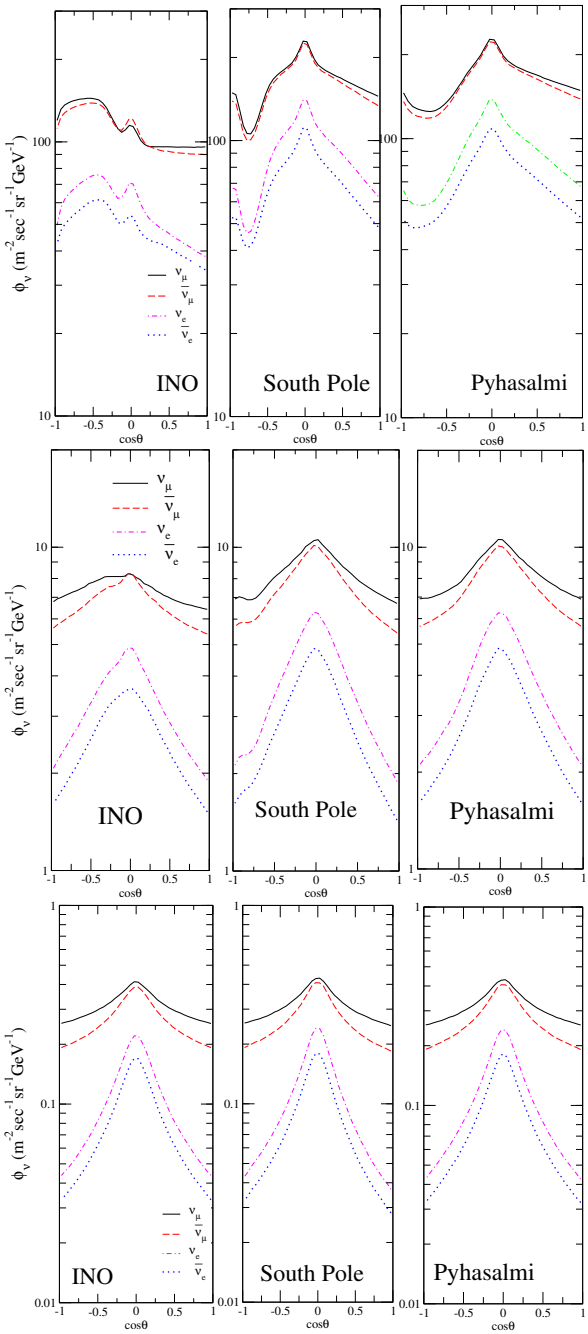

Figure 3.8.: The zenith angle dependence of atmospheric neutrino flux at E=1 GeV (upper), E=3.2 GeV (middle) and E=10GeV (lower), averaged over all azimuth angles for INO, South Pole and Pyhäsalmi sites. Here θ is the arrival direction of the neutrino, with $\cos\theta = 1$ for vertically downward going neutrinos, and $\cos\theta = -1$ for vertically upward going neutrinos. [44]

Such processes occurring in supernova remnants (SNR), active galactic nuclei (AGN) or gamma-ray bursts (GBR) can produce neutrinos with energies above PeV and form a diffuse flux on neutrinos with extra-galactic origin. The latter reaction is important also when protons interact with the cosmic microwave background (CMB) radiation producing so-called GZK-neutrinos (see Figure 3.1).

To observe the neutrinos from astrophysical sources the detector must be capable of reconstructing event energies above TeV and that requires typically 1 km^3 or larger detector volume which is not applicable to the detection technique presented in this thesis. However, the first interactions of PeV-range neutrinos have been observed in IceCube detector deployed in the antarctic ice at the South Pole. The 3.7σ evidence of astrophysical neutrino flux have been announced by observing muon neutrinos from the northern sky [45]. In addition to IceCube, there are two on-going large-scale projects to construct underwater neutrino telescopes: Gigaton Volume Detector (GVD) in Lake Baikal [46] and KM3net in the Mediterranean sea with three separate detector sites [47]

3.4. Accelerator-based Neutrino Beams

The accelerator-based neutrino production is based on the same basic particle physics processes that occur in the natural neutrino sources discussed above: the pion and kaon leptonic decay, beta decay, and muon decay. In the following the used and planned methods of the artificial neutrino beams are described.

Conventional Neutrino Beam

The so-called conventional neutrino beam is made by colliding protons on a fixed target, usually graphite. In the collisions charged pions are produced which subsequently decay via

$$\pi^+ \rightarrow \mu^+ + \nu_\mu \tag{3.10}$$

or

$$\pi^- \rightarrow \mu^- + \bar{\nu}_\mu. \tag{3.11}$$

Both muon neutrino and muon antineutrino beams can be created. Depending on which beam is needed, pions with corresponding charge are selected and directed to a decay pipe by using magnetic field in a component called magnetic horn. In the decay pipe pions decay in flight into muons and muon neutrinos as presented in Equation 3.10 and Equation 3.11. Muons and other particles are absorbed in the beam dump while neutrinos continue in the direction of the original pions. The

	Fermilab Booster	Fermilab Main Injector	J-Parc Main Ring
Proton energy (GeV)	120	120	30 (50)
Beam Power (kW)	12	(700)	400 (750)
Protons/cycle ($\times 10^{12}$)	4.5	(49)	123 (330)
Cycle time (s)	0.5	(1.333)	2.48
Peak neutrino energy (GeV)	1	2	0.6
Experiments	MicroBooNE [48] (SBL [51])	NOνA [49] MINOS+ [52] MINERνA [53] (DUNE [3])	T2K [50]

Table 3.2.: Summary of current conventional neutrino beams currently operational and the experiments they serve [42]. The values in parenthesis refers to the design values.

energies of the produced neutrinos are usually of the order of a few GeV. An example of the energy spectra is shown in Figure 3.9.

Typically the conventional beams are used in neutrino oscillation experiments and neutrino cross section studies. This was also the method used at BNL in the experiment where muon neutrino was discovered [25]. The protons were shot to a beryllium target and muon neutrino interactions producing muons were seen in a spark chamber detector. Currently there are two major accelerator centres providing conventional high-energy neutrino beams: Fermilab in US and J-Parc in Japan. Table 3.2 summarises properties of these neutrino beam lines and lists the experiments they serve.

β-beam

The concept of beta beam relies on producing and accelerating beta decaying or positron emitting isotope ions resulting a pure electron neutrino or electron antineutrino beams for $\nu_e \to \nu_\mu$ studies [55]. In practice the large amount of radioisotope ions are produced, accelerated and injected into a storage ring (decay ring), where they decay via

$$n \to p + e^- + \bar{\nu}_e \tag{3.12}$$

or

$$p \to n + e^+ + \nu_e. \tag{3.13}$$

As the neutrinos are emitted from the decay-in-fight ions, they are kinematically focused towards to direction of flight. The decay ring is constructed in such way that

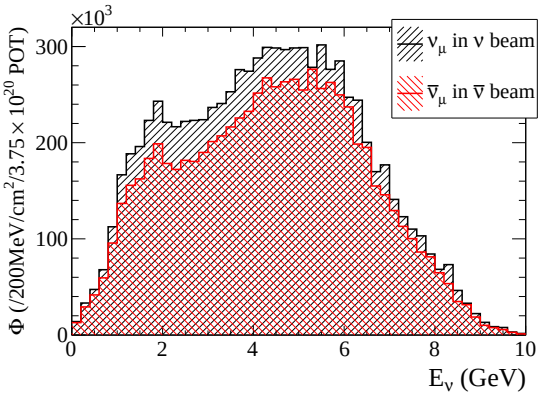

Figure 3.9.: The estimated energy spectrum of muon neutrinos for the proposed CERN to Pyhäsalmi beamline studied in the LAGUNA-LBNO design study. [54]

it contains straight sections pointing towards the detector site. The advantage of the β-beam would be the possibility to construct essentially background-free pure electron neutrino or electron antineutrino beam with well defined energy. That is important especially in long baseline neutrino experiments measuring the CP-violation phase. The resulting continuous energy spectra will peak typically at several hundreds of MeV i.e. in the neutrino energy region where the quasi-elastic scattering interaction dominates.

The conceptual design for β-beam at CERN have been conducted [56]. The schematic design of isotope production and the accelerator chain is shown in Figure 3.10. The feasible isotopes for neutrino production (^{6}He and ^{18}Ne) could be produced with isotope-separation line to be injected to the existing Proton Synchrotron (PS) and Super Proton Synchrotron (SPS) for further acceleration to high energies ($\gamma \approx 100$) and for bunching. After that the bunches are injected to the decay ring. The water-Cherenkov detector concept (MEMPHYS) have been studied as a far detector at Frejus (130 km) for CERN-based beta beam showing sensitivity for (additional) measurement of θ_{13} and the 3σ observation of the CP-violation with 78% of the true CP-violation phase values [57].

Currently the measured large value of the mixing angle θ_{13} have postponed the realisation of the β-beam as the experiment utilising the conventional high energy neutrino beam will be sensitive to determine the neutrino mass hierarchy and study the CP-violation phase.

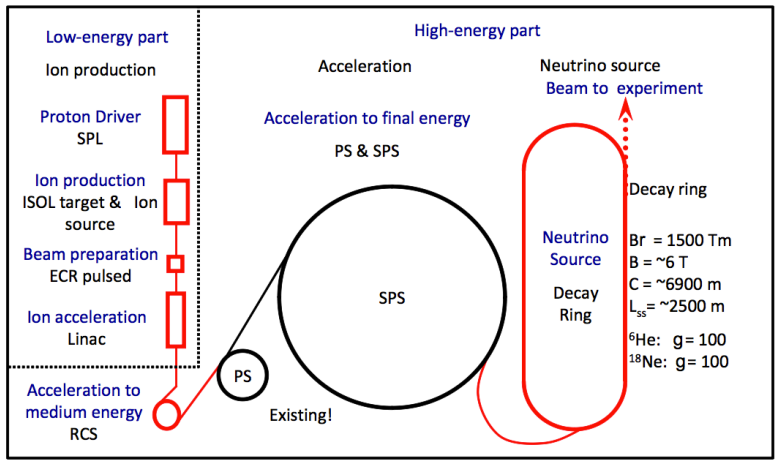

Figure 3.10.: Overview of the CERN-baseline Beta-Beam [56].

Neutrino Factory

In a concept of neutrino factory, the focus is in muons (instead of pions like in conventional beams). The bunching, accelerating and storing muons which then decay via

$$\mu^+ \rightarrow \bar{\nu}_\mu + e^+ + \nu_e \tag{3.14}$$

or

$$\mu^- \rightarrow \nu_\mu + e^- + \bar{\nu}_e \tag{3.15}$$

are key issues in the neutrino beam production in a neutrino factory [58]. An equal number of muon and electron neutrino flavors is produced. Compared with pions, muons have longer lifetime, which allows the artificial acceleration and collimation of them. Muons decay in a decay ring, just like the radioactive isotopes in the case of the β-beam. The neutrino factory allows to study the neutrino oscillations via various transitions. Following transitions are available for the beam of μ^+

$$\begin{aligned} \nu_e \rightarrow \nu_\mu \text{ (Golden channel)} \qquad & \bar{\nu}_\mu \rightarrow \bar{\nu}_\tau \text{ (Dominant channel)} \\ \nu_e \rightarrow \nu_\tau \text{ (Silver channel)} \qquad & \bar{\nu}_\mu \rightarrow \bar{\nu}_e \text{ (Platinum channel)} \\ \nu_e \rightarrow \nu_e \text{ (Disappearance channel)} \qquad & \bar{\nu}_\mu \rightarrow \bar{\nu}_\mu \text{ (Disappearance channel).} \end{aligned}$$

Similar channels are available for beam of μ^-. As the interactions of the both neutrinos and antineutrinos with same flavor are observed, the detector must have the lepton flavor discrimination and charge-identification capability. Magnetised iron calorimeter have been proposed for the detection technique.

The feasibility of the neutrino factory have been studied e.g in International Design Study for the Neutrino Factory (IDS-NF) [59]. In the baseline design pions are produced with 4 MW pulsed proton beam. The pions with opposite charge are separated with magnetic field and they decay to muons in transport channel. Muons are cooled down and bunched and rapidly accelerated to the desired energy (25 GeV) with an accelerator chain of linac ($\rightarrow$ 0.9 GeV), recirculating linear accelerators (0.9 $\rightarrow$ 12.6 GeV) and fixed field alternating gradient accelerator (12.6 $\rightarrow$ 25 GeV) before to be injected into the storage ring to produce neutrinos.

It has been shown that the neutrino factory with two far detectors with baselines of 4000 km and 7500 km are optimal for studying neutrino mixing parameters. Albeit the current measured value of the mixing angle θ_{13} makes the neutrino factory performance in a hunt for CP-violation comparable with the β-beam, the variety of different oscillation channels would outperform the other options to study the mixing parameters θ_{13}, δ_{CP}, θ_{23} and Δ_{31}.

More recently, the concept of low-energy neutrino factories (LENF) have been introduced [60]. Removing the last part of the muon acceleration system from the conventional neutrino factory (fixed field alternating gradient accelerator) results in a smaller and less expensive facility that produces lower energy neutrinos (1-4 GeV). A clear advantage of lower neutrino energies is the better performance of neutrino detectors in detecting such neutrinos than the neutrinos with higher energies.

4. Neutrino Oscillations

Neutrinos are produced in weak interactions processes where they appear as the so-called weak interaction states, i.e. in states with specific flavor: ν_e, ν_μ, ν_τ. Neutrinos propagating, on the other hand, do not necessarily have any specific flavor but they are superpositions of the flavor states. Hence, when a neutrino is detected it may have other flavor than it had when it was produced. This quantum mechanical phenomenon is called the neutrino oscillation. The theoretical basis the phenomenon of the neutrino oscillation was laid by B. Pontecorvo in 1957 [61]. Indications of neutrino oscillations was observed in solar neutrino experiments, which detected a deficit of the electron neutrinos, that is, less ν_e's were observed than were produced in the Sun (Homestake [31], Kamiokande, [32], GNO [33], SAGE [7]). The first direct experimental evidence of neutrino oscillations came from the measurement of atmospheric neutrinos in the Super-Kamiokande experiment [23]. In this experiment the flavor content of neutrinos produced in the atmosphere by cosmic rays depends on the direction of their entrance to the detector, i.e. on their distance of flight, in the way predicted by neutrino oscillation. In 2002, the solar neutrino problem was solved by the SNO experiment [62] which was able to measure in addition to the ν_e flux also the flux of muon and tau neutrinos and showing thereby that the total flux agrees with the prediction of the Solar Model. In this chapter the basic formalism and the open questions related to neutrino oscillations are presented and discussed.

4.1. Neutrino Mixing

The key ingredient of neutrino oscillation phenomena is that the flavour states (interaction states; ν_α, $\alpha = e, \mu, \tau$) are not the same as the mass states (propagating state; ν_k, $k = 1, 2, 3$) of the neutrino but their superpositions:

$$|\nu_\alpha\rangle = \sum_k U_{\alpha k} |\nu_k\rangle, \tag{4.1}$$

where $U_{\alpha k}$ are complex numbers.

In the standard three-neutrino mixing scenario the $U_{\alpha k}$'s are components of 3×3 unitary matrix U called the Pontecorvo-Maki-Nakagawa-Sakata (PMNS) matrix [63]:

$$\begin{pmatrix} |\nu_e\rangle \\ |\nu_\mu\rangle \\ |\nu_\tau\rangle \end{pmatrix} = \begin{pmatrix} U_{e1} & U_{e2} & U_{e3} \\ U_{\mu 1} & U_{\mu 2} & U_{\mu 3} \\ U_{\tau 1} & U_{\tau 2} & U_{\tau 3} \end{pmatrix} \begin{pmatrix} |\nu_1\rangle \\ |\nu_2\rangle \\ |\nu_3\rangle \end{pmatrix} \tag{4.2}$$

The PMNS matrix can be parametrised in terms of three rotation angles (mixing angles) θ_{ij}, characterising the mixing between mass and flavor states, and one phase δ in the following form

$$U = \begin{pmatrix} c_{12}c_{13} & s_{12}c_{13} & s_{13}e^{i\delta} \\ -s_{12}c_{23} - c_{12}s_{23}s_{13}e^{-i\delta} & c_{12}c_{23} - s_{12}s_{23}s_{13}e^{-i\delta} & s_{23}c_{13} \\ s_{12}s_{23} - c_{12}c_{23}s_{13}e^{-i\delta} & c_{12}s_{23} - s_{12}c_{23}s_{13}e^{-i\delta} & c_{23}c_{13} \end{pmatrix} \tag{4.3}$$

where $s_{ij} = \sin\theta_{ij}, c_{ij} = \cos\theta_{ij}$. For antineutrinos one has

$$|\bar{\nu}_\alpha\rangle = \sum_k U^\dagger_{\alpha k}|\bar{\nu}_k\rangle. \tag{4.4}$$

The CP conjugate of the transition $\nu_e \to \nu_\mu$ is $\bar{\nu}_e \to \bar{\nu}_\mu$. If U is not real, that is $\delta \neq 0, \pi$, the probabilities of these two transitions are different, meaning CP violation.

If neutrinos turn out to be Majorana particles, two additional phases, so-called Majorana CP-phases will be present in the mixing matrix. They can be introduced by multiplying the matrix U with the matrix

$$\begin{pmatrix} e^{-i\phi_1} & 0 & 0 \\ 0 & e^{-i\phi_2} & 0 \\ 0 & 0 & 1 \end{pmatrix}.$$

These phases, ϕ_1 and ϕ_2, will not play any role in neutrino oscillation experiments, as they do not affect the oscillation probability.

According to the Schrödinger equation, in vacuum the massive state $|\nu_k\rangle$ evolves in time as

$$\begin{aligned} i\frac{d}{dt}|\nu_k\rangle &= H|\nu_k\rangle = E_k|\nu_k\rangle \\ |\nu_k\rangle(t) &= e^{-iE_k t}|\nu_k\rangle. \end{aligned}$$

Here H is the Hamiltonian operator in vacuum and E_k is the energy of the mass eigenstate ν_k. Therefore, at time t the initial flavour state (Equation 4.1) has evolved to

$$|\nu_\alpha\rangle(t) = \sum_k U_{\alpha k} e^{-iE_k t}|\nu_k\rangle. \tag{4.5}$$

Assuming that the neutrinos have a finite but small mass, such that $m_k << p_k$ and $p_k \simeq E_k$, the neutrino energy E_k can be written as

$$E_k = \sqrt{p_k^2 + m_k^2} \simeq p_k + \frac{m_k^2}{2p_k} \simeq E + \frac{m_k}{E}. \tag{4.6}$$

The probability of neutrino with the initial flavor α to be observed with flavour β is given by

$$\begin{aligned} P_{\nu_\alpha \to \nu_\beta} &= |\langle \nu_\beta | \nu_\alpha(t) \rangle|^2 = |\sum_k U^\star_{\alpha k} U_{\beta k} e^{-\frac{m_k^2 t}{2E}}|^2 \\ &= \delta_{\alpha\beta} - 4 \sum_{k>j} \mathrm{Re}[U_{\alpha k} U^\star_{\beta k} U^\star_{\alpha j} U_{\beta j}] \sin^2(\frac{\Delta m^2_{kj} L}{4E}) \\ &\quad + 2 \sum_{k>j} \mathrm{Im}[U_{\alpha k} U^\star_{\beta k} U^\star_{\alpha j} U_{\beta j}] \sin^2(\frac{\Delta m^2_{kj} L}{2E}), \end{aligned} \tag{4.7}$$

where $\Delta m^2_{kj} = m^2_k - m^2_j$ is the neutrino mass square difference and $\Delta_{kj} = \frac{\Delta m^2_{kj} L}{2E}$ is the oscillation phase. If $\alpha = \beta$ the probability is called as the survival probability and if $\alpha \neq \beta$ as the disappearance probability of α or the appearance probability of β, depending on the context.

From the experimental point of view, the determination of mixing angles, mass-squared differences and CP violation phase is an interplay between the energy of neutrinos E and the distance from neutrino source to the detector L, called the baseline. This can be seen as a ratio L/E in Equation 4.7 If L/E is small, the terms with small Δm^2 cannot produce observable contribution to the total oscillation probability. On the other hand, a large L/E leads to rapid oscillations, which the detector cannot distinguish and the total contribution of the oscillating $\sin^2$ -part in Equation 4.7 averages to 1/2.

The PMNS-matrix (Equation 4.2) can be written as a product of three matrices associated with rotations in the three coordinate planes in form of

$$U = \begin{pmatrix} 1 & 0 & 0 \\ 0 & c_{23} & s_{23} \\ 0 & -s_{23} & c_{23} \end{pmatrix} \begin{pmatrix} c_{13} & 0 & s_{13} e^{-i\delta} \\ 0 & 1 & 0 \\ -s_{13} e^{-i\delta} & 0 & c_{13} \end{pmatrix} \begin{pmatrix} c_{12} & s_{12} & 0 \\ -s_{12} & c_{12} & 0 \\ 0 & 0 & 1 \end{pmatrix}. \tag{4.8}$$

As the two mass squared differences Δm^2_{21} and Δm^2_{32} have turned out to differ by two orders of magnitude, the corresponding mixing angles can be probed independently with experiments using different neutrino flavors as a source and different baseline covering a part of L/E parameter space. The θ_{12} and Δm^2_{21} have been determined with the solar and θ_{23} and Δm^2_{32} with atmospheric neutrinos. That is why θ_{12} and

$$
\begin{aligned}
\Delta m^2_{21} &= (7.53 \pm 0.18) \times 10^{-5}\mathrm{eV}^2 \\
\Delta m^2_{32} &= (2.44 \pm 0.06) \times 10^{-3}\mathrm{eV}^2(\mathrm{NH}) \\
\Delta m^2_{32} &= (2.52 \pm 0.07) \times 10^{-3}\mathrm{eV}^2(\mathrm{IH}) \\
\sin^2 2\theta_{12} &= 0.846 \pm 0.021 \\
\sin^2 2\theta_{23} &= 0.999^{+0.001}_{-0.018}(\mathrm{NH}) \\
\sin^2 2\theta_{23} &= 1.000^{+0.000}_{-0.017}(\mathrm{IH}) \\
\sin^2 2\theta_{13} &= (9.3 \pm 0.8) \times 10^{-2}
\end{aligned}
$$

Table 4.1.: Measured values of the oscillation parameters [42].

θ_{23} are sometimes called solar and atmospheric mixing angles and mass squared differences Δm^2_{21} and Δm^2_{32} solar and atmospheric mass differences, respectively. The third mixing angle θ_{13} has been determined in three reactor experiments (Daya Bay [64], RENO [65] and Double Chooz [66]).

The values of the oscillation parameters of the active neutrinos (ν_e,ν_μ,ν_τ) have been measured in many experiments. The current situation is summarised in Table 4.1. In Table 4.1 the values of Δm^2_{32} and $\sin^2\theta_{23}$ depend on the neutrino mass hierarchy (MH), that is, on the sign of Δm^2_{31}. For the time being, it is not known whether Δm^2_{31} is positive or negative, since neutrino oscillation experiments have not been sensitive to answer this question. The two possible possible orderings are called normal hierarchy (NH), where $\Delta m^2_{31} > 0$, and the inverted hierarchy (IH), where $\Delta m^2_{31} < 0$. The two scenarios are illustrated in Figure 4.1. The ordering of the mass states ν_1 and ν_2 is fixed by defining that the ν_1 state is the one containing the largest fraction of electron neutrino and taking into account the measured value of Δm^2_{12} from solar neutrino experiments to be positive. That leads to the ordering of $m_1 < m_2$.

As already mentioned above, the travel through dense medium, e.g. the Earth, the Sun or supernovae, can significantly alter the oscillatory behaviour of neutrinos. The modifications are caused by the coherent forward scattering with the material which they are traversing and are different for different neutrino flavors. This phenomenon, called the MSW-effect, was discovered by S. Mikheyev and A. Smirnov [67] and L. Wolfenstein [68].

The matter impacts differently on electron neutrinos and other flavors of neutrinos. This is due to the different interactions: electron neutrino have both charged and neutral current interactions with electrons of the medium, while ν_μ or ν_τ can interact only via neutral current interactions. This gives arise to potential energy $V_e =$

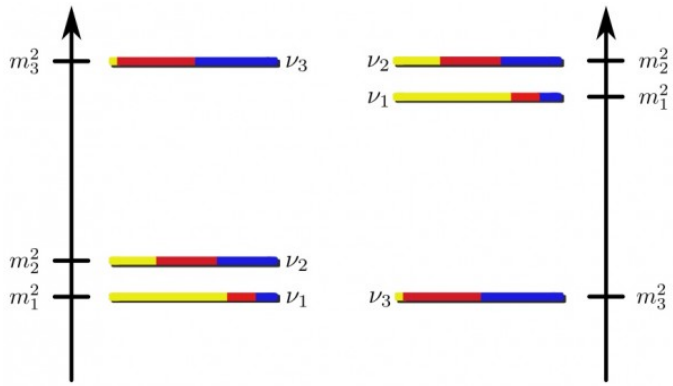

Figure 4.1.: Neutrino mass hierarchy (MH) schemes with three neutrino states. Left: Normal hierarchy, right: Inverted Hierarchy. Colour encoding of each state corresponds the fractions of the flavor content: yellow for electron, red for muon and blue for tau neutrino content.

$\pm\sqrt{2}G_F N_e$ for the electron neutrinos. The N_e is the electron number density of the medium and G_F is the Fermi constant. The positive sign is for the electron neutrino and the negative sign for the electron antineutrino.

In the case of two neutrino flavors, the effects of the medium neutrino traverse can be taken into account by replacing in the oscillation probability formula (Equation 4.7) the vacuum oscillation angle θ and the squared mass difference Δm^2 with the corresponding quantities in matter, defined as

$$\Delta m^2_{\text{mat}} = \sqrt{(A - \cos 2\theta)^2 + \sin^2 2\theta}\,\Delta m^2 \tag{4.9}$$

and

$$\sin^2 2\theta_{\text{mat}} = \frac{\sin^2 2\theta}{\sqrt{(A - \cos 2\theta)^2 + \sin^2 2\theta}} \tag{4.10}$$

with $A = 2\sqrt{2}G_F N_e E/\Delta m^2$. The transition probability for $\nu_e \to \nu_\mu$ is hence given by

$$P(\nu_e \to \nu_\mu) = \sin^2 2\theta_{\text{mat}} \sin^2\left(\frac{\Delta m^2_{\text{mat}} L}{4E}\right), \tag{4.11}$$

The equations above hold only for a constant matter density, but still this simplified two neutrino scenario helps to illustrate following consequences of matter effects:

- The electron number density of the medium should be large enough to develop significant matter effects.
- If $\cos 2\theta = A$, the resonance occurs and the oscillations is significantly enhanced.
- Because the V_e is different for neutrino and antineutrino, the A is different and matter affects differently neutrinos and antineutrinos.
- The A depends also on the sign of Δm^2. Hence the observing the neutrinos that have propagated through dense medium give information on the mass hierarchy.

The difference between matter and vacuum oscillation probabilities is illustrated in Figure 4.2, where the matter effects are calculated for neutrinos traversing the Earth.

4.2. Determination of Mass Hierarchy

The neutrino mass hierarchy affects the interpretation of the results of neutrino oscillation experiment and to the design of the neutrino experiment of the future. For example, the sensitivity of neutrinoless double beta decay ($0\nu\beta\beta$) experiments to measure the effective neutrino mass $|\langle m_{ee}\rangle|$ depends on the neutrino mass hierarchy. The oscillation probabilities of neutrinos traversing in dense matter depends also on the mass state ordering. Hence, the measuring the neutrino mass hierarchy is important for long baseline neutrino oscillation experiments and for experiments with atmospheric neutrinos, as well as, for understanding the dynamics of supernovae by means of neutrinos.

On the other hand, as the neutrino mass hierarchy affects many physics phenomena, the question of the neutrino mass hierarchy can be addressed in different experimental configurations measuring the effects of neutrino oscillations:

- the reactor $\bar{\nu}_e \to \bar{\nu}_e$ oscillation experiments with a medium baseline (tens of kilometers) (JUNO [2], RENO-50 [65]).
- the accelerator $\nu_\mu \to \nu_e$ or $\bar{\nu}_\mu \to \bar{\nu}_e$ with a long baseline (hundreds to thousands of kilometers) (NOνA [49], DUNE [3]).
- the atmospheric $\nu_\mu \to \nu_\mu$ or $\bar{\nu}_\mu \to \bar{\nu}_\mu$ oscillation experiments (PINGU [73], ORCA [74], INO [75], Hyper-K [76]).

All these approaches attempt to measure how the $sgn(\Delta m^2_{31})$ alters the oscillation probability function. From the experimental point of view, this requires:

- Sufficiently accurate knowledge of the baseline. In case of reactor experiment and long baseline experiment the baseline is fixed, but with atmospheric neutrinos

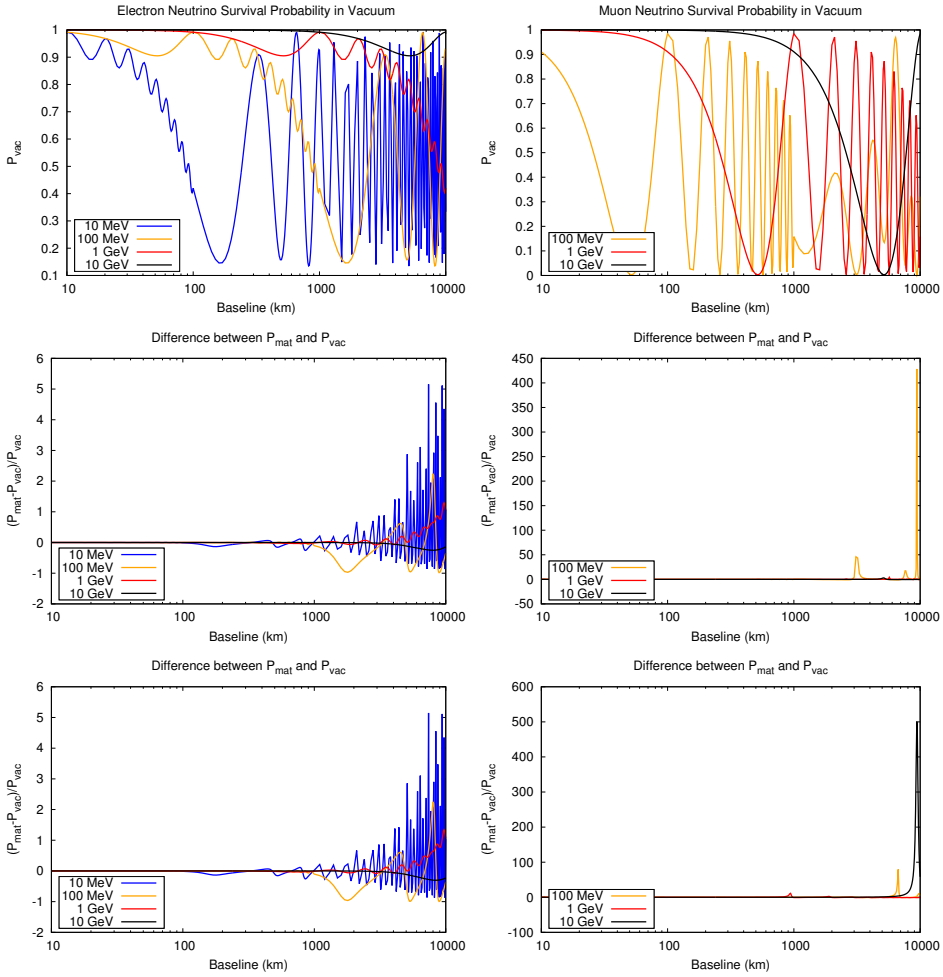

Figure 4.2.: Demonstration of the impact of the Earth matter effects on the survival probability of electron neutrino (left column) and muon neutrino (right column). Uppermost figures are the oscillation probabilities in vacuum. The middle figures show the difference between the probabilities including matter effects compared to vacuum case with varying density of the Earth (20 shells). Lowermost figures are calculated using average matter density of the earth. Note the different behaviour especially in case of muon neutrinos where the resonances occurs with different baseline lengths. Figures are done by using GLoBES oscillation code [69] [70] and in middle and bottom ones the PREM model [71] [72] is used to obtain the matter densities.

the reconstruction of the direction of the incident neutrino is required.

- Energy reconstruction capability is needed since the oscillation probability depends on energy of the neutrino. The outstanding energy resolution is needed especially with reactor experiment, due to the small variations in energy spectra of neutrinos are searched for.

- Very intensive neutrino source providing high enough statistics.

4.2.1. Reactor Neutrinos

The sensitivity to the neutrino mass hierarchy of so-called intermediate baseline reactor neutrino experiments arises from the interference effect of rapid oscillations induced by the squared mass differences Δm^2_{31} and Δm^2_{32} [77]. Figure 4.3 and Figure 4.4 illustrate the optimal location of an experiment (JUNO), reactor neutrino event spectrum with respect to the L/E ratio and the difference between normal hierarchy and inverted hierarchy scenarios with baseline (∼50km). The derivation relies on resolving the change of phase of small wiggles modulating the θ_{12} and Δm^2_{21} driven oscillation. The key issue is the Fourier transformation of the L/E spectrum. The Fourier power spectrum will have small shoulder next to the main peak, and the relative positions of these two features can be used to determine the mass hierarchy.

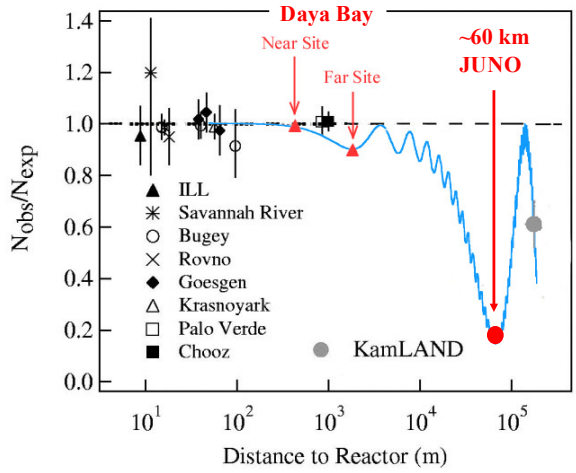

Figure 4.3.: The survival probability of reactor neutrinos. The JUNO is located at the distance from the reactors where the θ_{12}-driven oscillation is maximal.[1]

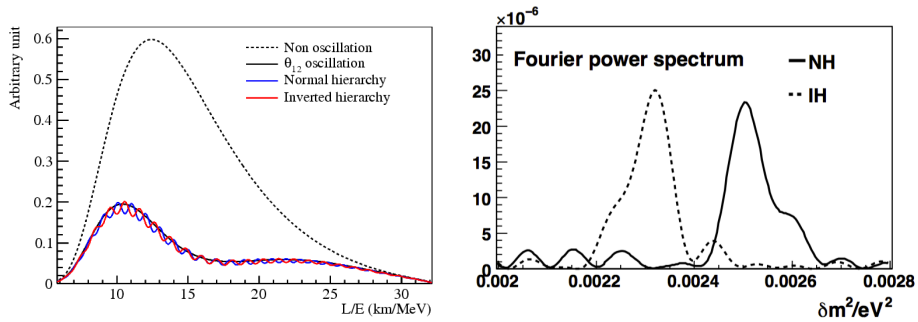

Figure 4.4.: The imprint of neutrino mass hierarchy in the spectrum of reactor neutrinos. Left: the L/E-spectrum of reactor neutrinos from reactor at the 60 km distance. The neutrino mass hierarchy can be resolved by looking the fast oscillations of red (NH) and blue (IH) curves. Right panel: the power spectrum of Fourier transform. The difference between normal hierarchy and inverted hierarchy is clearly visible. [2]

One advantage of the reactor neutrino approach is that the baseline is short enough to avoid neutrino matter effects. Hence the uncertainties coming from the density profile of the Earth and the matter induced CP-violating phase are not complicating the interpretation of the results.

From the experimental point of view observing such small spectral changes require high statistics (tens of thousands events) with sufficiently good energy resolution (3% at 1 MeV) [78] The location of the detector with respect to reactor cores is also crucial as small deviations from optimal distance substantially reduce the sensitivity of the measurement. Furthermore, if the distances to different reactor cores are different the imprint of fast oscillations is smeared [79]. The detector should also be build few hundreds of meters underground to shield it against cosmogenic muons.

The usual choice for the detection technique in the reactor neutrino experiments is a liquid scintillator detector. It is proven to work reliably in many experiments, most recently in three experiments of Daya Bay, RENO and Double Chooz [64] [65] [66]. when measuring the mixing angle θ_{13}. A further detector R&D to fulfil the requirements, especially to achieve the sufficient energy resolution but also from the construction point of view, is underway in a new experiment JUNO (Jiangmen Underground Neutrino Observatory) [2]. JUNO is under construction in Jiangmen in China. It will utilise large (∼20 kiloton) liquid scintillator detector located at 53 km from several nuclear reactor cores. Six reactor cores are under construction

[1] talk by Liangjian Wen in Neutrino 2014

in Yangjiang and two in Taishan. At the expected time of starting data taking with JUNO in 2020, all the cores should be operational. The JUNO collaboration has demonstrated that with reasonable assumptions the median sensitivity better than $\sim 3\sigma$ for determination of mass hierarchy can be achieved within 6 years of measurement [2].

Another proposed new experiment is RENO-50 [65] which will be constructed in South Korea. The scientific goals and design parameters of RENO-50 detector are quite similar to those of JUNO.

The JUNO and RENO-50 detectors are not intended to measure only the mass hierarchy, but they have rich physics programs of precision measurement of other neutrino oscillation parameters, and by observing solar, atmospheric, supernova, and geoneutrinos to gather information on the dynamics of these objects.

4.2.2. Atmospheric Neutrinos

Using atmospheric neutrinos to probe the neutrino mass hierarchy relies on the matter enhanced oscillation effects when neutrinos traverse through the Earth. These resonance oscillations can only occur for neutrinos in the case of normal hierarchy or for antineutrinos in case of inverted hierarchy. The oscillation probabilities of different neutrino oscillation channels with respect to the neutrino energy are illustrated in Figure 4.5. Different baselines through the Earth (cosine of zenith angle) are shown. The difference between normal and inverted hierarchy is visible in the plots.

To search for the neutrino mass hierarchy with atmospheric neutrinos requires a detector which can resolve the direction of the incoming neutrino and reconstruct its energy within the range of 2-10 GeV. The proper energy determination usually requires that the event is contained in the detector volume. This requires large volume detectors. The charge identification of the final state muon increases the sensitivity of the mass hierarchy determination. The main aim of such experiments is to reproduce the earth neutrino oscillogram shown in Figure 4.6 where the oscillation probability is plotted for different values of the neutrino energies E_ν and $\cos\theta_z$, where θ_z is the zenith angle of the incoming neutrino.

There are several detector concepts introduced for resolving the neutrino MH using atmospheric neutrinos. The PINGU (Precision IceCube Next Generation Upgrade) [73] is the extension of the IceCube and DeepCore detectors at the South Pole. The ORCA (Oscillation Research with Cosmics in the Abyss) [74] is a similar kind of detector setup to be deployed into the Mediterranean Sea. Both of these detectors are insensitive to the electric charge of particle which limits the sensitivity of mass hierarchy measurement. Both collaborations have announced to achieve the 3σ significance within 3-5 years' measurement.

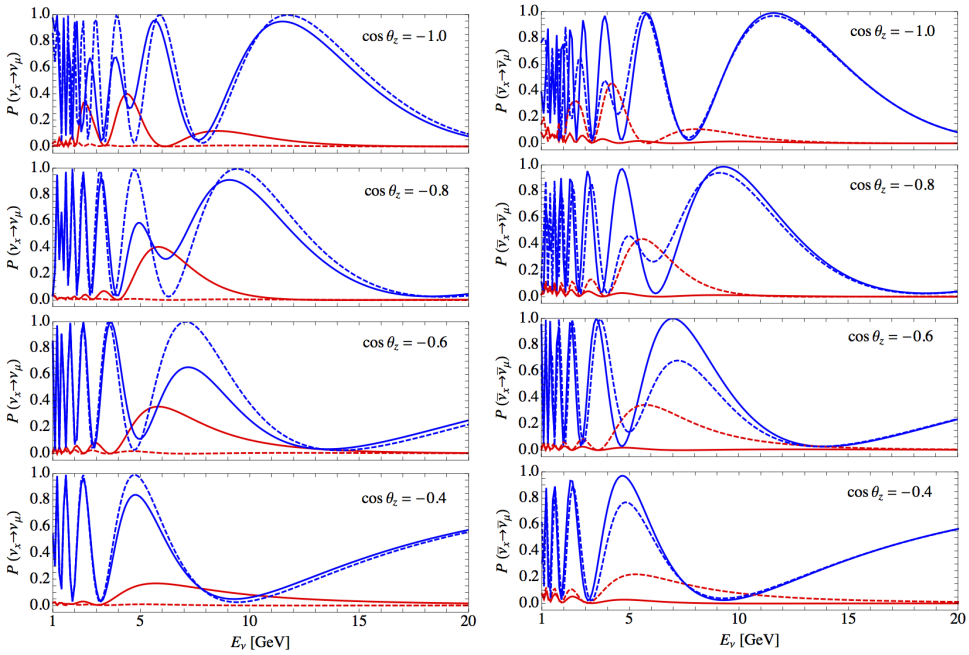

Figure 4.5.: Oscillation probabilities for $\nu_\mu \to \nu_\mu$ (blue lines) and $\nu_e \to \nu_\mu$ (red lines) transitions with respect to the neutrino energy E_ν. From top down the zenith angle θ_z decreases as indicated. The left panel shows the behaviour of neutrinos and the right panel of antineutrinos. The solid lines correspond to the normal hierarchy and the dashed lines to inverted hierarchy. [80]

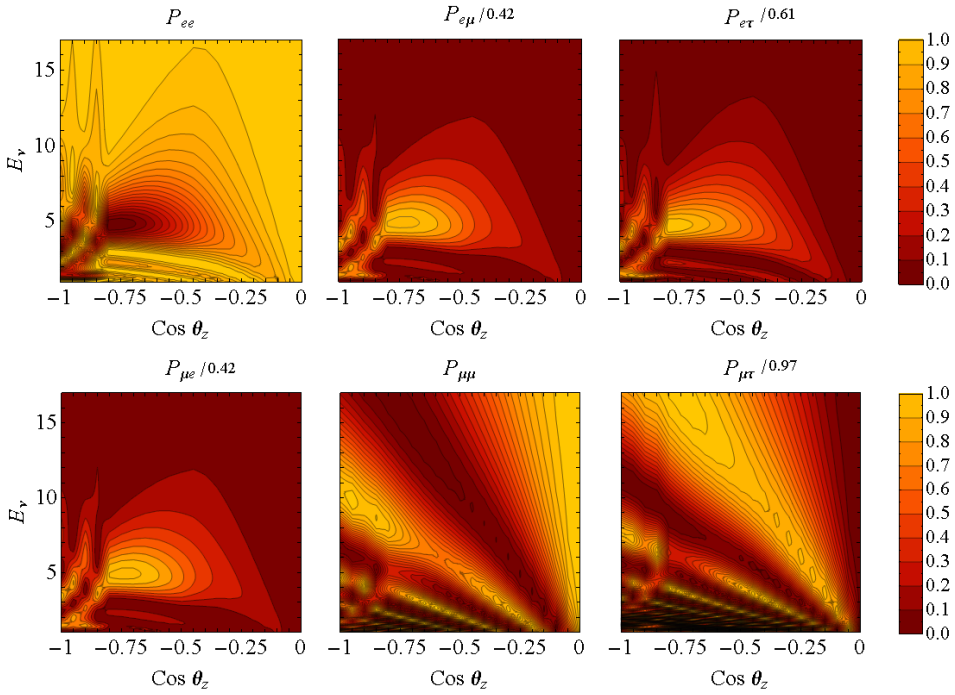

Figure 4.6.: Neutrino oscillograms of the Earth (lines of equal probabilities in the $E_\nu - \cos\theta_z$ -plane) for different oscillation channels. Oscillation probabilities are normalized according to their maximum value in the parameter space of each panel. The normal hierarchy is assumed. [80]

INO (India-based Neutrino Observatory) [75] detector is a concept of 50 kiloton magnetised iron calorimeter. The advantage of this approach compared with PINGU and ORCA would be the charge identification. Although the mass of the detector is relatively large, the size (fiducial volume) still restrict the number of collected events feasible for MH analysis. The sensitivity of the INO detector is estimated to be $\sim 3\sigma$ with 10 years of measurement.

The next-generation water-Cherenkov detectors, like Hyper-Kamiokande [76] will also be capable to determine the MH. In this detection technology the charge information is limited, but the discrimination between electrons and muon neutrinos (especially in the sub-GeV region) will compensate that. The sensitivity of determining the mass hierarchy is estimated to be better than 3σ if $\sin^2\theta_{23} > 0.4$ with 10 years' effective measurement.

The liquid argon detectors proposed for the next-generation neutrino beam experiments (LBNE (Long-Baseline Neutrino Experiment) [81] , LBNO (Long-Baseline Neutrino Oscillations) [54] and the joint effort of these collaborations DUNE (The Deep Underground Neutrino Experiment) [3]) have as one of their main goals to determine the neutrino mass hierarchy. Their excellent particle identification and energy and angular resolution compared with the other detector types mentioned above make them most efficient detectors, not only for beam neutrinos, but also for atmospheric neutrinos. With atmospheric neutrinos only, the single-phase liquid argon detector planned in the LBNE project would reach better than 3σ significance for the mass hierarchy with 350 kt·year exposure [81].

4.2.3. Long Baseline Neutrino Beam

In long-baseline neutrino beam experiments the probability of muon neutrino oscillation to electron neutrino (electron neutrino appearance probability) is different for different mass ordering of neutrino mass states. This is illustrated in Figure 4.7 for the very long baseline (2300 km) from CERN to Pyhäsalmi mine studied in LBNO project [54].

The separation between the NH and IH alternatives, requires sufficient long flight in matter to develop. Baselines shorter than 500 km are not capable for a high significance measurement. Crucial issues are the size of the detector to get enough statistics (order of tens of kilotons), the sufficient energy resolution in GeV region, clear separation between muon and electron induced events and the background rejection capability.

The current long-baseline experiments T2K, MINOS+ or NOνA do not have the potential to exceed the 3σ threshold in determining the MH, but the proposed long baseline experiments, like LBNO and LBNE/DUNE will exceed this accuracy. As

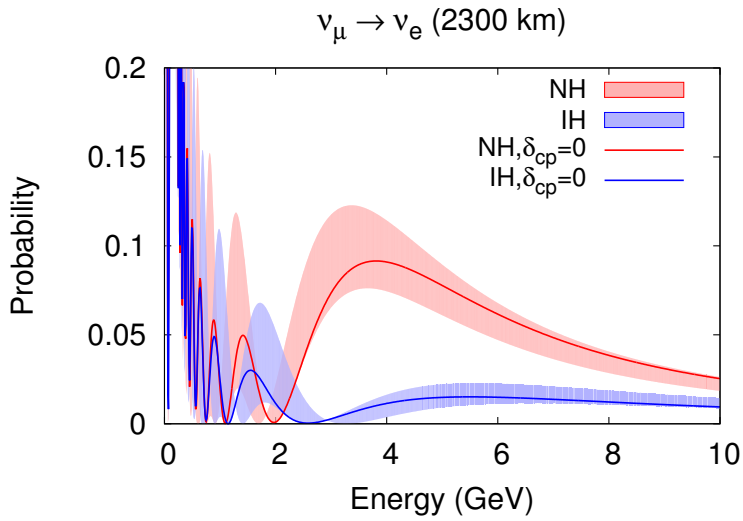

Figure 4.7.: The conversion probability of muon neutrinos to electron neutrinos with 2300 km baseline. The difference between normal hierarchy (NH, in red) and inverted hierarchy (IH, in blue) is clearly visible. The shaded areas correspond to the effect of CP-violation, the CP angle δ being allowed to vary in the range 0 to 2π. Other oscillation parameters are fixed to the best fit value according to Table 4.1.

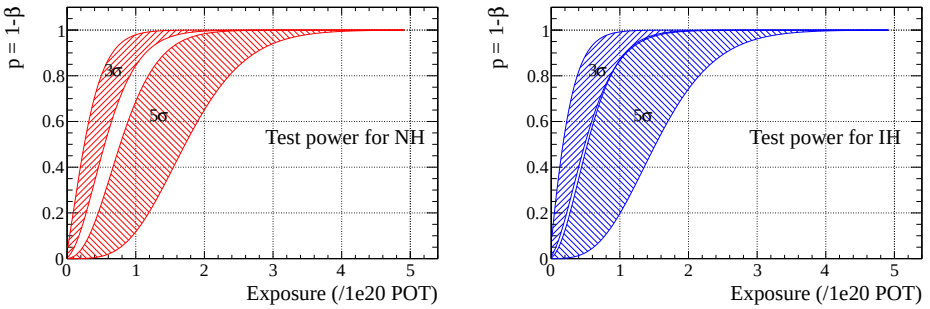

Figure 4.8.: The statistical power to resolve the neutrino mass hierarchy in case of normal hierarchy (left) and inverted hierarchy (right) with the LBNO scenario: 20 kton LAr detector with SPS (700kW) beam and baseline of 2300 km. The shaded areas denote the probability to obtain 3σ and 5σ significance. The variation originates in the statistics and the uncertainties related to neutrino oscillation parameters, especially the value of δ_{CP}. In both cases, the statistical power to make 5σ measurement after 5×10^{20} protons on target (POT) (≈ 5 years) is $\sim$1. [54]

an example, the estimated sensitivity reach of the LBNO experiment [54] is given in Figure 4.8. It is shown that the rejection of the wrong hierarchy can be done with 5σ significance with exposure $\sim 5 \times 10^{20}$ protons on target (POT) with a 20 kton LAr detector. This would correspond to 5 years of CERN-SPS running. In this particular case the long baseline of 2300 km helps with the mass hierarchy determination and 5σ significance can be reached independently of octant of θ_{23} or the value of the CP violating phase δ_{CP}. Regrettably, there are no plans for a neutrino beam from CERN in the near future.

4.2.4. Other Indications of Mass Ordering

The mass hierarchy can also be probed using the burst of neutrinos created in possible core-collapse supernovae. There are different approaches available for this: one can look for the earth-matter effects in the energy spectrum of neutrinos [82], observe the so-called spectral swapping of ν_e and $\nu_{\mu,\tau}$ below some critical energy [83], or study the rise time of the $\bar{\nu}_e$ signal [84]. However, the models of supernova collapse and therefore the flavor conversion mechanism in supernovae are still uncertain which limits the feasibility of these methods.

Another probe of the MH is given by the neutrino mass measurements. For example, the effective neutrino mass (m_{ee}) measured in neutrinoless double beta decay is

Experiment	Isotope	Detection Technique	Mass (goal)
MAJORANA [86]	^{76}Ge	Point contact Ge	40 kg (1 t)
GERDA [87]	^{76}Ge	Semicoax/BE	36 kg
CDEX [88] / NG-Ge76	^{76}Ge	Point contact Ge	10 kg (1 t)
COBRA [89]	^{166}Cd	CdZnTe	(45 kg)
CANDLES [90]	^{48}Ca	CaF_2 scintillator	300 kg
AMoRE [91]	^{100}Mo	Low-T MMC	1.5 kg (200 kg)
MOON [92]	^{100}Mo	Foils + scintillator	(0.48 t)
EXO200 [93]/nEXO	^{136}Xe	LXe TPC	110 kg (4.7 t)
NEXT [94]	^{136}Xe	High-P TPC	10 kg (100 kg)
PandaX [95]	^{136}Xe	High-P TPC	20 kg (200 kg/ 1t)
KamLAND-Zen [96]	^{136}Xe	Liquid scintillator	383 kg (1 t)
SuperNEMO [97]	^{82}Se	Foils + tracker	(20 $\times$ 7 kg)
CUORE [98]/CUPID [99]	^{130}Te	Bolometers	39 kg (206 kg/1 t)
SNO+ [100]	^{130}Te	Liquid scintillator	(260 kg)

Table 4.2.: Overview of the current double beta decay experiments and R&D projects

sensitive to the mass hierarchy provided the lightest neutrino mass state is sufficiently light $m \lesssim 10^{-2}$ eV. This is illustrated in the upper left panel of Figure 4.9. For the IH ($\Delta m^2_{23} < 0$) $|m_{ee}| \geq 10^{-2}$ eV, while for NH ($\Delta m^2_{23} > 0$) $|m_{ee}|$ can be much smaller.

Currently there are very active R&D programs aiming the large scale double beta decay experiments utilising different isotopes and different detection techniques. Most of the operational prototypes of these experiments are at the level of one to some tens of kilograms and that is not enough to reach the mass range where the neutrino mass hierarchy can be determined. The most stringent limit for Majorana neutrino mass ($|m_{ee}|$) of 60 - 161 meV (90% C.L.) is set by the KamLAND-Zen experiment [85]. To cover the region of inverted mass hierarchy, the mass of the double beta decaying source should be of the order of one ton and that is the goal of the various on-going projects summarised in Table 4.2.

Similar kinds of splittings as in the case of double beta decay are available for direct measurement of electron neutrino mass (m_{ν_e}) and the sum of neutrino states $m_{\text{cosmo}} = \sum_i \nu_i$ coming from cosmological measurements, also illustrated in Figure 4.9 [101]. Direct mass measurements relies on the measurement of the end point energy of beta-decay electron spectrum or the electron capture process. The KATRIN experiment [102] utilising the tritium source is expected to start the data taking in 2017 and the design sensitivity reach of 200 meV would not reach the inverted hierarchy region. Other approach based on the measurement of cyclotron frequency of the emitted electron from tritium decay [103] called ProjectX is in R&D phase

and aims to probe the inverted mass hierarchy region. An experiment to measure the electron neutrino mass from the electron capture of ^{163}Ho (HOLMES [104]) is in demonstrator phase to prove the feasibility of the technique.

4.3. Observation of CP-violation with Neutrinos

In addition to the mass hierarchy, another undetermined parameter in the mixing matrix (in Equation 4.3) is the CP-violating phase δ_{CP}. The matrix elements containing the δ_{CP} dependence also contain $\sin\theta_{13}$. The unknown value of the mixing angle θ_{13} have been the bottleneck towards fixing the best experimental scheme to search for CP violation with neutrinos. However, recently reactor neutrino experiments have shown that zero θ_{13} -scenario can be excluded and that the value of $\sin^2 2\theta_{13}$ is relatively large $\sin\theta_{13} = (9.3 \pm 0.8) \times 10^{-2}$ [42]. This has opened the possibility to look for the effects of CP violation in neutrino oscillation experiments.

4.3.1. Long Baseline Neutrino Beam Experiment

The most promising way to observe the CP violation phase of the PMNS-matrix is to employ high-power, high-energy neutrino beams. The oscillation channel is the same as used for probing the neutrino mass hierarchy, that is $\nu_\mu \rightarrow \nu_e$, but in this case the length of the baseline is not as crucial as it is for the determination of the mass hierarchy.

Controlling the systematic uncertainties and the event statistics are the key issues in hunting the CP violation. The effect of non-zero or non-π phase is illustrated in Figure 4.7 for CERN-Pyhäsalmi baseline studied in the LBNO [54]. The shaded areas denote the spread caused by the values of δ_{CP}. The determination of the CP violation phase relies on the measurement of the behaviour of the probability function inside the shaded area and that requires high statistics. The sensitivity of LBNO in excluding $\delta = 0, \pi$ with different beam scenarios is shown in Figure 4.10.

A great part of this work is done in connection to the LAGUNA-LBNO Design Study, which was completed in 2015 and where the detection of the leptonic CP violation was one of the main issues. Later on the expertise and knowhow achieved in this study has been taken in use in the DUNE project, which aims to a realisation of a long-baseline neutrino oscillation experiment with Fermilab-Homestake baseline. The detector technology in DUNE proposal is decided to be liquid argon TPC.

The CP violation can also be probed in the proposed Hyper-Kamiokande water-Cherenkov detector with upgraded T2K neutrino beam from J-Parc. The baseline of 295 km accompanied with Mton-class detector would provide high statistics. However,

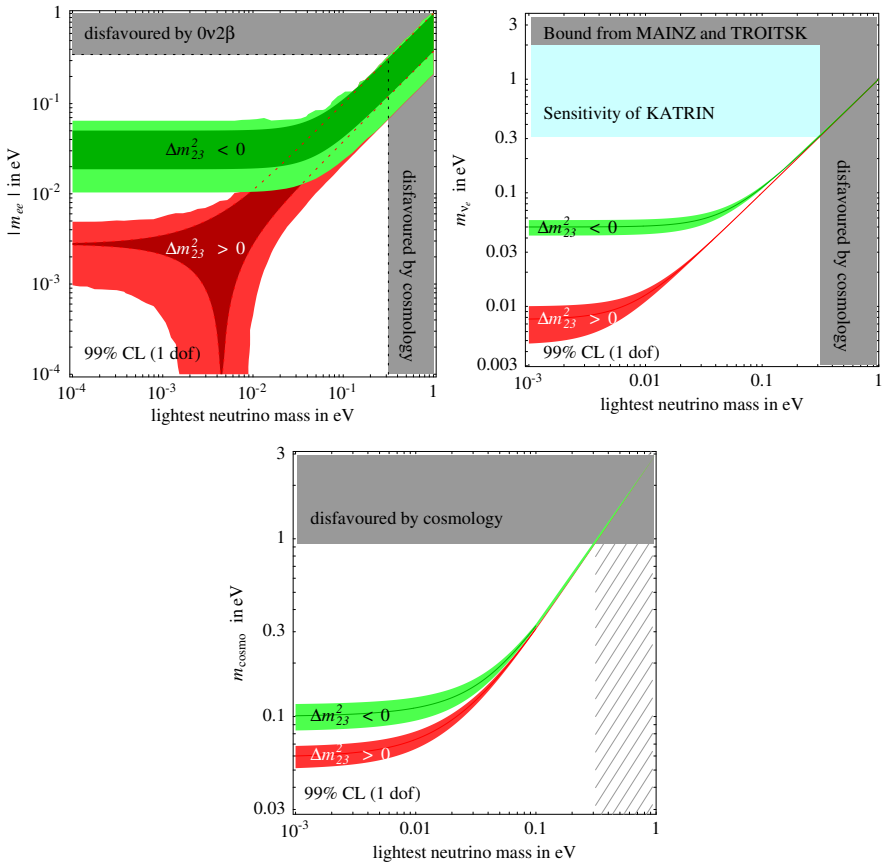

Figure 4.9.: Bounds on the effective neutrino mass ($|m_{ee}|$), electron neutrino mass (m_{ν_e}) and mass of the sum of neutrino states (m_{cosmo}) obtained on the basis of different measurements with respect to the lightest neutrino mass [101]. The normal hierarchy is shown in red and the inverted hierarchy is shown in green. Darker regions depict the scenario with negligible uncertainties of oscillation parameters. In every case, the Normal Hierarchy is the only allowed if the effective mass is sufficiently light.

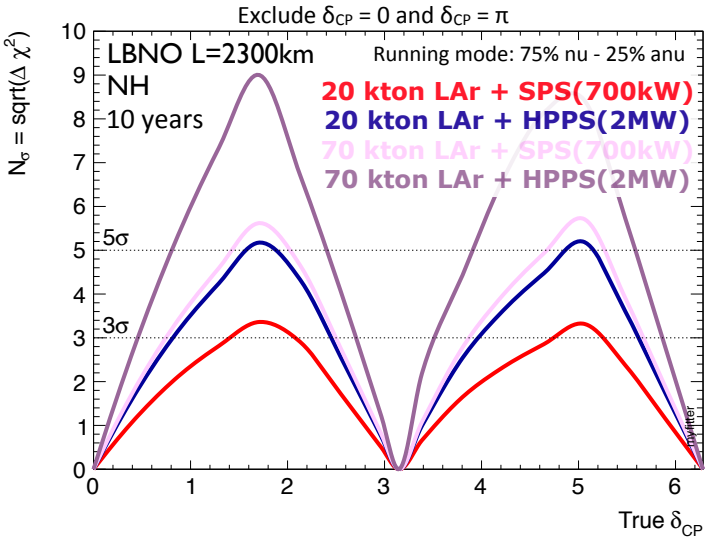

Figure 4.10.: Sensitivity for excluding the $\delta_{CP} = 0$ or $\delta_{CP} = \pi$ as a function of δ_{CP} in LBNO experiment [54].

due to the relatively short baseline ($\sim$ 295 km), the experiment is not sensitive to the neutrino mass hierarchy.

4.3.2. Short-baseline Experiment with Low-Energy Neutrinos

Apart from the long-baseline experiments discussed above the leptonic CP violation can also be tested using low-energy (<60 MeV) neutrinos coming from several pion decay-at-rest beams i.e. neutrinos from stopped muons with short baselines (1.5 km, 8 km and 20 km). Intensive neutrino beams can be produced with high power cyclotrons. The neutrinos are detected in a gigantic water or scintillator-based detector. The Daeδalus collaboration have estimated the sensitivity reaches for different scenarios with cyclotron approach alone and for cyclotrons combined with other neutrino beams [105] (see Figure 4.11). The Daeδalus approach in the context of LENA is discussed in Chapter 11 of this thesis.

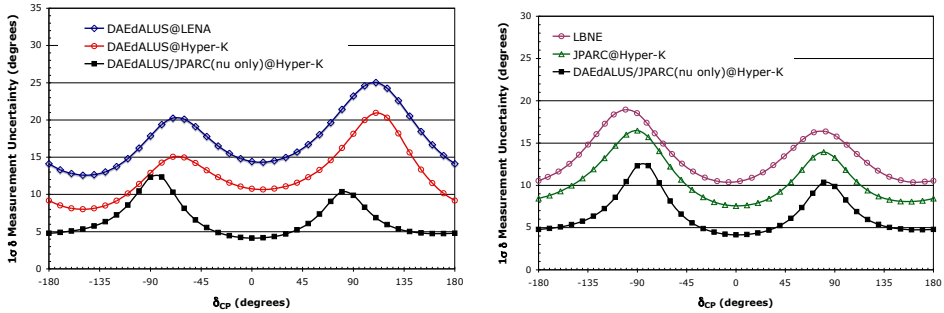

Figure 4.11.: The estimated 1σ uncertainties of the Daeδlus approach for the measurement of CP violation phase alone with the proposed LENA and Hyper-Kamiokande detectors and impact of combining the result with the long baseline beam from J-Parc to Hyper-Kamiokande. [105]

4.4. Search for Sterile Neutrinos

The number of the active neutrinos, that is, neutrinos with ordinary Standard Model interactions, is limited by the LEP experiment to three [106]. However, there are some experimental results that can not be explained in terms of mixing of the three active neutrinos, but which seems to indicate the existence of sterile flavor of neutrinos, i.e. neutrinos which do not have Standard Model gauge interactions. The strongest argument for the existence of sterile neutrinos is inferred from the results of the LSND (Liquid Scintillator Neutrino Detector) experiment, where $\bar{\nu}_\mu \rightarrow \bar{\nu}_e$ transitions were observed in a decay-at-rest $\bar{\nu}_\mu$ beam at Los Alamos National Laboratory [9]. The most straightforward interpretation of the LSND result is antineutrino oscillation with a squared mass difference of about 1 eV^2. This value is three (five) orders of magnitude larger than measured atmospheric (solar) mass-squared difference. The measured beam neutrino excess and interpretation is shown in Figure 4.12.

The one of the goals of the more recent MiniBooNE (Mini-Booster Neutrino Experiment) was to confirm or reject the LSND results. Instead of decay-at-rest beam, the neutrinos from conventional decay-in-flight neutrino beam, produced by 8 GeV protons from the Booster at Fermilab were used. The MiniBooNE detector, located 541 m from the target, an excess of electron antineutrinos of 78.4 ± 28.5 (2.8σ C.L) and excess of electron neutrinos of 162 ± 47.8 (3.4σ C.L.) were observed. [10] (see Figure 4.13). The observed excess of antineutrino events is consistent with the LSND results. For electron neutrinos, an excess of events at low energies (E_ν <475 MeV) was observed but not at higher energies. This causes some tension between the LSND

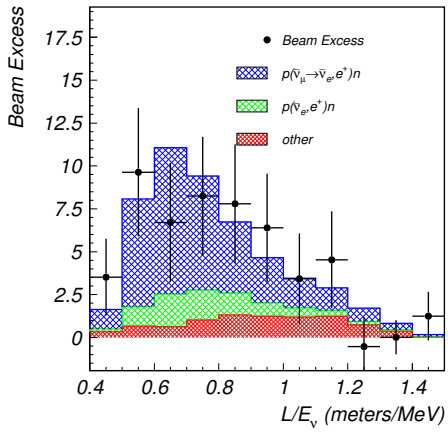

Figure 4.12.: Excess of observed beam neutrino events in LSND experiment [9]. The L_ν/E_ν distribution with $20 < E_e < 60$ MeV, where L_ν is the distance travelled by the neutrino in meters and E_ν is the neutrino energy in MeV. The data contradict the standard three-flavor neutrino oscillation scenario, but agree well with the expectation from neutrino background and additional neutrino oscillation with $\Delta m^2 \approx 1$ eV^2.

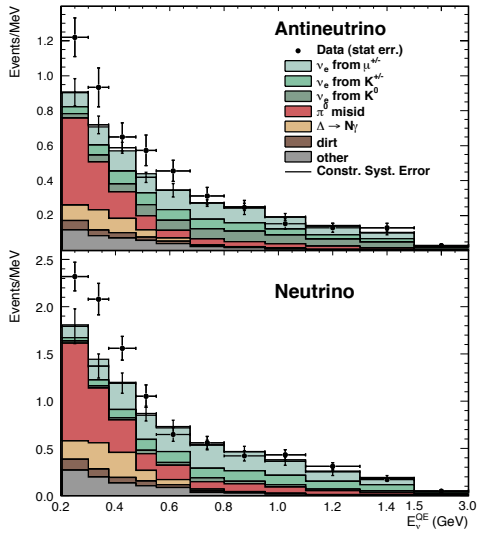

Figure 4.13.: The observed and expected events in MiniBooNE experiment: the antineutrino mode (top) and neutrino mode (bottom). [10]

and MiniBooNE results.

In addition to the $\bar{\nu}_\mu \rightarrow \bar{\nu}_e$ -conversion results discussed above, another hint contradicting the three-neutrino scenario comes from the $\nu_e \rightarrow \nu_e$ survival experiments observed in the calibrations of the radio-chemical solar neutrino experiments GALLEX [107] and SAGE [108]. In these calibrations, intensive artificial low-energy neutrino sources of ^{51}Cr and ^{37}Ar were used to check the performance of the detectors. The deficit of the measured event rates in comparison with the expected ones was observed in both GALLEX and SAGE with Chromium source 0.81 ± 0.10 and 0.95 ± 0.12, respectively, and in SAGE with argon source $0.79^{+0.09}_{-0.10}$. [109] (see Figure 4.14) . This deficit is known as the Gallium Anomaly.

More recently similar deficit has been observed in the fluxes of reactor neutrinos when using the up-to-date nuclear fission data. This is known as the Reactor Neutrino Anomaly. The re-evaluation called for a 3% increase of the reactor neutrino flux. The cross section of the inverse beta decay was also updated. As a consequence, the data from past short baseline reactor neutrino experiments, originally thought to be consistent with non-oscillation hypothesis, was now showing an about 6% deficit of antineutrino events. The new analysis indicated, at the 98.6% confidence

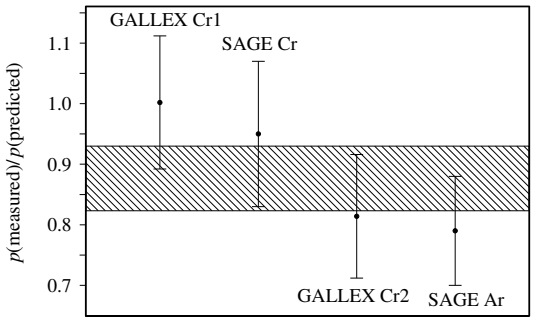

Figure 4.14.: The ratio of measured and predicted $\nu_e \rightarrow \nu_e$ survival probability for calibrations of the GALLEX and the SAGE experiments indicating the deficit of electron neutrinos [109]. The hashed region is the weighted average of all four experiments. [109]

level, a deviation from the non-oscillation scenario. The re-evaluated results of different reactor experiments are shown in Figure 4.15. [110]. The reactor anomaly is still disputable, since the uncertainties of the nuclear data and/or the incomplete understanding of neutrino production in nuclear reactors makes the interpretation of the data uncertain.

It is also worth mentioning that not all the experiments have observed the anomalies described above. For example, at the same time with LSND experiment, observing same transition $\bar{\nu}_\mu \rightarrow \bar{\nu}_e$, in the KARMEN experiment the excess of events was not observed [111]. The non-observation of muon neutrino disappearance in the MINOS neutrino beam experiment contradicts, too, the sterile neutrino scenario. The T2K collaboration has performed an unsuccessful search for ν_e disappearance due to sterile neutrinos with the off-axis near detector with baseline of 280 m. The analysis of ν_e charged-current (CC) interactions excludes region at 95% CL is approximately $\sin^2 2\theta_{ee} > 0.3$ for $\Delta m^2_{eff} > 7$ eV^2. [112].

In the simplest sterile neutrino scenario, just one sterile state is introduced, assumed to mix with the standard active neutrinos. The neutrino mixing matrix (Equation 4.3) is then extended to a 4×4 matrix with three additional mixing angles θ_{14}, θ_{24} and θ_{34} and three additional squared mass differences Δm^2_{41}, Δm^2_{42} and Δm^2_{43}.

The global fits to the experimental data contradicting the three-neutrino scenario

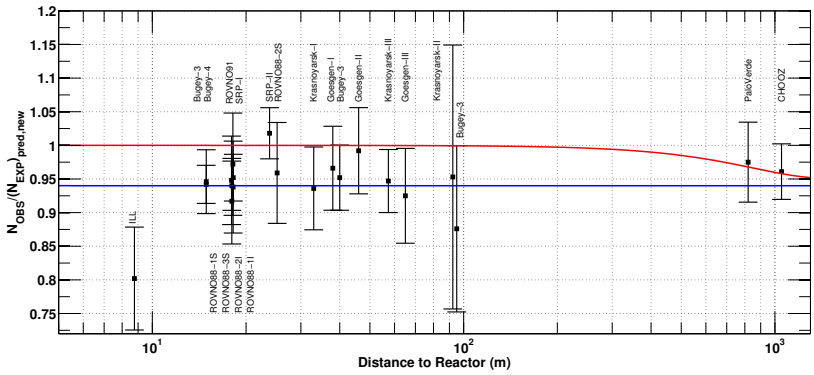

Figure 4.15.: Reevaluated short baseline reactor neutrino measurements leading to the 98.6% confidence level indication of deficit electron antineutrinos. [110]

indicate that the $|\Delta m^2_{41}|$ is much larger than the known mass squared differences Δm^2_{21} and Δm^2_{32}. Naturally, the addition of a new neutrino flavor makes the mass hierarchy schemes more complex. If the normal hierarchy is assumed, the sterile neutrino state (ν_4) would be much heavier than other massive states, implying that $\Delta^2_{41} >> |\Delta^2_{31}| >> \Delta^2_{21} > 0$. Because the sterile flavors cannot be observed directly, their imprint should be searched from the oscillation probabilities of active neutrinos. Following the parameterisation presented in [113], for short baselines the oscillation probabilities can be approximated in the follows:

$$
\begin{aligned}
P_{\nu_e\to\nu_e} &= 1 - \sin^2(2\theta_{14})\sin^2\Delta_{41} \\
P_{\nu_e\to\nu_\mu} &= P_{\nu_\mu\to\nu_e} = 4c^2_{14}s^2_{14}s^2_{24}\sin^2\Delta_{41} \\
P_{\nu_e\to\nu_\tau} &= 4c^2_{14}c^2_{24}s^2_{14}s^2_{34}\sin^2\Delta_{41} \\
P_{\nu_e\to\nu_s} &= 4c^2_{14}c^2_{24}c^2_{34}s^2_{14}\sin^2\Delta_{41} \\
P_{\nu_\mu\to\nu_\mu} &= 1 - c^2_{14}s^2_{24}(3 + 2c^2_{14}\cos^2(2\theta_{24}) - \cos^2(2\theta_{14}))\sin^2\Delta_{41} \\
P_{\nu_\mu\to\nu_\tau} &= 4c^4_{14}c^2_{24}s^2_{24}s^2_{34}\sin^2\Delta_{41} \\
P_{\nu_\mu\to\nu_s} &= 4c^4_{14}c^2_{24}c^2_{34}s^2_{24}\sin^2\Delta_{41}.
\end{aligned}
\tag{4.12}
$$

Here the contributions related to the squared mass differences in Δ_{32} and Δ_{21} are neglected. Within the scope of this work, the most important is the first equation.

The current four-flavor fits based on the data favouring the existence of sterile neutrino are collected in Figure 4.16 and Table 4.3 [114]. Separate fits for each experiment type are presented: reactor experiments (Reactor), Gallex and SAGE experiments (Gallium) and ν_e+^{12}C (C12) data from LSND and KARMEN. Results from the

	Reactor	Gallium	C12	Combined	Global-low	Global-high
Δm^2_{41}	1.95	2.24	13.80	7.59	0.9	1.6
$\|U_{e4}\|^2$	0.026	0.15	0.13	0.036	0.027	0.036
$\|U_{\mu 4}\|^2$					0.021	0.0084
$\sin^2 2\theta_{e\mu}$					0.0023	0.0012
$\sin^2 2\theta_{ee}$	0.10	0.51	0.45	0.14	0.10	0.14
$\sin^2 2\theta_{\mu\mu}$					0.083	0.034

Table 4.3.: 3+1 sterile neutrino fits to the experimental data [114].

combined fit of three previous ones (Combined) is also shown in both. In addition the two combined fits including more recent MiniBooNE results are included. The Global-low and Global-high fits proceed with and without the low-energy ($E_\nu < 475$ MeV) data, respectively.

4.4.1. Proposed experiments

The proposed experimental approaches to search for sterile neutrinos can be divided into three categories: to the accelerator-based search, where the disappearance or appearance of certain neutrino flavor could be observed, to reactor-based experiments with very short baseline of few meters and the spectral distortions in observed energy and spatial spectrum of reactor neutrino events is searched for, and to experiments using radioactive sources, so called oscillometric measurements, where the oscillation pattern is searched within the detector itself.

The Fermilab Short Baseline program [51] has been established to search for sterile neutrino flavors with muon neutrino beam and three detectors based on the liquid-argon technology: 112 ton near detector at 110m, 89 ton MicroBooNE detector at 470 m and 476 ton ICARUS T600 -module at 600 m from the beam target. Compared to the MiniBooNE experiment, the addition of a near detector and a larger far detector will improve the background rejection and increase the coverage in L/E parameter space. The estimated sensitivity is shown in Figure 4.17. The MicroBooNE collaboration has already announced the first observations of cosmic muon tracks, and the upgrade process of the ICARUS detector is under way at CERN (the WA104 experiment).

There are also other proposals to search for sterile neutrinos using accelerator-based approach:

- Stored muon beam proposed in nuSTORM [115], which is considered as a step towards a neutrino factory, can also be used for searching of sterile neutrinos.

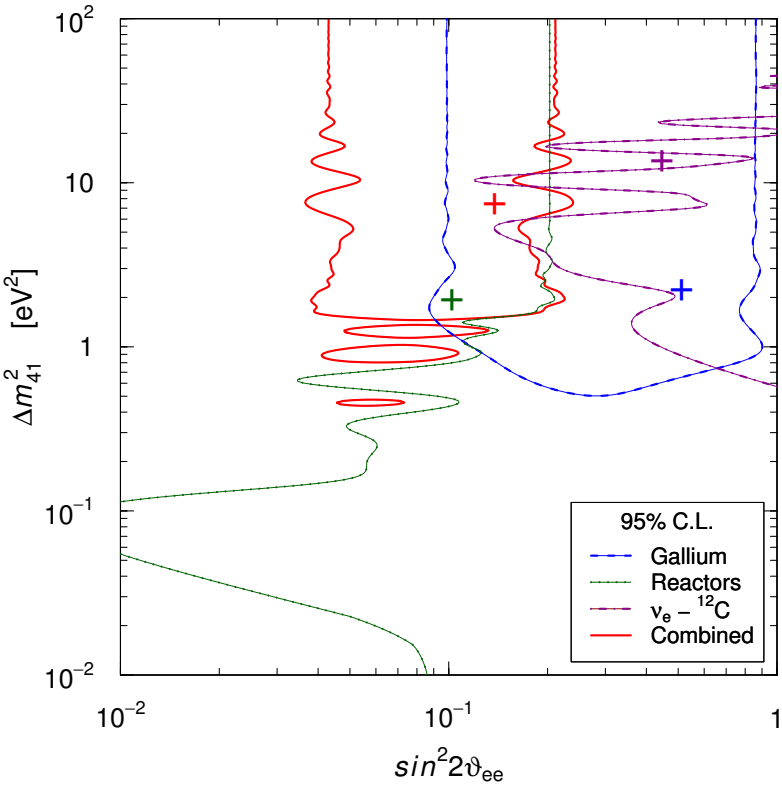

Figure 4.16.: Allowed regions (95% C.L.) and best fit values (crosses) of the 3+1 sterile neutrino mixing parameters from separate fits to the different experimental data: gallium (blue), reactors (green) and ν_e $-^{12}$C (magenta). The red line and red cross corresponds to a combined fit.. The best fit values are listed in Table 4.3. [114]

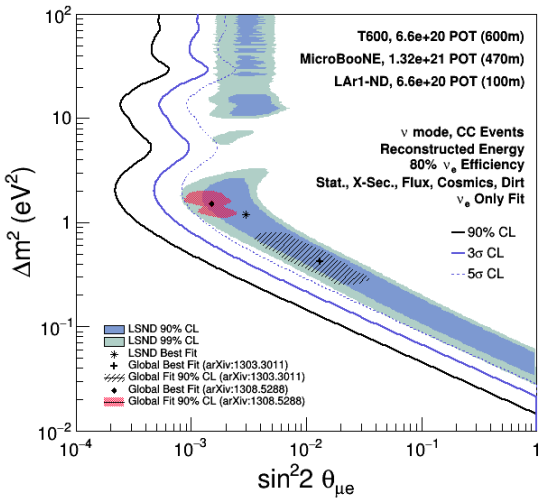

Figure 4.17.: Estimated sterile neutrino sensitivity limit for Fermilab SBL neutrino program [51] utilising three liquid argon detectors at distances 110m, 470m and 600m from the beam target.

- The OscSNS [116] project propose to use neutrinos from Spallation Neutron Source accompanied with Gadolinium-doped liquid scintillator detector.
- The IsoDAR approach, included in the Daeδalus program [105], relies on the production of ^{8}Li and its β-decays.

The reactor-based search for sterile neutrinos, a scintillator detector (plastic or liquid) is placed at few meters away from the reactor core. The existence of sterile neutrinos can be probed by observing the energy spectrum of reactor neutrinos. There are many ongoing projects around the world. The Nucifer [117] will use about 1 ton of gadolinium-doped scintillator target at the distance of 7 meters away from 70 MW_{th} Osiris research reactor at Saclay and the Stereo experiment [118] uses a segmented liquid scintillator detector in ILL research reactor at Grenoble. The DANSS experiment [119] aims at 1 m^3 of the highly segmented plastic scintillator detector to be located next to one commercial reactor the Kalinin nuclear power plant in Russia. All of the experiments mentioned above are able to probe the sterile neutrino oscillation parameter space around the values indicated by the global fit ($\Delta m^2_{14} \approx 1$ eV^2, $\sin^2 2\theta_{14} \approx 0.1$).

The Borexino-SOX experiment [120] will use intensive ^{144}Ce-^{144}Pr (phase-I) and ^{51}Cr source (phase II) with neutrinos detected in the liquid scintillator detector Borexino. The deficit of electron antineutrino events from cerium and electron neutrino events from chromium are looked for. The example of event spectra in which the oscillation pattern is clearly visible and the sterile neutrino sensitivity reach of Borexino detector is shown Figure 4.18. The method is discussed in detail in Chapter 9 of this thesis in the context of LENA.

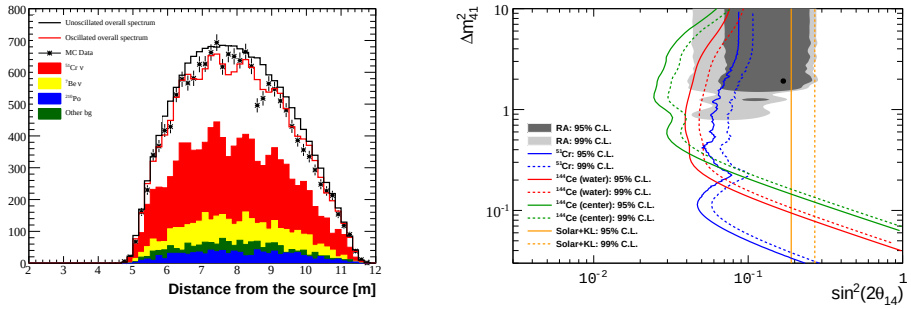

Figure 4.18.: Sterile neutrinos with Borexino-SOX [120]. Left panel: The illustration of spatial event distribution and its components in Borexino-SOX experiment with ^{51}Cr source ($\sin^2 2\theta_{14}$=0.3, Δm^2_{41}=2 eV^2). Right panel: Estimated sterile neutrinos sensitivity for external ^{51}Cr and the ^{144}Ce-^{144}Pr source deployed in the volume water buffer (muon veto) or in at the centre of the scintillator vessel in Borexino.

Part II.

Liquid Scintillator Technique

5. Liquid Scintillator Technique in Neutrino Physics

Various liquid scintillator (LS) detectors, like KamLAND [121], Borexino [122], LSND [123], Double Chooz [124], Daya Bay [64] and RENO [125] have served the neutrino and astroparticle physics for detecting low-energy neutrinos and antineutrinos, with energies ranging from few hundreds of keV to several tens of MeV. The main part of the original research work of this thesis concerns with the scintillator detection technique for neutrinos from various sources with low energies, but also extending the neutrino energies to 1-10 GeV range. This chapter introduces the detection principle of the liquid scintillator detectors.

5.1. Detection Principle

The observation of particles with liquid scintillator detector is based on the detection of light produced by charged particles traversing scintillating medium. Charged particles propagating in the medium ionise and/or excite molecules and the scintillation photons are emitted isotropically in the subsequent deexcitation process of the molecules. The scintillating medium is usually based on solvent containing organic molecules with benzene rings, like PC (pseudocumene) in Borexino [122] or LAB (linear-alkyl-benzene) in SNO+ [126].

To avoid the emitted photons to be reabsorbed a small amount of wavelength-shifting solute is usually mixed to the solvent. This makes the scintillating target material more transparent to the photons and they can travel longer distances allowing them to be detected in photomultipliers surrounding the scintillating material. In Borexino and SNO+ PPO (2,5-diphenyloxazole) is used as wavelength-shifting solute. The concentrations are 1.5 g/l and 2 g/l, respectively [122] [126].

Typically organic scintillator emits of the order of 10 000 photons per 1 MeV of deposited energy. The number of registered photons sets a limit to the energy reconstruction capability of the detector. This is affected by the optical properties of the scintillator medium (see Table 6.1), the photo-coverage (typically $\sim$30%), the quantum efficiency of the photo-sensors, and the effectivity of read-out electronics. Liquid scintillator detectors are in general considered to have good energy resolution. For example, in Borexino the energy resolution is approximately 5% at 1 MeV of deposited energy [127]. Due to the isotropic emission of the scintillation light, the position and the deposited energy of the low-energy events can be reconstructed using

the measured time differences and photon intensities in different photosensors as an input for point-fitting algorithm. The most optimal shape to collect light is sphere.

Another important feature of the liquid scintillator technique is the low excitation energy (∼eV) of the molecules producing the scintillation light. That would, in principle, allow the measurement of relatively low-energy deposits without a threshold. On the other hand, a lower limit on the neutrino-induced energy deposits is set by the residual radioactivity intrinsic to the detector materials. The background levels heavily depend on the materials used in the detector, as well as on the materials surroundings of the detector. Typically the low-energy limit is of the order of ~ 200 keV, due to the intrinsic ^{14}C contamination of the scintillator material itself. Different background sources are introduced later in this Chapter.

The light yield of the scintillation process can be described with empirical Birk's formula:

$$\frac{dL}{dx} = \frac{A\frac{dE}{dx}}{1 + k_b\frac{dE}{dx}}. \tag{5.1}$$

It relates the light yield dL to the energy deposition dE in the path length of dx. The absolute scintillation efficiency of the material A and the Birk's constant k_b are experimentally determined parameters which depend on the scintillator material and the particle type of the traversing particle. The Birk's constant k_b describes so-called quenching effects.

The time structure of scintillation photon emission of the scintillator material depends on the deexcitation times of the excited states. This can be modeled by the formula

$$F(t) = \sum_i N_i e^{-t/\tau_i}, \tag{5.2}$$

where τ_i is the time constant of the excited state i, and N_i is the mean fraction of photons that are emitted with that time constant (such that $\sum_i N_i = 1$).

The time constants, mean fractions and Birk's constants for Linear-Alkyl-Bentzene (LAB) are tabulated, for an example, in Table 5.1.

5.2. Signals of Neutrino Interactions in Liquid Scintillators

For neutrino interactions the scintillation light is produced by the final state particles and/or subsequent decay(s) of final state nuclei originating in the interaction. The temporal structure of scintillation light emission and the look for delayed light emission can be used to discriminate different kinds of neutrino interactions as well as to separate the desired neutrino signal from background.

	Electrons	Alphas
N_1	0.71	0.44
N_2	0.22	0.16
N_3	0.07	0.40
τ_1	4.6 ns	3.2 ns
τ_2	18 ns	18 ns
τ_3	156 ns	190 ns
k_b	0.15 mm/MeV	0.11 mm/MeV

Table 5.1.: The photon emission parameters for Linear-Alkyl-Bentzene (LAB) according to [128].

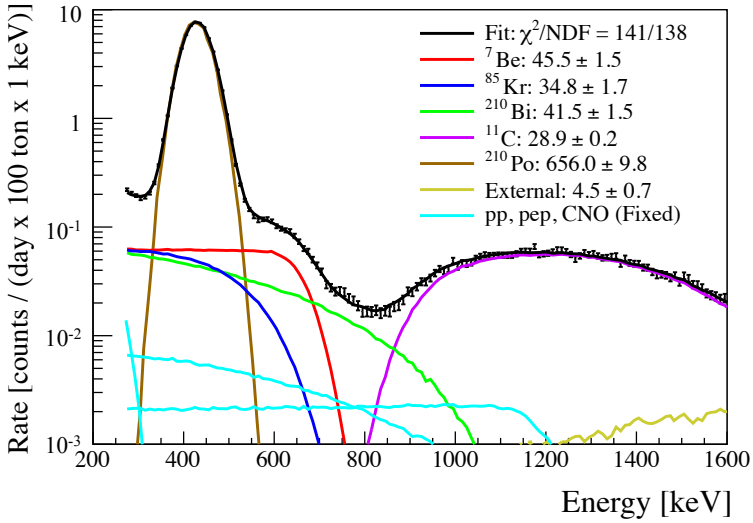

Figure 5.1.: The measured and fitted energy spectrum of solar neutrinos recorded in the Borexino experiment. [127]

5.2.1. Low-energy Neutrinos

Neutrino-Electron Scattering

In the neutrino-electron scattering

$$\nu_l + e^- \rightarrow \nu_l + e^- \ (l = e, \mu, \tau) \tag{5.3}$$

the energy transfer from initial neutrino to the final state electron can vary between 0 and $T_{\max}$ and the maximum kinetic energy of the final state electron $T_{\max}$ depends on the energy of the neutrino (see Equation 2.13). Even if the inital neutrinos are mono-energetic they will produce a flat shoulder-like (visible) energy spectrum of recoil electrons. That makes the unambiguous determination of the initial neutrino energy impossible. Furthermore, as the reaction holds for all neutrino flavors, there is no way to make flavor discrimination.

The neutrino-electron scattering is the main channel for solar neutrino measurement in liquid scintillators. The measured recoil electron energy spectra of Borexino experiment is shown in Figure 5.1. The shoulder-like contribution of the mono-energetic ^{7}Be neutrinos is visible. For the neutrinos with the energy spectrum, e.g. ^{8}B neutrinos from the Sun, the spectral shape affects the visible energy spectra.

Inverse β Decay reaction

For the inverse beta decay reaction

$$p + \bar{\nu}_e \rightarrow n + e^+ \tag{5.4}$$

the positron and neutron in the final state allows a clear event signature. A prompt signal results from the ionisation of positron and from gamma-rays from its annihilation. As most of the neutrino energy is transferred to the positron, this prompt signal contains the energy and time information of the event. The observed energy, also called visible energy is related to the initial neutrino energy with $E_{\text{vis}} \approx E_\nu - E_{\text{thr}} + 2 \times m_e \approx E_\nu - 0.78$ MeV. The delayed signal originates in the capture of the neutron by a free proton, resulting in deuteron and 2.2 MeV gamma-ray emission. Typically, in an un-doped scintillator the capture happens ~ 250 μs later than the prompt signal. This delayed signal allows very efficient tagging of inverse beta decay reactions. To shorten the time between neutron emission and capture and to increace the energy gamma emission, the scintillator can be doped with a substance having a high neutron capture cross section, like gadolinium. This shortens the capture time to ~ 30 μs and increases the energy of the gamma emission. In case of ^{157}Gd gamma-ray emission is increased to 8 MeV.

Elastic neutrino-proton scattering

Apart from the ν_e scatterings, the elastic scattering of neutrino can also occur with a proton:

$$\nu_l + p \rightarrow \nu_l + p \ (l = e, \mu, \tau), \tag{5.5}$$

Due to the proton mass and the quenching effect, the amount of scintillation light is significantly lower than that of electron. Hence, at lowest energies this reaction does not play any crucial role. The importance of this channel grows as the neutrino energy becomes higher, for instance in the detection of the muon and tau neutrinos originating in supernova bursts.

Reactions on Carbon

The relevant reactions on ^{12}C and ^{13}C accompanied by their threshold energies are

$$^{12}\mathrm{C} + \nu_\mathrm{e} \rightarrow ^{12}\mathrm{N} + \mathrm{e}^- \quad (17.34 \text{ MeV}) \tag{5.6}$$

$$^{12}\mathrm{C} + \bar{\nu}_\mathrm{e} \rightarrow ^{12}\mathrm{B} + \mathrm{e}^+ \quad (13.37 \text{ MeV} \tag{5.7}$$

$$^{13}\mathrm{C} + \nu_\mathrm{e} \rightarrow ^{13}\mathrm{N} + \mathrm{e}^-. \tag{5.8}$$

$$\tag{5.9}$$

In these reactions the tagging relies on finding the coincidence between prompt signal from electron or positron and the delayed signal originating in subsequent $\beta^\pm$ decay. Event signature resembles inverse beta decay reaction. In this case observing the coincidence of the prompt and delayed signals is more difficult due to wide energy spectrum of final state electrons originating in the beta decays and also due to their longer half-lifes (from 10 ms to 900s depending on the channel).

5.2.2. High-Energy Neutrinos

At the higher neutrino energies, the variety of possible final state particles and their combinations grows and the spatial ranges of the final state particles increase. The energy deposition to the target medium can not anymore be considered as a simple point-like event. That makes the event reconstruction more complicated and in many cases impossible. The neutrino energies 1-10 GeV are important for atmospheric neutrinos and high-energy beam neutrinos. For them the event reconstruction aims to the sufficient energy measurement needing the discrimination between muon and electron neutrino initiated events and the reconstruction of the direction of the initial state neutrino. The rejection of the neutral current interactions is also important as the final state neutrino carry part of the energy away from the detector, making the reconstruction unreliable.

In the simplest event category of quasi-elastic scattering

$$\nu_\mu + n \rightarrow p + \mu^- \quad \text{and} \quad \bar{\nu}_\mu + p \rightarrow n + \mu^+ \tag{5.10}$$

$$\nu_e + n \rightarrow p + e^- \quad \text{and} \quad \bar{\nu}_e + p \rightarrow n + e^+, \tag{5.11}$$

the major part of scintillation light produced originates in the final state charged lepton ($\mu^\pm$,$e^\pm$). If the discrimination between muon is possible the energy reconstruction is also possible with a single track fitting. In case of LENA, the overall energy resolution of the order of 9% can be reached, providing that the event is fully contained in the detector active volume [129]. The fractions of resonant pion production reactions

$$\nu_\mu + n \rightarrow \Delta^+ + \mu^- \rightarrow p + \pi^0 + \mu^-, \tag{5.12}$$

and deep inelastic scattering reactions increase with neutrino energy (see. Figure 2.5). At the moment there are not known method to fully de-convolute the light-production of the different final state particles and these event categories are usually considered as background. The rejection of them is based on finding the subsequent signals from decays or captures of muons and captures of neutrons. In addition an elementary tracking algorithms, which search the most probable light-emission locations, have been recently developed. This will be discussed in context of LENA in Chapter 10.

For the neutral current interactions, the final state charged lepton is replaced with corresponding neutrino not producing any signal in the detector. The amount of light produced is then considerably less than in corresponding charged current events. Figure 5.2 shows the response matrices for electron neutrino interactions illustrating the energy reconstruction capability of LENA detector [129]. The left panel shows the considered signal (quasi-elastic charged current interactions) and the right panel the corresponding reconstruction of neutral current events. The broad distribution of the reconstructed energies of the neutral current events is visible.

5.3. Background Sources

As the signals of neutrinos are rare and usually weak, it is important to understand the background signals originaing from different sources. The background levels depend on the experimental setup and surroundings of its location. The sources of the background can be divided into two categories: the radioactivity inside or nearby the detector, and the background induced by cosmic-ray muons.

The intrinsic background originates in the target medium or other detector materials like photomultiplier tubes, support structures or the vessel containing the target medium. The major components of these intrinsic background sources are the following:

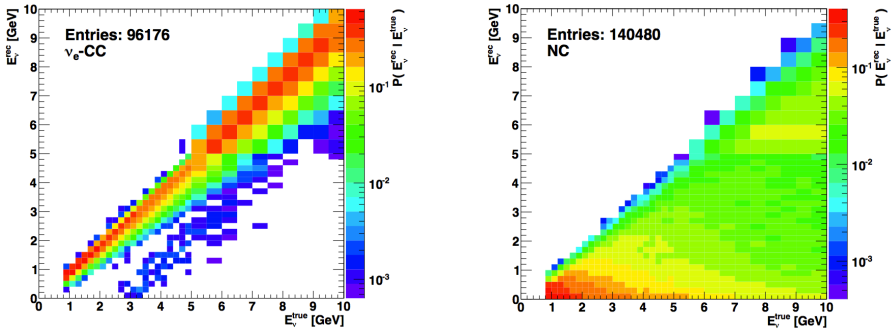

Figure 5.2.: The energy response of the LENA for electron neutrino charged current events (left) and corresponding neutral current events (right) [129].

- Radioactivity of the scintillator material itself. As the liquid scintillator is made of organic material (petroleum), it will always contain some amount of β-decaying active carbon isotope ^{14}C with the end-point energy of 156 keV. This ^{14}C contamination sets the lower limit to the experiments visible energy window and is typically 250 keV. Removal of the ^{14}C from the scintillator is not possible in practice for large detectors.

- Radioactive contamination can enter to the scintillating medium as the surface contamination, for example as dust, on the detector materials. Typical elements are those of uranium and thorium decay chains. Careful cleaning and proper selection of the detector materials reduce this background considerably. The detector setup must also be sealed against the diffusive isotopes like radon and krypton present in air.

- The gamma rays from the detector materials and also from the detector surroundings (the walls, floor, ceiling) can penetrate into the active volume, interact there and produce light. Especially, the glass of photomultiplier tubes contains gamma-active ^{40}K with the gamma-ray energy of 1.46 MeV. To reduce the background induced by gamma radiation the material selection and low background photosensors are the key issues. Against the external gammas a shielding of the detector is usually necessary. The gamma-induced background can be further reduced by limiting the fiducial volume properly in the analysis phase.

The background induced by cosmic-ray muons consists of the following components:

- Cosmic-ray muons can traverse long distances in rock and enter to the detector producing enormous amount of scintillation light. These events cause

background for example for signals originating from atmospheric neutrinos. The high light output of cosmic muon event makes impossible to observe also the weak signals originating from low-energy neutrinos. The flux of these high-energy muons can be reduced by locating the detector deep underground and equipping it with an active muon veto detector, typically water-Cherenkov detector.

- Through-going muons can induce radioactive isotopes into the active volume of the detector. These can be, for example, the radioactive carbon isotopes, like ^{11}C and ^{10}C, from the muon knocking out neutrons from ^{12}C or neutron-rich isotopes from spallation process (e.g. ^{8}He, ^{9}Li). The rejection of this background is based on the tracking the through-going muon and vetoing the detector or part of it for a sufficiently long time window after the muon passing.
- High-energy cosmic muons can knock out neutrons also from the rock. These fast neutrons can drift several meters and end up to the detector and produce a signal. These neutron signals cannot be associated with the veto signal and the only way to reduce them is to construct the detector in the deep location to reduce the cosmic muon flux and equip the detector with the sufficient thick buffer to catch most of the neutrons before the active volume.

The lowest levels of backgrounds have been achieved in the Borexino experiment. The full description of them can be found in the reference [127].

5.4. Major Achievements and Future of LS Technique

Since 1950's the liquid scintillator detectors have played a crucial role in many of the neutrino physics problems, for instance

- First neutrino observation by F. Reines and C. Cowan in 1956 [13].
- The confirmation of the neutrino oscillation by using reactor neutrinos by KamLAND experiment [121].
- Observation of signal from geoneutrinos by KamLAND and Borexino experiments [130] [131].
- The precision measurement of solar ^{7}Be neutrinos, evidence of solar pep neutrinos, and observation of even lower energy solar pp-neutrinos with Borexino experiment [132] [133] [134].
- The three independent measurement of the neutrino mixing angle θ_{13} by the reactor neutrino experiments Double Chooz, Daya Bay and RENO [124] [64] [125].

In addition the LSND experiment observed neutrinos from the beam dump of LAMPF [9]. The controversial observation of the excess of electron neutrino events were made. The results are discussed in Chapter 4 more in detail. The KamLAND experiment have also extended the physics program to include the double beta decay studies by positioning a ^{136}Xe source inside the scintillation volume and setting new limits to the half life of the neutrinoless double beta decay [96].

To achieve new discoveries, the former water-based Cherenkov detector SNO is being converted to LS detector SNO+ [100]. The filling of the detector is expected during 2016. The physics program will consist of, especially, the neutrinoless double beta decay measurement with ^{130}Te. The measurement with radioactive neutrino sources and utilising the Borexino detector (SOX) is under preparations [120]. Within the decade, the next large-scale project will be the measurement of neutrino mass hierarchy with next-generation LS detector. Two collaborations have showed the interest to construct of the order of 20 kiloton LS detectors at 55-60 km from nuclear power plant complexes. The JUNO experiment [2] in China is under construction and RENO-50 [65] in South Korea is in design study phase. The construction of either one or both of these detectors does not sweep away the need of even larger detector dedicated, especially, to astroparticle physics. The next chapter will introduce the LENA project [1] and its physics program proposed for that purpose. There is also interest to construct 30-100 kiloton detector with water-based liquid scintillator (WbLS) [135] as a target materal. The project is called THEIA [136] and it is based on the The Advanced Scintillation Detector Concept (ASDC) [137].

6. LENA Project

LENA (Low Energy Neutrino Astronomy) has been proposed as a next-generation large liquid scintillator detector [1]. The aim is to construct a large detector deep underground that would serve as a multipurpose detector probing neutrinos from astrophysical sources (the Sun, supernovae) and geoneutrinos. In addition it would have capability to determine fundamental particle properties, like neutrino oscillation parameters and observe the proton decay or set the limit for the life-time of the proton substantially more stringent bound than the existing one. To achieve, for instance, the observation of diffuse supernova neutrino background flux, the active mass of the detector have to be of the order of 50 kton and operational time 10 years [1] [138].

The extensive design study of LENA detector setup have been performed in pre-feasibility and feasibility studies, and as a part of the LAGUNA and LAGUNA-LBNO Design Studies [4]. The design studies covered mainly the construction of the detector deep underground from the logistics and rock mechanical point of view and the long term operation of the detector. In the Design Studies also the physics programs possible to be carried through in the experiment, especially by using a high-energy neutrino beam, were investigated.

In this chapter the baseline design of the LENA detector is introduced and the main physics goals and expected results are described. In the final section we briefly describe the simulation environment which has been used to determine the detector response for various kinds of neutrino and background sources and where the major part of the present thesis work has been performed.

6.1. Detector Setup

A schematic of illustration of the LENA detector setup is presented in Figure 6.1 showing the main detector components. As in many other large liquid scintillator detectors, the active part in the middle is surrounded by inward-looking photosensors. These are enclosed into a light-tight tank, surrounded by water layer acting as a shielding against radioactivity and an active muon veto detector.

The active scintillator target of the LENA detector consists of $\sim$50 kton of linear alkylbenzene (LAB) with small amounts of 2,5-diphenyl-ozazole (PPO) and 1,4-bis-

Physical and Chemical data		Optical properties	
Chemical formula	$C_{18}H_{30}$	Refractive index n	1.49
Molecular weight	241	Relative light yield y	1.
Density (g/cm^3)	0.863	Absorption maximum (nm)	260
Flash point (°C)	140	Emission maximum (nm)	283
Viscosity (cps)	4.2	Attenuation length (m)	∼20
Molecular density (10^{27}/m^3)	2.2	Rayleigh scat. length	25
Free protons (10^{28}/m^3)	6.6		
Carbon nuclei (10^{28}/m^3)	4.0		
Total p and e^- (10^{29}/m^3)	3.0		

Table 6.1.: Overview of the basic properties of Linear-Alkyl-Benzene (LAB). [1]

(o-methylstyryl)-benzene (bisMSB) acting as wavelength shifters, transforming the scintillation emission spectrum to the wavelength range 400-430 nm in which the detector material is the most transparent and the photomultiplier tubes most efficient. The basic properties of the LAB are shown in Table 6.1 and the scintillatons related parameters are presented in Table 5.1.

The active scintillation volume is surrounded with the support structure with the radius of 14 m, on which the optical modules are mounted. The support structure stands completely inside the liquid scintillator and hence the space between the support structure and the tank wall is filled by the scintillator liquid. The support structure is also equipped with the optical shielding preventing the light originating in the events occurring outside of the target volume of the detector leaking into the innermost target volume.

The scintillation light created by the particles traversing in the active scintillator material are detected with photomultiplier tubes (PMTs). As high pressure increases the risk of implosion, the PMTs are encapsulated. This prevents the chain reactions of the kind that happened in Super-Kamiokande and also provides the non-scintillating buffer in front of PMT. The encapsulation acts also as a light concentrator increasing the photo-coverage. In the baseline design of LENA, 12-inch photomultipliers (Hamamatsu R11780) are considered and the total number exceeds 30 000. Characterisation of this particular type of PMT model is presented in [139]. The schematic drawing of the optical module is shown in Figure 6.2. In the KamLAND and Borexino detectors, the active scintillation volume is enclosed into a nylon vessel surrounded by buffer liquid. In LENA the different approach is used. The buffer liquid is included in encapsulation of the photomultipliers. The buffer liquid acts as a shield against the internal radioactivity of the PMT itself.

All the components described above are placed inside the steel tank supported

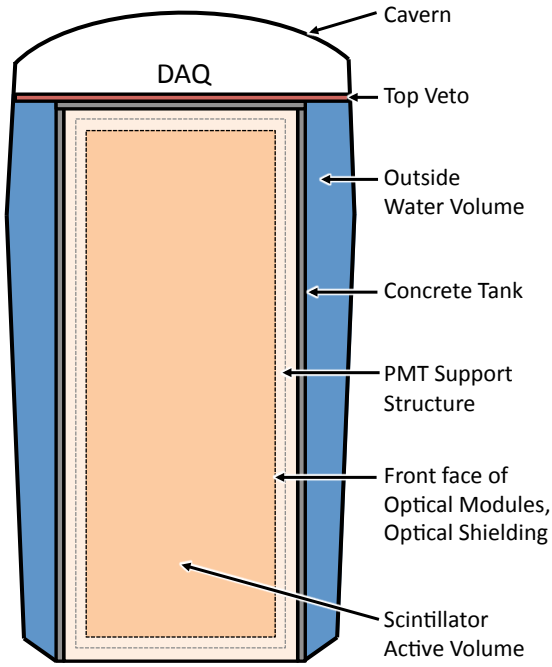

Figure 6.1.: Main components of LENA detector.

by concrete structure and surrounded with water buffer between the cavern and tank walls. The inside surface of the tank is covered with stainless steel or plastic lining. The water buffer is to be instrumented with photomultipliers, and it acts as a buffer against the gamma rays and neutrons from the rock and also as an active muon veto (water-cherenkov) detector. On the top of the tank there is a $\sim$2m thick scintillator layer and an additional active muon veto detector consisting of layers of gas-filled detectors, like drift chambers or limited streamer tubes or plastic scintillator detectors. More detailed construction phases and estimated construction plan including timeframe are described in the final reports of the LAGUNA and LAGUNA-LBNO Design Studies [4].

In LAGUNA and LAGUNA-LBNO Design Studies [4] seven sites across the Europe to hold the next-generation large neutrino detector, including LENA, were studied. The Pyhäsalmi mine in Finland was found to be the most feasible location for LENA detector due to its great depth (1430 m), rock quality allowing the excavation of the large cavern and the background conditions. The structure of the mine and the

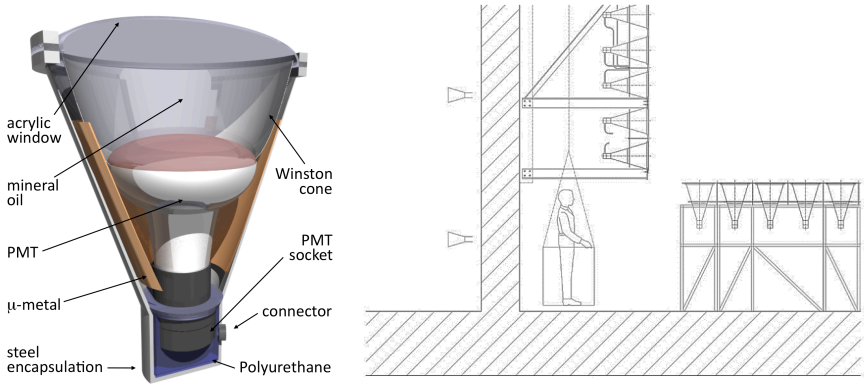

Figure 6.2.: Optical module design for LENA and their mounting to the walls and the floor of the tank.

design of the large caverns at the depth of 1.4 km are illustrated in Figure 6.3. The advantages of locating large detector in Pyhäsalmi mine have been presented more in detail in [140] [141] [142] [143].

6.2. Physics Program

The main advantages of LENA detector are its considerably larger active mass, improved photosensors and improved data acquisition system compared with the existing liquid scintillator detectors ($\sim 50\times$ KamLAND or SNO+, $\sim 150\times$ Borexino). This accompanied with the expected measurement time (> 10 years) allows for measurements with unprecedented accuracy and also opens a window for new discoveries. The physics prospects of the LENA are presented in [1] and are described in the following.

6.2.1. Solar Neutrinos

The size and the expected low detection threshold of electron neutrinos (≈ 250 keV) results in high statistics solar neutrino measurements. The expected solar neutrino event rates in LENA are given in Table 6.2.

The high event rate of ^{7}Be, about 10^4 events per day, allows the search of periodic modulations of the solar neutrino flux in the time scales ranging from few minutes

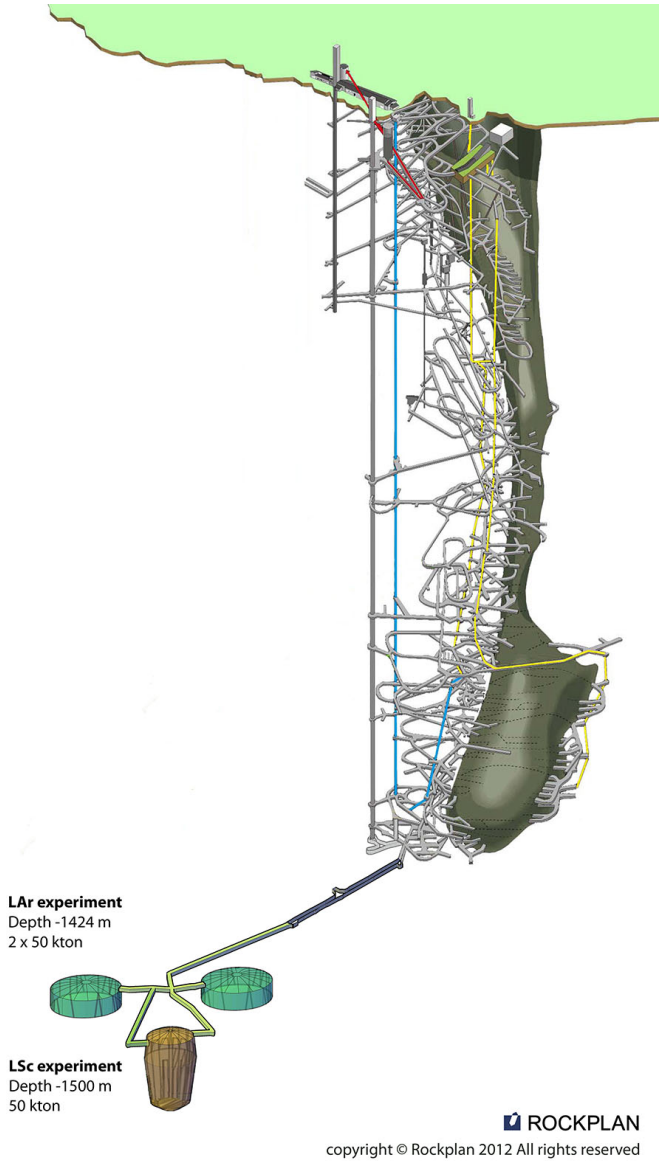

Figure 6.3.: Schematic view of the Pyhäsalmi mine and the two large caverns for liquid-Argon (LAr) detectors and one for scintillator detector LENA (LSc).

Source	Channel	EW [MeV]	m_{fid} [kt]	Rate [cpd]
pp	$\nu e \rightarrow e\nu$	>0.25	30	40
pep		0.8−1.4	30	2.8×10^2
^{7}Be		>0.25	35	1.0×10^4
^{8}B		>2.8	35	79
CNO		0.8−1.4	30	1.9×10^2
^{8}B	^{13}C	>2.2	35	2.4

Table 6.2.: Expected solar neutrino rates in LENA [1]. The fiducial target mass m_{fid} is specific for each solar neutrino component and set by the rejection of expected energy dependent gamma-ray induced background.

to several years. The precision better than 1% could be reached. This would make it possible to study the temperature variations in the central region of the Sun, helioseismic g-mode i.e. the density variations and possible variations of the fusion rate for the first time using neutrinos. These studies are expected to shed new light to the mechanism behind the eleven-year solar activity cycle.

The measurement of ^{8}B with LENA would allow to test so-called MSW-LMA prediction i.e. how the survival probability of the solar neutrinos depends on the neutrino energy. The Figure 6.4 shows the expected behaviour according to the MSW-LMA solution and the measured data points from different solar neutrino experiments. The LENA experiment will be able to study especially the transition from vacuum dominated $\lesssim$1 MeV region to matter dominated region $\gtrsim$ 5 MeV beyond the reach of current and past solar neutrino experiments. The deviation form the predicted behaviour can be measured with 5σ significance within five years [144]. The deviation would implicate new physics e.g. non-standard interactions or sterile neutrinos.

The high event statistics achievable in LENA allows also one to observe the faint neutrino signal from the CNO energy production chain of the Sun. The CNO fluxes are connected to the metallicity of the Sun i.e the abundance of elements heavier than helium, on which the CNO neutrino observations would bring valuable information.

6.2.2. Supernova Neutrinos

LENA is expected to observe of the order of 1.5×10^4 events from core-collapse supernova explosion occurring at the distance of about 10 kpc (in the Milky Way). The Table 6.3 summarises the expected event rates from different channels. The main channel is inverse β decay providing energy spectrum of electron antineutrinos with an distinctive delayed coincidence signal. Accompanied with other charged-current reactions on carbon and their subsequent signals from decays will give a handle to

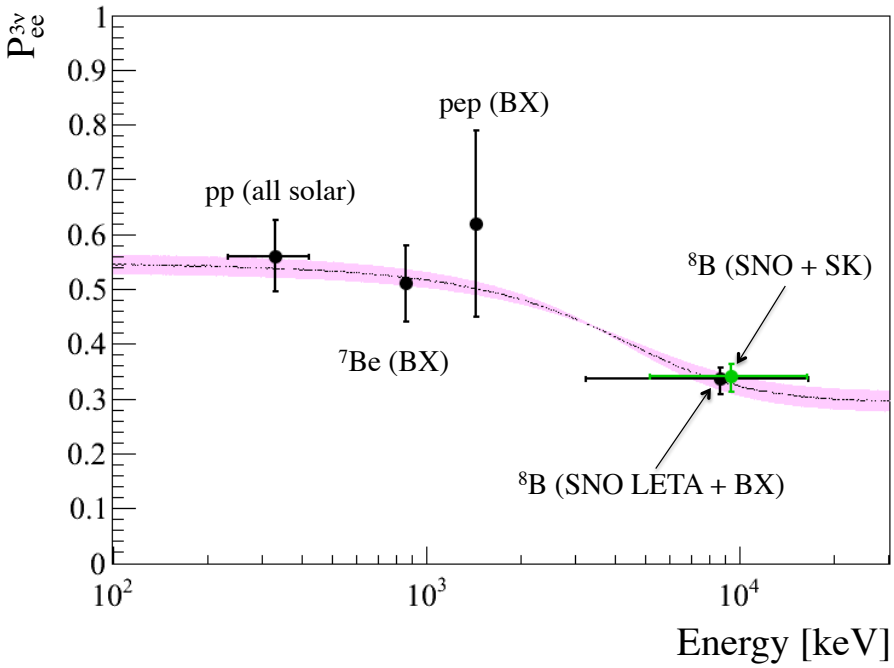

Figure 6.4.: Energy dependent survival probability if solar neutrinos [127]. The shaded area denotes the allowed region (1σ) of the MSW-LMA prediction. The current measured survival probabilities from solar neutrino experiments are also shown.

Reaction	Type	Events for $\langle E_\nu \rangle$ values		
		12 MeV	14 MeV	16 MeV
$\bar{\nu}_e\, p \rightarrow n\, e^+$	CC	$1.1{\times}10^4$	$1.3{\times}\ 10^4$	$1.5{\times}\ 10^4$
$\nu\, p \rightarrow p\, \nu$	NC	$1.3{\times}10^3$	$2.6{\times}10^3$	$4.4{\times}10^3$
$\nu\, e \rightarrow e\, \nu$	NC	$6.2{\times}10^2$	$6.2{\times}10^2$	$6.2{\times}10^2$
$\nu\, {}^{12}\mathrm{C} \rightarrow {}^{12}\mathrm{C}^*\, \nu$				
${}^{12}\mathrm{C}^* \rightarrow {}^{12}\mathrm{C}\, \gamma$	NC	$6.0{\times}10^2$	$1.0{\times}10^3$	$1.5{\times}10^3$
$\bar{\nu}_e\, {}^{12}\mathrm{C} \rightarrow {}^{12}\mathrm{B}\, e^+$				
${}^{12}\mathrm{B} \rightarrow {}^{12}\mathrm{C}\, e^-\, \bar{\nu}_e$	CC	$1.8{\times}10^2$	$2.9{\times}10^2$	$4.2{\times}10^2$
$\nu_e\, {}^{12}\mathrm{C} \rightarrow {}^{12}\mathrm{N}\, e^-$				
${}^{12}\mathrm{N} \rightarrow {}^{12}\mathrm{C}\, e^+\, \nu_e$	CC	$1.9{\times}10^2$	$3.4{\times}10^2$	$5.2{\times}10^2$

Table 6.3.: Expected event rates in LENA for neutrinos originating in a supernova at a distance of 10 kpc. Here ν stands for a neutrino or antineutrino of any flavor. The NC rates are summed over all flavor channels. The three representative values for $\langle E_\nu \rangle$, (12 MeV, 14 MeV and 16 MeV) are assumed to be the same for all flavors. [1]

discriminate the fluxes of $\bar{\nu}_e$ and ν_e. On the other hand, the signals from neutral current interactions are sensitive for all neutrino flavors. In addition, in a real-time detector, like LENA, the time evolution of the event rate from the burst of supernova neutrinos is also detectable. This kind of high statistics measurement with a lower detection threshold compared with that of the water-Cherenkov detectors, would be valuable for improving the models of core-collapse supernova explosions. Furthermore, the indication of neutrino mass hierarchy might also be visible.

LENA should also be able to detect the cumulative weak glow of the few MeV neutrinos and antineutrinos from distant core-collapse supernovae. It is estimated that within the 10 - 25 MeV energy window 2 -10 events per year due to this diffuse supernova background (DSNB) will be detected via the inverse beta decay channel. The lower limit for the energy window depends on the level the reactor neutrino flux which would dominate the electron antineutrino flux below it. At the energies above 25 MeV the atmospheric neutrino background exceeds the DSNB signal.

6.2.3. Geoneutrinos

In the context of geoneutrinos, LENA would be the first high statistics measurement collecting $\sim 10^3$ events per year from decay chains of ^{238}U and ^{232}Th. The energy spectra of geoneutrinos (<4.5 MeV) and neutrinos from nuclear reactors (<14 MeV) are heavily overlapping and therefore a distant location of the detector from nuclear

reactors is preferred. Although, the reactor neutrino events can be subtracted statistically from the geoneutrino energy window, they anyhow impose a systematic uncertainty to the geoneutrino measurement.

The accuracy of the measurement of total geoneutrino flux at sub-percent level is possible to reach with LENA. That would significantly improve the estimates of radiogenic heat produced inside the Earth and shed light to the fractions of different energy sources allowing for example the plate tectonics. As the energy spectra of geoneutrinos originating the decay chains of uranium and thorium are not fully overlapping the separation of their contributions to the total event rates is possible. The accuracy down to to 3% and 5% levels, respectively, in 10-year measurement would be achievable. The special interest of geologists is the ratio of the thorium to uranium abundances giving information on the accretion of the elements in the crust and mantle. A detector with a specifications of LENA would be able to determine that with 10% accuracy. The geoneutrino measurements and their sensitivities are discussed in Chapter 8.

6.2.4. Atmospheric Neutrinos

The most significant results concerning atmospheric neutrinos, have been so far obtained by the 50 kton water-Cherenkov detector Super-Kamiokande [23] [145]. A LENA type detector would have the same fiducial mass but a 50 times higher light yield than the Super-Kamiokande and it would outperform the water-Cherenkov detector in energy resolution. Hence a good determination of fluxes and angular spectrum is expected up to few tens of GeV with it.

The performance of the detector depends on the ability to identify the neutrino flavor (ν_e or ν_μ) in charged current reactions. The tracking procedures, also developed in this thesis and presented later on, are aimed to achieve a good flavor discrimination. Other important requirement is the discrimination of neutral current events from the charged-current ones. Crucial is the ability to separate π^0 induced events from ones induced by ν_e and the charged $\pi^\pm$ from $\mu^\pm$.

With sufficient energy and angular resolution the following physics issues can be dealt with: i) a high statistics measurement of θ_{23} and Δm^2_{32} can be carried out by employing muon neutrinos with entrance angles varying from vertical to horizontal directions and the oscillations can be verified in an energy region not probed before, and ii) neutrinos below the horizontal plane open a window to look at the matter enhancement of the oscillation probabilities and determine the mass hierarchy of the neutrinos.

Channel	Lower limit 90% C.L.
$p \to e^+ + \pi^0$	$\tau_p = 8.2 \times 10^{33}$
$p \to \mu^+ + \pi^0$	$\tau_p = 6.6 \times 10^{33}$
$p \to K^+ + \bar{\nu}$	$\tau_p = 2.3 \times 10^{33}$
$n \to K^0 + \bar{\nu}$	$\tau_p = 1.3 \times 10^{33}$
$p \to K^0 + \mu^+$	$\tau_p = 1.3 \times 10^{33}$
$p \to K^0 + e^+$	$\tau_p = 1.0 \times 10^{33}$

Table 6.4.: The nucleon decay channels probed by Super-Kamiokande experiment and the lower limit for the life-time of the corresponding nucleon [147] [148]. The first two reactions are favoured by minimal Grand Unified Theories and latter ones by supersymmetric GUT models.

6.2.5. Proton decay

The Grand Unified extensions of the Standard Model predict that the nucleons are not a stable particles [146]. The most stringent limits on the proton lifetime are provided by the Super-Kamiokande experiment. It results for the different decay channels predicted by the minimal SU(5) Grand Unified Theory are listed in Table 6.4

The reaction $p \to K^+ + \bar{\nu}$ is the most interesting reaction from the point of view of liquid scintillator detectors because the signals from K^+ (prompt) and delayed signal from its decay products would be visible. The lower limit of $\tau_p > 4 \times 10^{34}$ years would be be achievable in LENA [149].

6.2.6. Long Baseline Neutrino Oscillations

The physics potential of the LENA detector using the high-energy neutrinos form particle accelerators was investigated in the LAGUNA-LBNO Design Study [4]. The capability of determining the neutrino mass hierarchy and to observe CP-violation were studied by assuming a high-energy neutrino beam with a baseline of 2288 km (from CERN to Pyhäsalmi mine).

In Figure 6.5 and 6.6 we demonstrate the sensitivity of the LENA detector to determine the mass hierarchy. In Figure 6.5 the median sensitivity, using the GLoBES software [69] [70], is as a function of the CP angle δ for two beam exposures (3×10^{20} p.o.t. and 1.5×10^{21} p.o.t.) assuming 50% - 50% neutrino-antineutrino run times separately for fully contained events (left panel of Figure 6.5) and all events (right panel of Figure 6.5). In Figure 6.6 the power to select true hierarchy and reject the false one is presented for fully contained events as a function of the exposure for normal hierarchy (NH, Figure 6.6 left panel) and for the inverted hierarchy

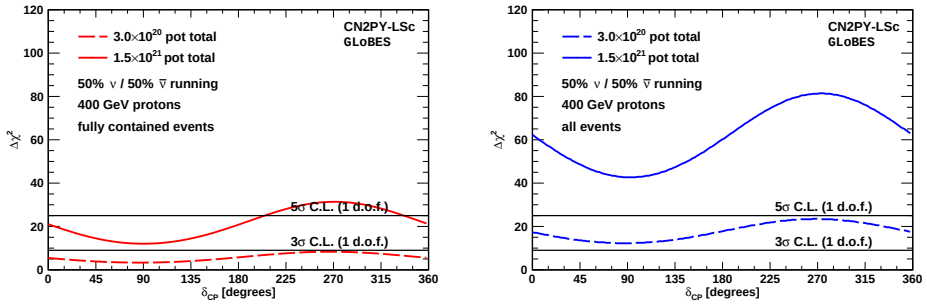

Figure 6.5.: Median sensitivity of the mass hierarchy determination with LENA baseline design with fully contained (left) and all events (right).

(IH, Figure 6.6 right panel). They show the maximum and minimum probability to determine the neutrino mass hierarchy with the desired confidence level (3σ or 5σ) as a function of exposure. That probability depends on the value of CP angle (δ). As is seen from these figures, to reach the 3σ significance almost a ten years of measurement, corresponding to $1.5 \times 10^{21} p.o.t.$, would be required. Crucial for resolving the mass hierarchy is a proper determination of neutrino energy, which requires the event to be fully contained inside the detector. This limits the statistics, as Figure 6.5 shows.

6.3. LENA Simulation Framework

To study the detector response and potential of LENA for great variety of physics phenomena consistently, a Monte Carlo simulation framework has been developed in Technical University Munich [138]. The framework is based on the GEANT4 toolkit [150], widely used in particle physics.

The geometrical description of the detector follows simplified baseline design described at the beginning of this chapter. It consists of a cylindrical pure LAB target with height of 98m and diameter of 28 m. The target is surrounded with a 2 m thick buffer volume, made out of LAB as well, but the scintillation process is not simulated in this volume. The buffer volume is enclosed in the concrete tank with thickness of 30 cm. Outside the tank there is a 2 m water buffer and limestone rock.

The built-in physics list (QGSP_BERT_HP including G4MuonNuclearProcess and G4MuonMinusCaptureAtRest) of the GEANT4 framework is used to describe the hadronic and electromagnetic interactions. The built-in scintillation model of the

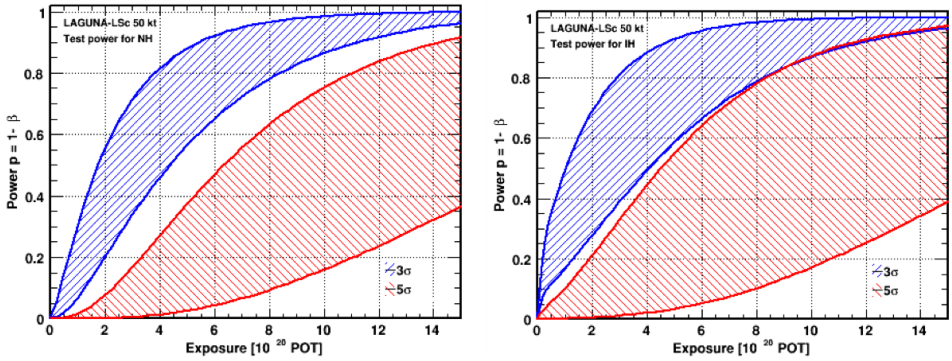

Figure 6.6.: The statistical power to resolve the neutrino mass hierarchy for normal hierarchy (left) and inverted hierarchy (right). Only fully contained events are included. This conservative approach assumes the signal efficiency is 27% (quasi-elastic charge current events) and the 11% of background events (mis-identified NC events) remaining.

GEANT4 framework (G4Scintillation) have been considered too simple for the description of the properties of LAB, hence the custom-made scintillation model have been implemented. It follows the scintillation model described in Chapter 5 and the scintillation properties of LAB introduced in Table 5.1. In addition the model includes absorption ($l_{\text{abs}} = 20$ m), absorption-reemission (isotropic scattering, ($l_{\text{iso}} = 60$m, decay constant $\tau_{re} = 1.2$ ns) and Rayleigh scattering processes ($l_{\text{ray}} = 40$m). These properties correspond the optical photon wavelength of 430 nm i.e. the wavelength dependence of the processes are not taken into account at this stage.

For an output from the Monte Carlo simulation the optical photons generated by the user-defined incident particle(s) and their secondaries are registered when they hit to the photosensitive detectors (PMTs). User have different options how to define the sensitive detectors. The options are described more in detail in [138]. In the studies in and closely related to this work the PMTs are implemented as following. The 30542 PMTs (12 inch) with light concentrator attached are used and they are placed at the edge of the buffer liquid. This resembles the baseline design of the optical module of LENA. The properties of the light concentrator follows the ones used in Borexino experiment. The detection efficiency depends on the incident angle of the photon hitting the light concentrator, being 86% when angle is below 40 degrees and dropping rapidly to zero if the incident angle is larger. The possible reflections from the light concentrator are not simulated. The more detailed description of the LENA simulation framework is in [138].

The output of the LENA GEANT4 environment is based on ROOT and in the energy and position reconstruction the implementation of photo detection related issues (e.g. energy resolution or dark counts) are implemented in the next step of the data-flow with a separate program developed by D. Hellgartner (TUM). After this step the simulated data look similar to the pre-processed data from the LENA experiment and are ready for different kinds of analyses.

The simulation framework has been used in several physics potential studies, including work presented in this thesis, most crucial being the energy and position reconstructions studies and the studies related to rejection of gamma-ray induced background.

Energy and Position Reconstruction Capability

Finding the location inside the detector where the event (the scintillation light emission) has occurred and the amount of photons emitted (i.e. the energy deposited) are the key tasks in the event reconstruction. In low-energy events, where the light-emission can be considered point-like and isotropic, the position and "energy" can be found by using a point-fitting algorithm. The position and energy resolution from point-fitting algorithm in baseline design of LENA is presented in detail in [129]. The main results are shown in Figure 6.7. The relative energy and position resolution in the fiducial volume of the detector can be approximated as:

$$\Delta T/T = (6.0 \pm 0.1)\ \% \cdot 1/\sqrt{T/\mathrm{MeV}}, \tag{6.1}$$

$$\sigma_{\mathrm{pos}} = (6.26 \pm 0.12\ \mathrm{cm}) \cdot 1/\sqrt{T/(\mathrm{MeV})}. \tag{6.2}$$

The functions represent the standard deviation of the gaussian resolution function. The T is the true kinetic energy of an electron, ΔT is the deviation of the reconstructed energy from the true kinetic energy, and σ_{pos} is the standard deviation of the position resolution function. The energy and position resolution as a function of the kinetic energy of the electron is shown in Figure 6.7. In context of this thesis the energy and position resolution play crucial roles in every physics analysis as they define the energy dependent smearing of the energy spectra and hence affect to the accuracy of the reconstructed energy and position of the event. This is important especially in the case of oscillometric measurement as the variations in the oscillation probability within the detector dimensions is studied. Furthermore, these reconstruction capabilities have an impact to the systematic uncertainty due to the normalisation of the total events collected (in fiducial volume) within a (part of the) detector.

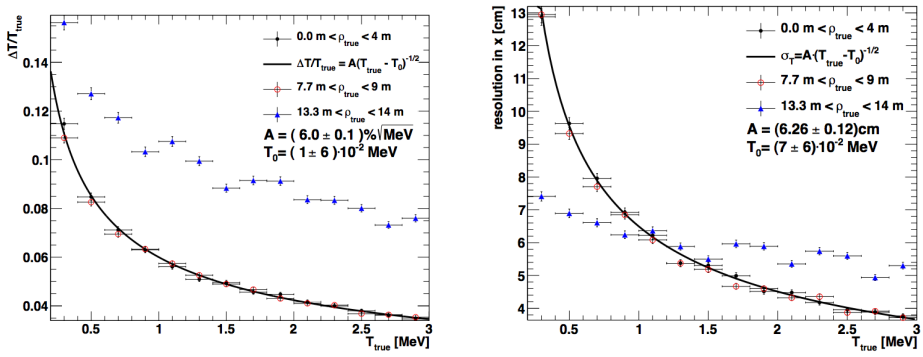

Figure 6.7.: The energy and position resolution as a function of kinetic energy of the electron obtained from the point-fitting algorithm [129].

External Gammas from Detector Materials

At the energies above few hundred keV the gamma-rays deposit their energy to the scintillator Compton scattering or pair production, having an electron or electron and positron in final state, respectively. The signal obtained is similar to that of the neutrino-electron scattering. From the signal point of view that makes the full rejection of gamma-induced background practically impossible. To suppress that background, the active volume should be shielded against the gamma-rays originating in the surrounding rock and from detector materials around the scintillator target. That reduce the number of gamma-rays entering to the active detector volume. The background can be further suppressed by defining the fiducial volume cut, i.e. selecting events whose reconstructed positions are sufficiently far away from the walls or the photomultipliers. This of course decreases the active volume but improves the quality of the data (signal to noise ratio). The gamma-ray background rejection has been studied in [138]. Figure 6.8 demonstrates the power of the fiducial cut. It shows that the level of gamma-ray induced background substantially decreases if the events with the reconstructed positions inside the detector radius of 12 m radius compared with the (full) 13.5 m radius are selected. The gamma-ray background would affect especially the solar neutrino measurement, but also the sterile neutrino search with radioactive ^{51}Cr source discussed in Chapter 9.

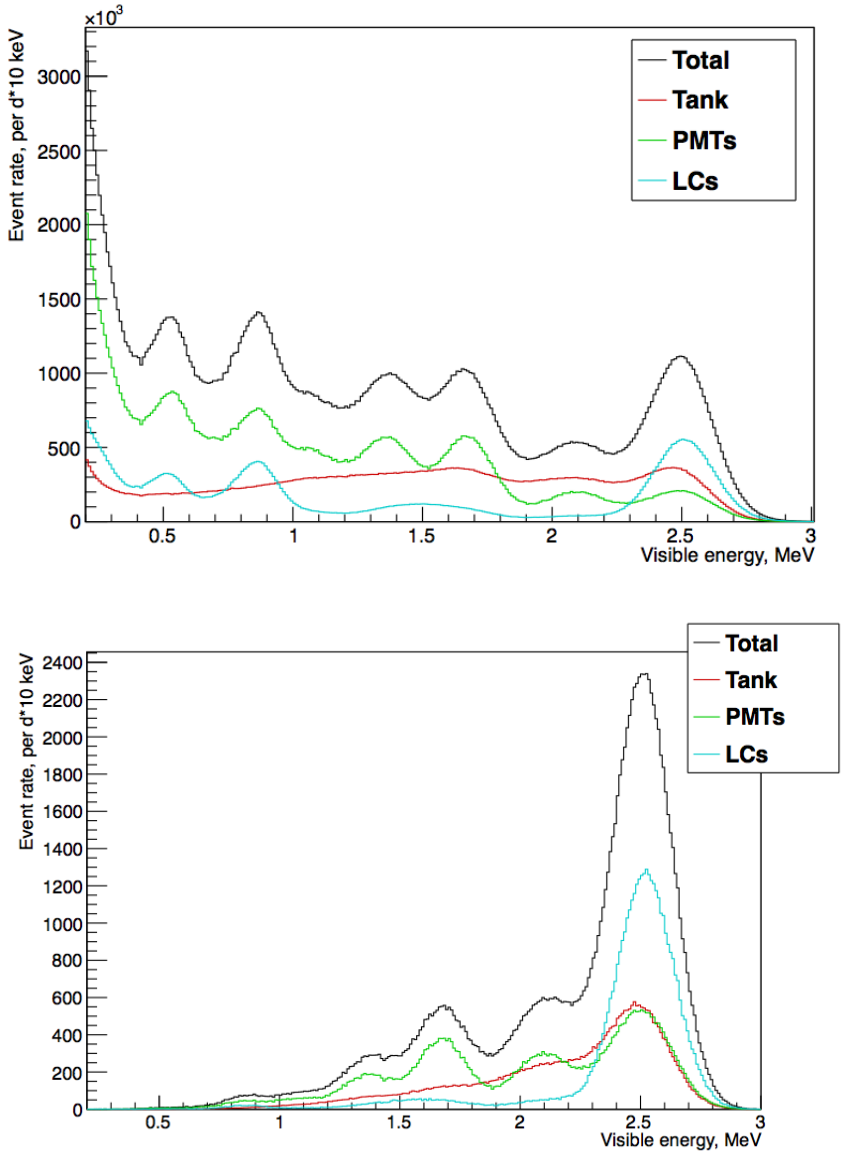

Figure 6.8.: Effect of fiducial volume cut on the external gamma-ray background from different external sources (concrete tank, photomultiplier tubes and light concentrators) [138]. In the upper panel the 13.5 m radius of the fiducial volume have been applied. The lower panel the radius of fiducial volume is reduced to 12 m. The reduction of external gamma-rays in visible energies below 1 MeV is effectively suppressed.

Part III.

Studies Related to LENA

7. Reactor Neutrino Background

Nuclear fission reactors have been playing a crucial role in neutrino physic ever since the experimental discovery of neutrino by Cowan and Reines at the Savannah River Nuclear Plant [13]. In the neutrino oscillation physics the reactors were used first in short baseline oscillation experiment with baseline less than 100 m. Between years 1980-1995 several such experiments were conducted: ILL-Grenoble [151], Gösgen [152], Rovno [153], Krasnoyarsk [154], Savannah River [155] and Bugey [156] [157]. All these experiments measured the flux of electron antineutrinos, which was found consistent with the expectations. In 1999 the CHOOZ experiment [158] in France with the baseline length extended to $\sim$ 1km was set up. Still no sign of oscillation was observed in the region $\Delta_{31} > 10^{-3}$ eV^2 (90% C.L). The CHOOZ data restricted the value of the mixing angle θ_{13} to $\sin^2 2\theta_{13} < 0.14$ (90% C.L) for $|\Delta m^2_{31}| \simeq 2.4 \times 10^{-3}$eV^2. Since 2002, the KamLAND experiment [121] in Mozumi mine in Japan, utilising an one kiloton liquid scintillation detector, have been detecting electron antineutrinos from several reactors surrounding it within an average distance of 180 km. The main goal of this experiment is to probe the same pair of oscillation parameters (θ_{12}, Δm^2_{21}) as in solar neutrino experiments but with electron antineutrinos. The experiment has reported a strong oscillation signal, which is in agreement with the data from solar neutrino (ν_e) experiments [159]. The latest contribution of the reactor experiments to the neutrino oscillation physics is the precision measurement of oscillation mixing angle θ_{13}. The three experiments using multiple scintillator detectors and multiple reactor cores at $\sim$ 1 km baseline have reported the deficit of the electron antineutrino event rate compared to the non-oscillation rates. The current results of these experiments (Daya Bay [160], Double Chooz [66] and RENO [65]) are shown in Table 7.1. The next step in the reactor neutrinos will be the hunt for the neutrino mass hierarchy with $\sim$20 kiloton scintillation detector (JUNO, RENO-50) as was discussed in Chapter 4.

The relevance of reactor neutrinos for the present study is due to their role as a background for the measurements of astrophysical neutrinos. One part of this thesis work consists of a study of the present and the future reactor neutrino background in Europe and in particular at the Pyhäsalmi mine. This study will be presented in following.

Experiment	$\sin^2 2\theta_{13}$
Daya Bay	0.084 ± 0.005
Reno	$0.101 \pm 0.008(\text{stat.}) \pm 0.010(\text{syst.})$
Double Chooz	$0.090^{+0.032}_{-0.029}$

Table 7.1.: The result from the three independent reactor neutrino experiments measuring the mixing angle θ_{13} (December 2015). [160] [65] [66] .

Isotope	E_f, MeV/fission
^{235}U	202.36 ± 0.26
^{238}U	205.99 ± 0.52
^{239}Pu	211.12 ± 0.34
^{241}Pu	214.26 ± 0.33

Table 7.2.: Energy released per fission from different isotopes in the reactor fuel [163].

7.1. Reactor neutrino flux calculation

7.1.1. Neutrino Production in Nuclear Fission Reactor

The processes governing neutrino emission in nuclear fission process are understood quite well. Neutrinos emerge from beta-decays of the fission products of the nuclear fuel. The majority of neutrinos is produced in fission chains of ^{235}U, ^{238}U, ^{239}Pu and ^{241}Pu resulting in an average electron antineutrino release of 5.5 per fission. In addition, another 1.2 neutrinos per fission come from the β-decay of ^{239}U $\rightarrow$ ^{239}Np $\rightarrow$ ^{239}Pu -chain and 0.03 neutrinos/fission originate from neutron capture in the accumulated fission fragments. On the average, the total electron antineutrino release per fission is thus ~ 6.7 [161] [162].

Neutrino flux depends directly on the thermal power of the reactor, i.e. the rate of fissions occurring. The energy released by one fission could be calculated when fraction of different fuel isotopes and their energy releases per fission of are known [162]. The average fission energies of isotopes are presented in Table 7.2. During the running period of a reactor, the composition of neutrino producing isotopes varies. With constant thermal power, the average energy released per fission increases and the number of fissions decreases, due to the burn-up of the fuel and accumulation of isotopes. This affects the neutrino production of the reactor. The total variation of fission energy is less than 2% during the fuel cycle, as is illustrated in Figure 7.1

There are several reactor types available and the isotopic composition of the nuclear

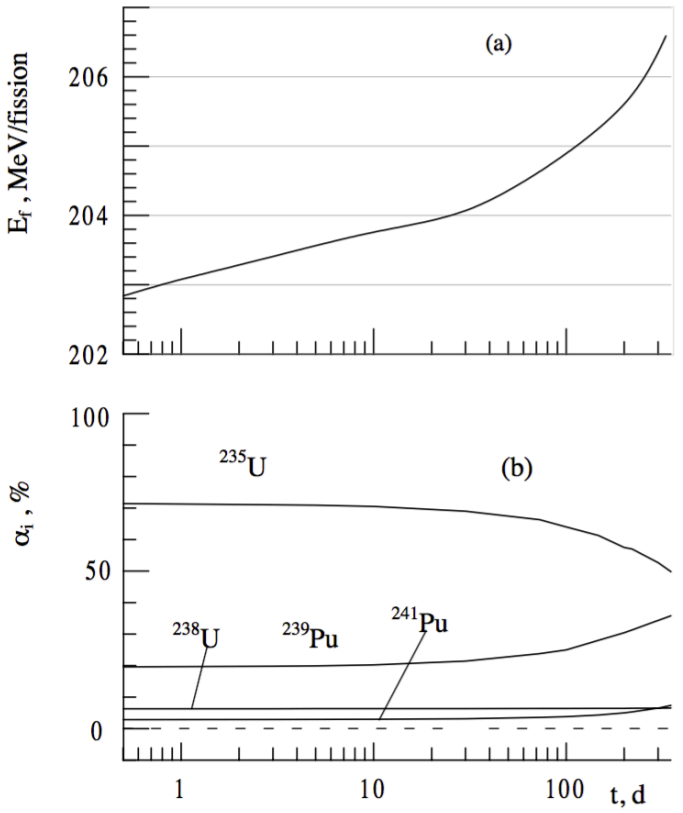

Figure 7.1.: Time evolution of total fission energy and fractions of fissile isotopes in PWR reactor. The total fission energy E_f (a) and fractions of fissile isotopes α_i (b) contributing to the total number of fissions of the Pressurised Water Reactor (PWR) with respect to the operation time t. [162]

Reactor Type	f_{U235}	f_{U238}	f_{Pu239}	f_{Pu241}
PWR	0.560	0.080	0.300	0.060
MOX	0.000,	0.081	0.708	0.212
PHWR	0.543	0.411	0.022	0.024

Table 7.3.: The fractions of the fissions for the neutrino producing isotopes in different reactor types [131] [165].

fuel used varies between the types. This affects also the energy released per fission and therefore to the neutrino production. Reactors can be divided into three main groups according to their nuclear fuel: 1) enriched Uranium burning (Pressurized Water Reactor (PWR), Boiling Water Reactor (BWR), light water graphite reactors (LWGR), gas cooled reactors (CGR)), 2) natural uranium burning (Pressurized Heavy Water Reactor (PHWR)) and 3) Mixed-OXide (MOX) fuel containing reactor (typically 30% of the fissions from MOX-fuel and the rest 70% from standard fuel) [164]. In the reactor-neutrino flux estimation it is sufficient to consider each reactor to be in the middle of their fuel cycle. A more precise estimate would require the measurements of the actual fluxes of reactors, not available for the present study. The fractions of fissile isotopes varies also with the type of the reactor. The fission fractions used in different experiments or their estimations are listed in [164]. In this work, the values taken from [131] and [165] have been used. The used isotopic contributions to the fissions are shown in Table 7.3.

Phenomenological Parameterization of the Energy Spectrum

The reactor neutrinos are produced in the β-decays of the fission fragments and their daughter nuclei. Their energy spectrum is the sum over the beta spectra of all the possible fission fragments appropriately weighted by their branching fractions. The reevaluation of the spectra have recently been carried out to include the nuclear data acquired since 1980's (see [166] for details). The phenomenological parameterization based on the re-evaluated reactor antineutrino spectrum follows exponential of a polynomial

$$S_{k,fit} = \exp\left(\sum_{p=1}^{6} \alpha_{kp} E_{\nu}^{p-1}\right) \tag{7.1}$$

with the coefficients α_{kp} for isotope k determined by a fit to the data. The values of the coefficients are listed in Table 7.4, and the resulting spectra of different fission fuel isotopes is illustrated in Figure 7.2.

Neutrinos are emitted isotropically from reactor core ($1/r^2$ dependence of flux). Due

k	α_{k1}	α_{k2}	α_{k3}	α_{k4}	α_{k5}	α_{k6}
^{235}U	3.217	-3.111	1.395	-3.690(-1)	4.445(-2)	-2.053(-3)
^{238}U	4.833(-1)	1.927(-1)	-1.283(-1)	-6.762(-3)	2.233(-3)	-1.536(-4)
^{239}Pu	6.413	-7.432	3.535	-8.820(-1)	1.025(-1)	-4.550(-3)
^{241}Pu	3.251	-3.204	1.428	-3.675(-1)	4.254(-2)	-1.896(3)

Table 7.4.: Coefficients for parameterisation of energy spectra of reactor neutrinos for isotope k [166].

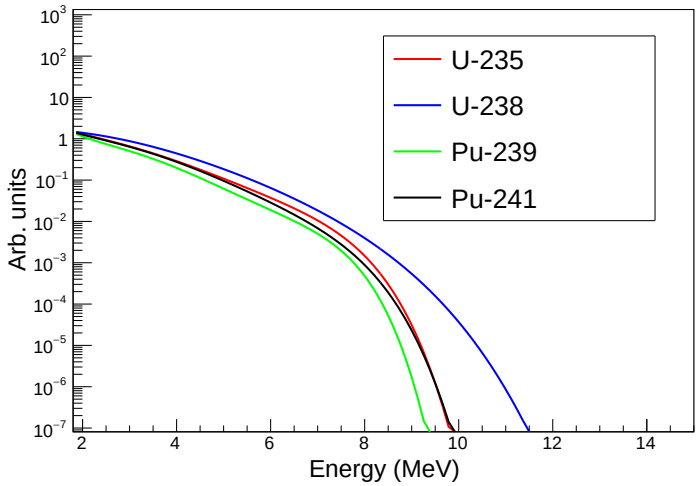

Figure 7.2.: Energy spectra of neutrinos from the fuel isotopes ^{235}U, ^{238}U, ^{239}Pu and ^{241}Pu. The spectra follow the parameterisation Equation 7.1 with the coefficients given in Table 7.4

to neutrino oscillation the probability to observe the neutrino as electron antineutrino changes along the way from the reactor to the detector. The strength of the neutrino flavor mixing is defined by oscillation parameters and is discussed more detailed in Chapter 4.

In the standard three-component oscillation case the survival probability of a produced electron antineutrino is given by

$$\begin{aligned} P_{\bar{\nu}_e \to \bar{\nu}_e} &= 1 - \cos^4(\theta_{13}) \sin^2(2\theta_{12}) \sin^2(1.267 \frac{\Delta m^2_{21} L}{E}) \\ &\quad - \sin^2(2\theta_{13}) \sin^2(1.267 \frac{\Delta m^2_{23} L}{E}) \end{aligned} \tag{7.2}$$

As it was discussed earlier, the matter of the Earth affects neutrino propagation and oscillation probabilities. However, for reactor neutrinos the matter effect can be generally neglected as the flight distances are relatively short and the effect is small compared with the other uncertainties of the experiments. However, compared to other sources of uncertainties this effect is considered to be negligible for reactor neutrinos. The illustration of matter effect to the typical reactor neutrino with energy of 4 MeV is depicted in Figure 7.3. With this particular energy the matter effect starts to impact at the distances greater than 100 kilometres and cannot be observed in short baseline experiments. When the reactor neutrinos are considered as a background, the measured energy spectra is a sum of neutrinos usually coming from several reactors at different distances. Taking into account the detector related uncertainties, like the energy and position resolutions, the matter effects, estimated to be sub-percent level, are smeared out.

7.1.2. Event Rate

The dominant detection channel of reactor neutrinos is the inverse beta decay. The total number of events from a reactor can be expressed in following form

$$N_{tot} = \epsilon N_p \tau \frac{\langle LF \rangle P_{th}}{4\pi L^2} \int dE_\nu \sum_k \frac{p_k}{Q_k} S_k(E_\nu) P_{\bar{\nu}_e \to \bar{\nu}_e}(E_\nu, L) \sigma(E_\nu). \tag{7.3}$$

Here the ϵ is the detector efficiency, N_p is number of free protons available in the target, P_{th} is the thermal power of the reactor and L is the distance from the reactor. The $\langle LF \rangle$ is the average load factor of the reactor. It describes the ratio between the net electric energy produced to the reference electric output during the time period τ. The load factors are assumed to be essentially same as the thermal load factors. In the integral the isotopic composition, related average fission energy and their spectra, p_k, Q_k and S_k respectively, as well as the energy dependent oscillation probability

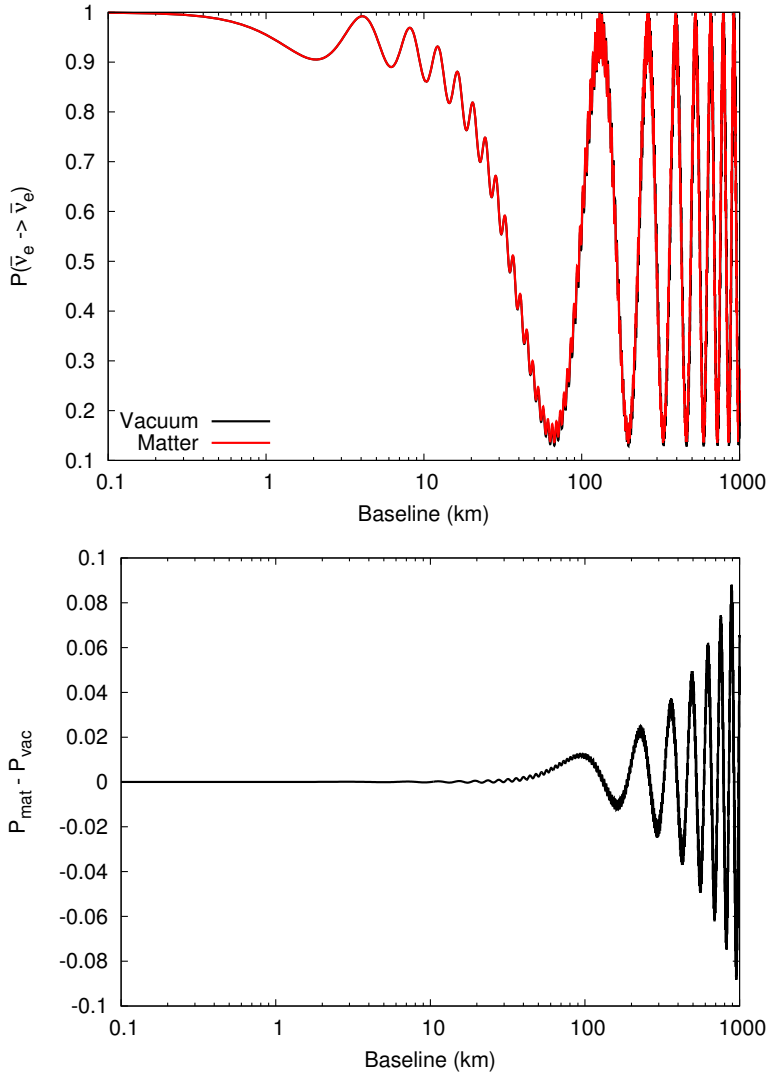

Figure 7.3.: Illustration of matter effects to the electron antineutrino with energy of 4 MeV. Upper panel: vacuum oscillation (black), matter oscillation red. Lower panel: the difference in percentage points ($P_{\mathrm{mat}} - P_{\mathrm{vac}}$).

Location	Events (TNU)	Events w/ 2014 load factors
Pyhäsalmi (FIN)	90.7 ± 3.1	72.4 ± 3.1
Umbria/Caso (ITA)	125.6 ± 4.2	100.1 ± 3.5
Sieroszowice (POL)	191.1 ± 9.4	154.5 ± 8.4
Slanic (ROM)	147.5 ± 6.1	123.9 ± 5.5
Canfranc (ESP)	290.2 ± 9.8	222.3 ± 8.4
Frejus (FRA)	738.3 ± 33.6	550.6 ± 19.5
Boulby (GBR)	1647 ± 144	1005 ± 119

Table 7.5.: Calculated reactor neutrino events in units of TNU in different underground locations proposed in the LAGUNA Design Study. The event rate with full power (Events) and the effect of load factors to the expected event rate (Events w/ 2014 load factors) is shown. The reactor data from year 2014 have been used.

P and interaction cross section of inverse beta decay σ are taken into account. The index k refers to the different neutrino producing isotopes (^{235}U, ^{238}U, ^{239}Pu and ^{241}Pu), see Table 7.4.

For making the comparison of different experiments at different locations of the world easier, the background event rates are usually expressed in the Terrestrial Neutrino Unit (TNU) defined as a rate induced by a neutrino flux that would generate 1 count per year in 10^{32} of protons (corresponding roughly to 1 kton of liquid scintillator). The same unit convention applies also for geoneutrinos (see Chapter 8).

7.1.3. Event rates at LAGUNA sites

The International Atomic Energy Agency (IAEA) lists the details of the operational nuclear reactors and their monthly and annual load factors (PRIS database). The European reactor sites and the underground sites studied in LAGUNA Design Study are shown in Figure 7.4.

By summing up the contributions coming from all reactors in the World, the map of reactor neutrino background, shown in Figure 7.5, can be constructed. The event rates at LAGUNA sites are listed in Table 7.5, and the shapes of the neutrino energy spectra for each sites are shown in Figure 7.6. For comparison, the rough estimate for JUNO experiment would be of the order of 1500 events per kiloton of liquid scintillator per year from reactors at the distance of 53 km and with full thermal power of 36 GW [2].

The estimation of uncertainties for the reactor neutrino flux is not straightforward.

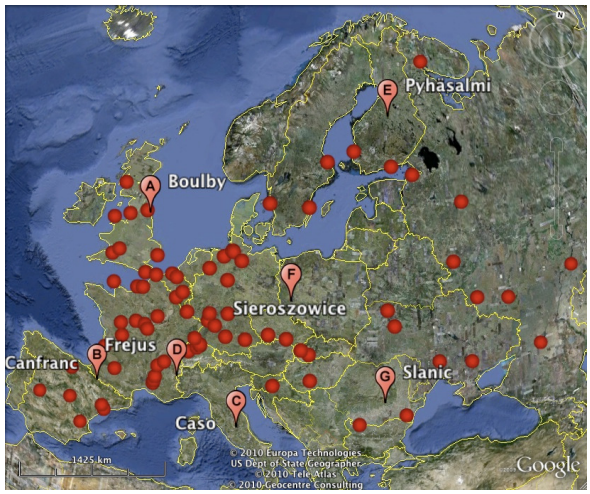

Figure 7.4.: Locations of the European nuclear power plants (red dots, may contain more than one reactor) and underground sites investigated within the LAGUNA-project.

There are error sources specific to each reactor core, like uncertainties in isotopic composition of the fuel or thermal power of the reactor. On the other hand, there are also global error sources, for example the uncertainties related to the neutrino oscillation parameters. The uncertainties are estimated using Monte Carlo method with the data statistics of 5000 one year measurements. The values presented in Table 7.5 are the mean and 1σ uncertainty from a gaussian fit to the Monte Carlo data. The systematic uncertainties considered (1σ) are listed in Table 7.6. The uncertainties are treated as gaussian, for simplicity.

7.2. Future Background Conditions at the Pyhäsalmi mine

From the LENA or other comparable detector to be build in the Pyhäsalmi mine point of view, it is useful to estimate the effect of future power plants to the neutrino background. The typical time scale for the construction of a nuclear power plant from the decision to the operational is usually order of ten years. Currently there are four power reactors operating in Finland and one, Olkiluoto-3 (or TVO-3) with 4.3 GW of thermal power or 1600 MW of electric power, is under construction at Olkiluoto nuclear power plant. The distance from Olkiluoto to Pyhäsalmi mine is 360 km. The duration from application for a decision-in-principle to the start of construction took

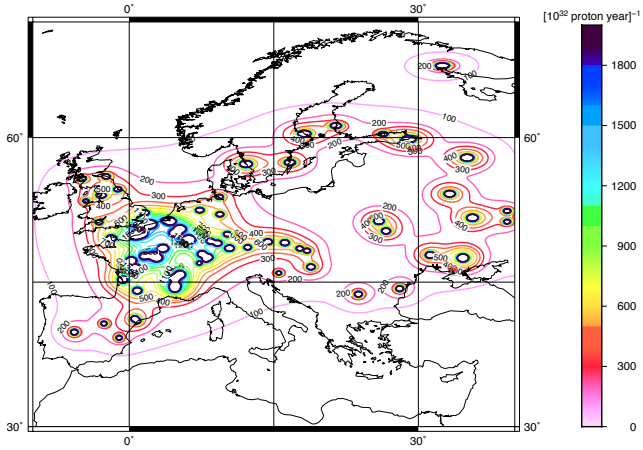

Figure 7.5.: Calculated reactor neutrino background across the Europe. The reactors are assumed to run with their nominal power and the load factors are not taken into account. The reactor data from year 2014 have been used.

Thermal power	P_{th}	2%
Fission energy	E_{U235}	0.13%
	E_{U238}	0.25%
	E_{Pu239}	0.16%
	E_{Pu241}	0.16%
Oscillation parameters	Δm^2_{21}	0.024
	Δm^2_{32}	2.4%
	$\sin^2 2\theta_{12}$	2.5%
	$\sin^2 2\theta_{23}$	2.0%
	$\sin^2 2\theta_{13}$	8.6%
IBD cross section	σ_{IBD}	1%

Table 7.6.: Uncertainties entering to the error estimation of reactor background event rate. For simplicity the systematics are considered to be uncorrelated and with gaussian shape.

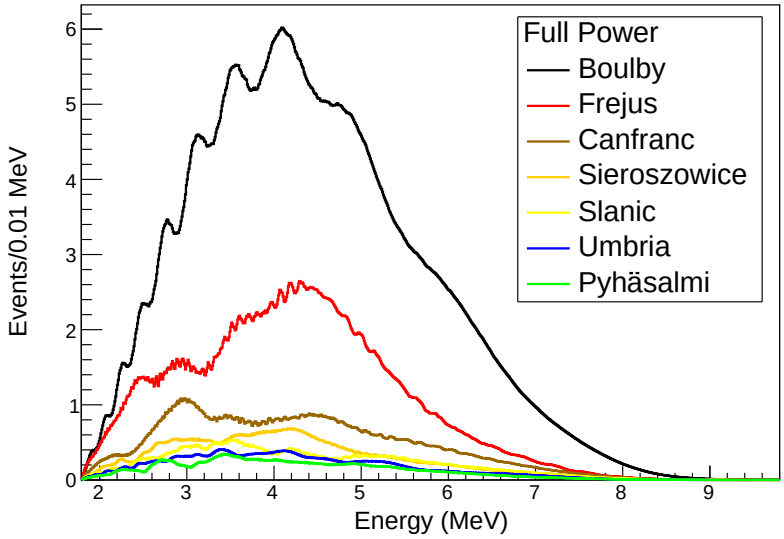

Figure 7.6.: Estimated reactor neutrino spectra at the sites considered in the LAGUNA Design Study. All the reactors in operation in 2014 are included.

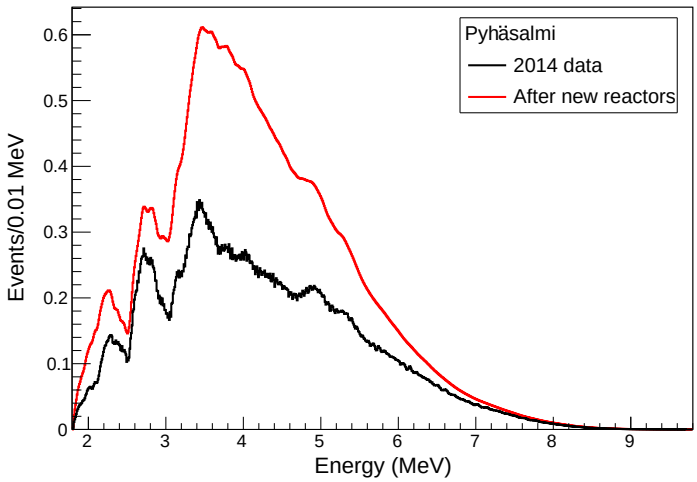

Figure 7.7.: Event spectrum of reactor neutrinos in Pyhäsalmi mine. Black curve denotes the situation in year 2014 (reactors running with their nominal power) and red line denotes the situation after the new reactors in Olkiluoto and Pyhäjoki nuclear power plants have been completed and are operational.

4.5 years, and the construction has been going on since July 2005. Current estimate the unit to be fully operational is during the year 2018. That reactor will increase the event rate of the reactor neutrino background approximately 10% at the Pyhäsalmi site.

A decision-in-principle for another nuclear reactor, to be built on Hanhikivi some 130 km from the Pyhäsalmi mine, was ratified by the Parliament in 2014. The company Fennovoima have submitted a construction license application in 2015 and the construction is planned to start in 2018 if the application will be accepted by the authorities. The pressurised water reactor (PWR) to be built will have the thermal power of 3.2 GW (1200 GW electrical). Fennovoima Electric company estimates that the reactor could be operational during the year 2024. The Pyhäjoki power plant would roughly double the reactor neutrino background flux at the Pyhäsalmi underground laboratory and increase the event rate to 144.0 ± 5.7 TNU. The comparison between the current background event spectrum (2014) and the situation after the Olkiluoto and Hanhikivi reactor have started their operation is shown in Figure 7.7.

Recently three reactor neutrino experiments Daya Bay, RENO and Double Chooz

have observed an excess of observed event rate from reactor neutrinos compared with the expected one around 5 MeV [167] [168] [66]. The origin of the that discrepancy is still unknown and it has not been taken into account in the reference flux spectra we have used. The total effect to the total event rate is estimated to be $\sim 2.5\%$.

The energies of geoneutrinos, supernova neutrinos (especially DSBN), possible experiments with radioactive sources, and the CP-violation search with Daeδalus-type experiment overlaps partially or fully with the energy range of the reactor neutrinos. Therefore the reactor neutrinos form a background for these measurements. In the case of DSNB and the Daeδalus, the lower limit of the energy window should be set so that reactor neutrinos are not entering the analysis window (for example $E_\nu > 15$ MeV). In the experiments with radioactive source, the activity (neutrino production) of the source should be high enough to guarantee sufficient high signal-to-background ratio. For the geoneutrino measurement the reactors induce the unavoidable background. The impact of current and future reactor background to the geoneutrino measurement will be considered in more details in next chapter.

8. Detection of Geoneutrinos

Geoneutrinos are created by β decaying isotopes inside the Earth. From the experimental point of view the most important isotopes are ^{238}U and ^{232}Th as the neutrinos they emit can have energy above the threshold for the inverse beta decay, which is the best process for detection. Due to its high mass abundance, the ^{40}K is also an important neutrino emitting isotope in the Earth. The mass abundance relative to uranium is estimated to be a(U):a(K) ≈1:12000 [169]. The energy of neutrinos originating from ^{40}K does not exceed the threshold of the inverse beta decay and are hence undetectable. The decay chains of ^{238}U and ^{232}Th and decays of ^{40}K produce varying numbers of electron antineutrinos (see Table 8.1).

Reaction	Q-value [MeV]
$^{238}\mathrm{U} \rightarrow ^{206}\mathrm{Pb} + 8\alpha + 8e^- + 6\bar{\nu}_e$	51.7
$^{232}\mathrm{Th} \rightarrow ^{208}\mathrm{Pb} + 6\alpha + 4e^- + 4\bar{\nu}_e$	42.7
$^{40}\mathrm{K} \rightarrow ^{40}\mathrm{Ca} + e^- + \bar{\nu}_e$	1.31

Table 8.1.: The three main isotopes in the Earth which produce electron antineutrinos via β-decays. For ^{238}U and ^{232}Th the whole decay chain is included.

As the neutrinos interact very weakly and hence travel undisturbed from the location of the decay to a detector, the observation of geoneutrinos opens a new window to the physical processes taking place inside the Earth. The estimated luminosity of the different components of geoneutrinos as a function of neutrino energy is shown in Figure 8.1. The Figure 8.1 also shows that there are plenty of other β-decaying isotopes in the Earth producing neutrinos which, however, are undetectable with current methods.

Some fraction of energy released in the decay process is carried away by neutrinos. The rest is transformed to heat inside the Earth. On average 47.7 MeV, 40.7 MeV and 0.59 MeV of energy is released in the decay chains of ^{238}U and ^{232}Th and decay of ^{40}K, respectively [169]. The energy production of these isotopes accounts for more than 99% of the radiogenic heat generated inside the Earth at present. The other components of the heat flux originate from the accretion phase and the core differentiation process of the Earth, as well as, cooling, seismic activity and friction. The total heat is thought to be the driving force of the plate tectonics and the

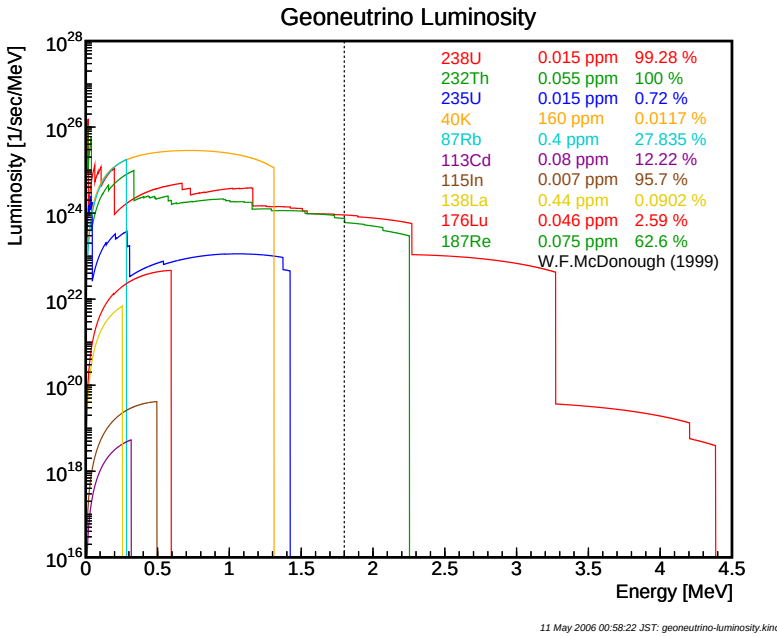

Figure 8.1.: Estimated geoneutrino luminosity of the Earth. The dotted line denotes the threshold energy of the inverse β-decay reaction, i.e, only contributions from the decays of ^{238}U and ^{232}Th are detectable.[1]

generation of the magnetic field of the Earth.

The density profile of the Earth has been studied by means of seismic measurements. This has led to the current understanding of the structure of the Earth. The general structure is depicted in Figure 8.2. The direct measurement of the isotopic composition and its variation between the crust and the mantle are derived from the rock samples of the crust and upper part of the mantle. These measurements cannot, however, be considered as a representative sample of the compositions of these reservoirs as, especially in the case of mantle, the direct rock samples are originating from the boundary layer between the crust and the mantle and the deep mantle samples are missing.

The models describing the composition of different layers of the Earth can be divided into three categories described by cosmochemical, geochemical and geodynamical models. They assume different initial composition of the primitive mantle (man-

[1]source: http://www.awa.tohoku.ac.jp/~sanshiro/research/geoneutrino/spectrum/ (12.1.2015)

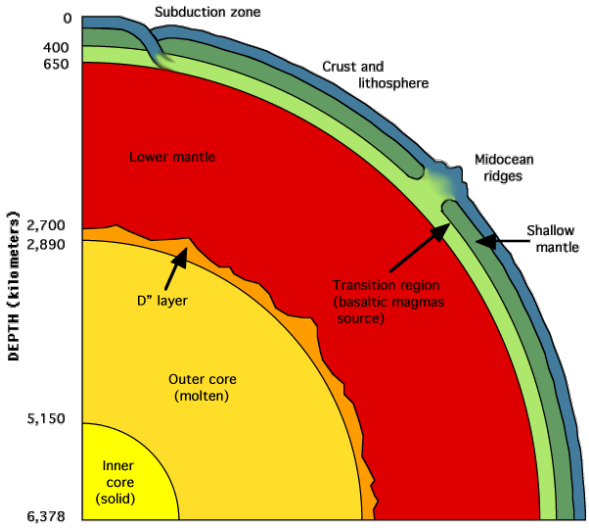

Figure 8.2.: The layers of the Earth.[2]

tle+crust just after the core differentiation) and lead to different dynamics (convection) governed by the total heat of the Earth and especially the radiogenic part of it.

One way to estimate the initial composition of Earth, as an input to the models is to study the composition of meteorites, i.e the early planetary medium of which also the Earth is created. In this simple approach, the bulk of the Earth consist of O, Fe, Si, Mg, Al, Ca and Ni, totalling to $\sim 98\%$ of the mass of the Earth. From these elements Al and Ca along with U and Th are refractory elements, i.e. have a high condensation temperature. They have been found to appear in equal proportions in different kinds of meteorites, while the proportions of other, non-refractory, elements vary. Therefore, by determining the abundances of U and Th inside the Earth, the amounts of other refractory elements can be calculated by using these so-called chondritic ratios. The abundances of other elements are model dependent.

By measuring the geoneutrinos fluxes it is possible to estimate the average contributions of uranium and thorium in the Earth. With measurements in several locations, their abundances in the mantle and in the crust can be accessed. Using these abundances, the radiogenic heat production can be calculated using the abundances and compared with the total heat production of the Earth (47 ± 2 TW in total) from the

[2]source: http://www.homepages.ucl.ac.uk/ ucfbdxa/resint.htm (18.1.2016)

drill-hole measurements [170]) allowing one to discriminate between different models.

8.1. Detection Method of Geoneutrinos

Geoneutrinos are detected via the inverse beta decay reaction on proton,

$$p + \bar{\nu}_e \rightarrow n + e^+, \tag{8.1}$$

the same process used for reactor neutrino detection. The Q-value of this reaction, ($Q = 1.804$ MeV) inhibits the observation of neutrinos from potassium whose endpoint energy is 1.31 MeV. Hence only geoneutrinos from the decay chains of ^{238}U and ^{232}Th could be efficiently detected by this method. The energy spectra of geoneutrino fluxes are shown in Figure 8.3.

The geoneutrino signal from inverse beta decay occupies the energy range from 1.8 to 4.5 MeV. The contribution of the events above the 3.25 MeV is negligible and usually overwhelmed by a reactor neutrino background. Hence, the experimental energy windows for geoneutrinos covers 1.8 - 3.3 MeV. This window is divided into two parts: the low-energy geoneutrino window containing neutrinos from both uranium and thorium decays (1.8 - 2.25 MeV) and the high-energy geoneutrino window containing neutrinos solely from uranium decays. In addition to the geoneutrino signals, there is always a background component from reactor neutrinos in these windows. In our analysis the energy range 3.3 - 8 MeV is used to estimate the reactor background entering to the both geoneutrino windows.

The total flux of geoneutrinos at the surface of the Earth is $\sim 10^6$ cm^{-2}s^{-1} which is relatively low compared with e.g. the flux of solar neutrinos (7×10^{10} cm^{-2}s^{-1}). Due to this low flux and small cross section of neutrinos with matter, the requirements for geoneutrino detectors are demanding. A clear delayed coincidence signature of the inverse beta decay reaction, the possibility to construct large detectors and the low threshold energy makes the liquid scintillator detectors the most feasible in the hunt for geoneutrinos. The major drawback of the scintillation detectors is their lack of directionality. The directionality would improve the resolving power between reactor neutrinos and geoneutrinos, as well as, help to deconvolute the mantle and crust components from the total geoneutrino flux.

As the shapes of the neutrino spectra from ^{238}U and ^{232}Th and the cross section of the inverse beta decay is well known, the simple relation between the flux of neutrinos ϕ and expected event rates S in terrestrial neutrino units (TNU) [169], defined as one event per 10^{32} target nuclei per year and corresponding roughly an annual event

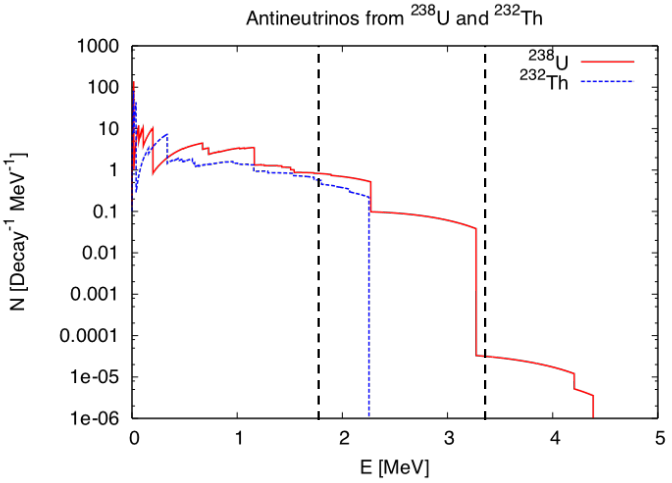

Figure 8.3.: The antineutrino spectrum of ^{238}U (red solid) and ^{232}Th (blue dotted). The detection window for geoneutrinos is between the black dashed lines (at 1.8-3.3 MeV). The lower limit is due to the IBD reaction threshold energy and above the upper limit the geoneutrino flux will be too low to be measured.

rate in one kiloton liquid scintillator detector, can be constructed:

$$S(^{238}\mathrm{U}) = 12.8 \times \phi(^{238}\mathrm{U}) \tag{8.2}$$

$$S(^{232}\mathrm{Th}) = 4.07 \times \phi(^{232}\mathrm{Th}). \tag{8.3}$$

Typically both of the geoneutrino fluxes from (^{238}U and ^{232}Th) are of the order of 4×10^6 cm^{-2}s^{-1} leading to event rate of few tens per kiloton of liquid scintillator in one year measurement on continental crust.

8.2. Experimental Status

The first detection of geoneutrinos was reported by the KamLAND experiment in 2005 [130]. By assuming the chondritic Th/U -mass ratio = 3.9, 4.5-54.2 events in the geoneutrino energy window were obtained with 90% C.L. Despite the large

uncertainty of the geoneutrino event rate, the data were sufficient to place the upper limit for the radiogenic heat production at 60 TW.

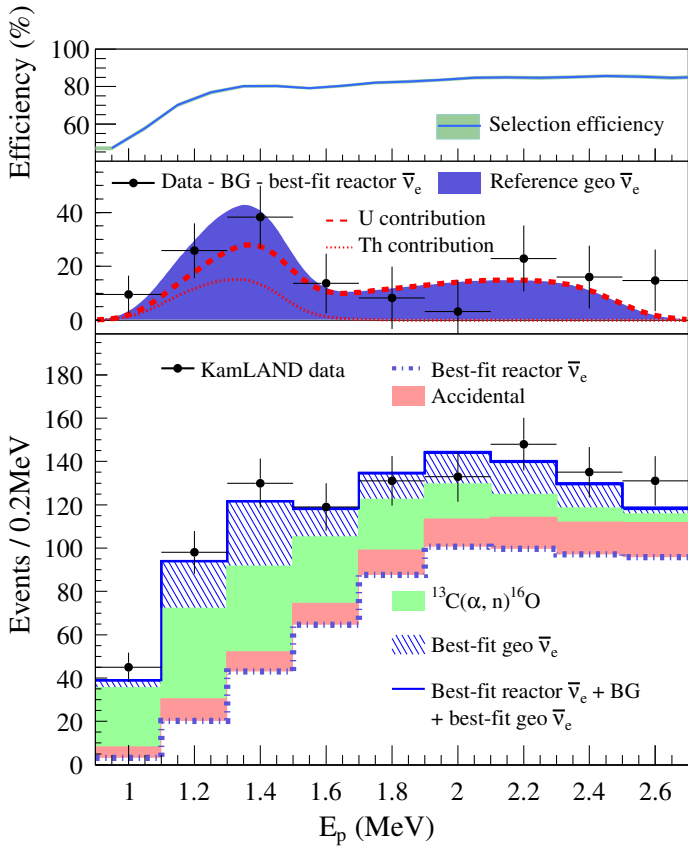

Figure 8.4.: Geoneutrino result of the KamLAND experiment [171]. The upmost graph depicts the estimated event selection efficiency. The graph in the middle shows the background subtracted event rates. The bottom graph shows the full measurement with fits for each component.

In 2013 the KamLAND collaboration reported the result based on 2991 days of data collection [171]. That period includes the time following the Fukushima disaster (March 2011) after which all the Japanese nuclear power reactors were turned off, meaning a substantially smaller reactor neutrino background than before. The result of 116^{+27}_{-28} geoneutrino events, corresponding to the $(3.4 \pm 0.8) \times 10^6$ cm^{-2}s^{-1} geo $\bar{\nu}_e$ flux, was obtained. Figures 8.4 and 8.5 illustrate the events in geoneutrino energy

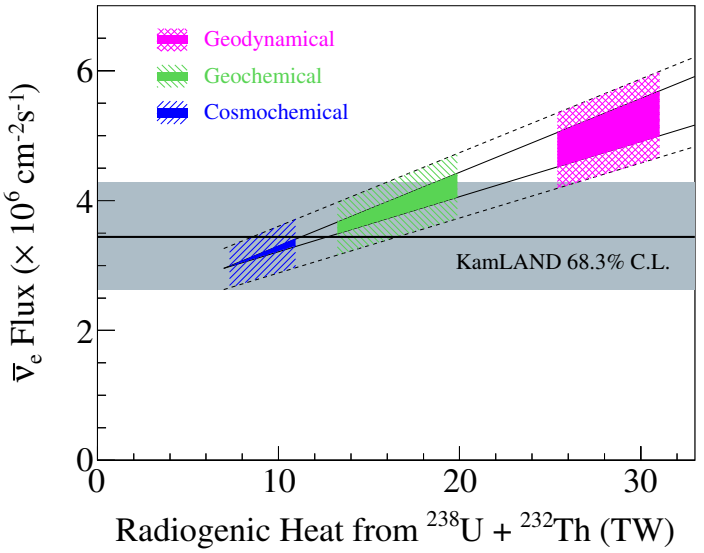

Figure 8.5.: Discrimination power of the KamLAND experiment to different categories of the models of the Earth's internal structure [171]. The 1σ uncertainty of the geoneutrino flux is denoted as shaded grey horizontal band. The different models describing the radiogenic composition of the Earth is denoted as shades areas.

window and the current discrimination power against different categories of geological models, respectively, of the KamLAND results. The results shown in Figure 8.5 seems to slightly favour the geochemical or cosmochemical models over the geodynamical one. The uncertainty of the flux measurement is, however, too large to make such exclusion.

The Borexino experiment, located in Laboratori Nazionali del Gran Sasso (LNGS) in Italy, has also observed the signal of geoneutrinos [131] and reports with the longer exposure time, although not exceeding the exposure of KamLAND experiment, are available (see refs. [165] and [172]). Its recent results of $23.7^{+6.5}_{-5.7}(\text{stat.})^{+0.9}_{-0.6}(\text{syst.})$ excludes the no-geoneutrino hypothesis with 5.9σ. The result limits the radiogenic heat production in the range of 23-36 TW. The measured prompt energy spectra of the geoneutrino measurement i.e. the energy deposited by the final state positron of the inverse β decay reactions is shown in Figure 8.6.

Figure 8.7 shows the geological model discrimination power of Borexino experiment.

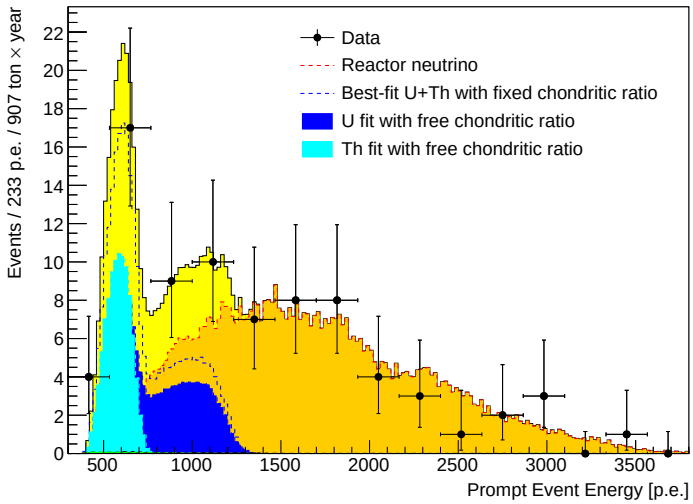

Figure 8.6.: Geoneutrino measurement of the Borexino experiment [172] showing the full measurement, fitted reactor (brown/orange) neutrino background and geoneutrino signal (yellow). The blue and cyan areas denote the geoneutrino signals from uranium and thorium when fitted free to the data.

In contrast to the KamLAND measurement shown in Figure 8.5, the Borexino measurement seems to favor geodynamical or geochemical model over the cosmochemical models. Similarly, as in the case of the KamLAND, one can not rule out any complete category of the geological models. This is due to the low statistics obtained in Borexino.

In the near future the SNO+ experiment in SNOLab in Canada starts its physics program containing also the geoneutrino flux measurement. The size of SNO+ is comparable with that of KamLAND. Hence the statistics will still be limited also from this experiment within coming years. The larger scintillator detectors (JUNO, RENO-50) proposed for the "near future" are dedicated to the measurement of the mass hierarchy of neutrinos by using neutrinos originating from nuclear reactors. The geoneutrino signal for the JUNO experiment have been studied in [2]. The annual event rate from reactors is estimated to be of the order of 5200 events, while the rate of geoneutrino events being 576. Figure 8.8 illustrates the expected reactor neutrino event spectrum compared with the geoneutrino event spectrum. The signal-to-noise ratio in the geoneutrino energy window (1.8-3.3 MeV) is expected to be as low as

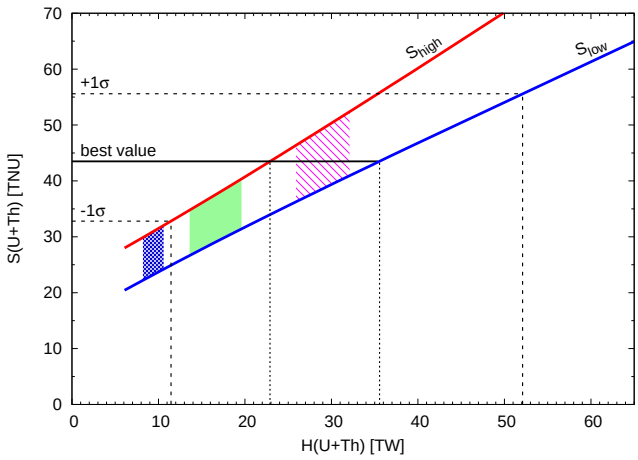

Figure 8.7.: Discrimination power of the Borexino experiment to different categories of the geological models of the Earth [172]. The uncertainty of the measured geoneutrino signal and corresponding uncertainty in radiogenic heat from ^{238}U and ^{232}Th is denoted as dashed and dotted lines, respectively. Different geological models are show as shaded blue, green and purple areas corresponding cosmochemical, geochemical and geodynamical models, respectively.

~ 0.11 which hampers the geoneutrino measurement.

8.3. Estimation of the Geoneutrino Flux in the Pyhäsalmi Mine

The estimated geoneutrino fluxes and event rates by three studies [169] for different underground laboratory sites are summarised in Table 8.2. The slight differences between the studies are due to the different assumptions concerning the isotopic abundance and the properties of the mantle (chemically homogenous or differentiated). The effect of the thickness of the crust in different locations is clearly manifested in the flux and rate values, the Hawaii site having the thinnest oceanic crust while the Pyhäsalmi located at the relatively thick Fennoscandian shield.

In a more recent study [174] ten potential experiment sites around the world were studied separately for U, Th and K components and for different reservoir areas

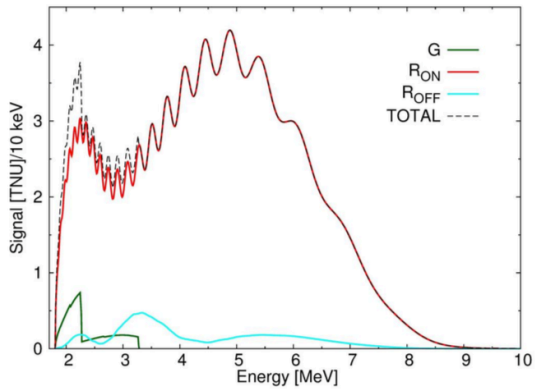

Figure 8.8.: Expected reactor neutrino event spectrum and geoneutrino event spectrum at the location of JUNO experiment in China [173]. The red and green lines are the expected geoneutrino and reactor neutrino signals, respectively, and the dashed grey line denotes the total signal. The cyan line illustrates the expected residual reactor neutrino signal if all the Chinese reactors within 55 km distance are turned off.

inside the Earth. The results for the Pyhäsalmi site are given in Table 8.3. The discrepancy between the earlier estimates arises from the more precise knowledge of the oscillation parameters affecting the survival probability of electron antineutrinos.

8.4. Prospects of Geoneutrino Measurements with LENA

Due to the construction of two new nuclear reactors in Finland, one in the Olkiluoto site and the other in Pyhäjoki, makes it necessary to re-estimate the reactor neutrino background in the Pyhäsalmi mine. This analysis is a part of this thesis work. In particular the background from the Pyhäjoki reactor, just 130 km away from Pyhäsalmi, would be crucial for the geoneutrino measurements.

The sensitivities of the geoneutrino measurements with LENA at Pyhäsalmi mine are estimated with the Monte Carlo method. The event sample corresponding to one measurement and the extraction of geoneutrino event rates are constructed in the following way. First to obtain the expected shapes of the energy spectrum of geoneutrino measurement, for both uranium and thorium chains, the initial neutrino spectra, shown in Figure 8.3, is used and, the cross-section of inverse β decay and the energy resolution of the detector are taken into account. The expected event

Location	U+Th rates in TNU according to		
	Mantovani *et al.*	Fogli et al.	Enomoto
Hawaii	12.5 ± 3.6	13.4 ± 2.2	13.4
Kamioka	34.8 ± 5.9	31.6 ± 2.5	36.5
Gran Sasso	40.5 ± 6.5	40.5 ± 2.9	43.1
Sudbury	49.6 ± 7.3	47.9 ± 3.2	50.4
Pyhäsalmi	52.4 ± 7.6	49.9 ± 3.4	52.4
Baksan	51.9 ± 7.6	50.7 ± 3.4	55.0

Table 8.2.: Predicted geoneutrino rates from U + Th at various locations. Rates are expressed in TNU. All calculations are normalized to the average survival probability $\langle Pee \rangle = 0.57$ [169].

rates are calculated based on the reference Earth model estimate (see Table 8.3). In one year LENA (with 50 kton fiducial volume) would detect ∼1700 geoneutrino events (∼1300 from uranium and ∼400 from thorium) within the geoneutrino energy window of 1.8-3.3 MeV. The calculation assumes that the background is solely based on nuclear reactors. The expected energy spectrum of reactor neutrino events is generated according to what have been presented in Chapter 7. The 80% load factor is assumed for each reactor and the statistical uncertainty of the observed event rate is taken into account. The all reactors in operation in 2014 have been included. The reactor neutrino background is ∼2800 events per years within 1.8-8 MeV energy window. The two new reactors (Olkiluoto and Pyhäjoki) would increase the number to ∼4800. However, the number of events falling into the geoneutrino energy window of 1.8-3.3 MeV are ∼780 (28%) with reactors in operation in 2014 and ∼1200 (25%) with the two new reactors, respectively. The effect of the excess of observed event rate in three reactor neutrino experiments Daya Bay [167], RENO [168]and Double Chooz [66], pointed out in previous Chapter, have not been taken into account in our calculation. In this study we are more interested on the effect of the new reactor nearby the Pyhäsalmi mine than the absolute sensitivity reach. Furthermore, as the excess is observed to be at the neutrino energies around 5-6 MeV and the total effect to the event rate is expected to be $\sim 2.5\%$, we will not expect it to drastically change the results we obtain.

To include the statistical fluctuations and the systematic uncertainties the event sample resembling data from single measurement, is generated by using the Monte Carlo method. The geoneutrino events are generated by sampling the expected energy spectra of the corresponding decay chain. For background originating in the nuclear reactors, the event rate induced by each reactor is separately calculated. The systematic uncertainties related to neutrino production and to the neutrino propagation, i.e. the neutrino oscillation parameters, are implemented (see Table 7.6).

	Flux in $m^{-2}s^{-1}$		
	ϕ(U)	ϕ(Th)	ϕ(K)
Litosphere	$4.0^{+1.00}_{-0.83}$	$3.64^{+1.02}_{-0.67}$	$15.53^{+3.33}_{-2.50}$
Deplepted mantle	0.57	0.35	3.93
Enriched mantle	0.45	0.42	1.74
Grand total	$4.98^{+1.00}_{-0.83}$	$4.41^{+1.02}_{-0.67}$	$21.04^{+3.33}_{-2.50}$
Expected TNU	35.1	9.9	–

Table 8.3.: The fluxes of different geoneutrino components (U, Th, K) from different reservoirs of the Earth (Litosphere, upper Deplepted mantle and lower Enriched mantle) as estimated for the location of the Pyhäsalmi mine [174]. The unit is $m^{-2}s^{-1}$. The calculation is based on the reference Earth model. Uncertainties given are 1σ values.

All the sources of systematic uncertainties are varied according to the gaussian shape. By adding the obtained geoneutrino events and obtained events from reactors, the event sample representing the measured data is constructed, called here as total event spectrum.

In our analysis, to obtain the number of geoneutrino events, the expected reactor neutrino background is subtracted from the total event spectrum. This kind of background subtraction method is selected for simplicity and because the main motivation is to study the effect of new reactors to be build nearby the mine. The expected shapes of the geoneutrino signal from both uranium and thorium chains are then fitted simultaneously to the background subtracted event spectrum. To evaluate effect of the uncertainties to the accuracy of the determination of total geoneutrino events, events from uranium chain, events from thorium chain and the extracted Th/U ratio, the Monte Carlo measurement is generated 2000 times.

The results presented in Figure 8.9 show that the total flux of geoneutrinos can be measured within ∼1% accuracy in a ten years measuring period. A measurement with this accuracy would provide an estimate to the radiogenic heat production as the chondritic Th/U-ratio can be assumed in the similar way as in the KamLAND and Borexino measurements. Due to the good statistics and the good energy resolution of the LENA detector, the uranium and thorium contributions can be separated. As shown in Figure 8.10 and Figure 8.11, the accuracy better than 3% and 5% in neutrino flux determination from the uranium chain and thorium chains, respectively, can be achieved in ten years.

Because of fully overlapping geoneutrino spectra of uranium and thorium the mea-

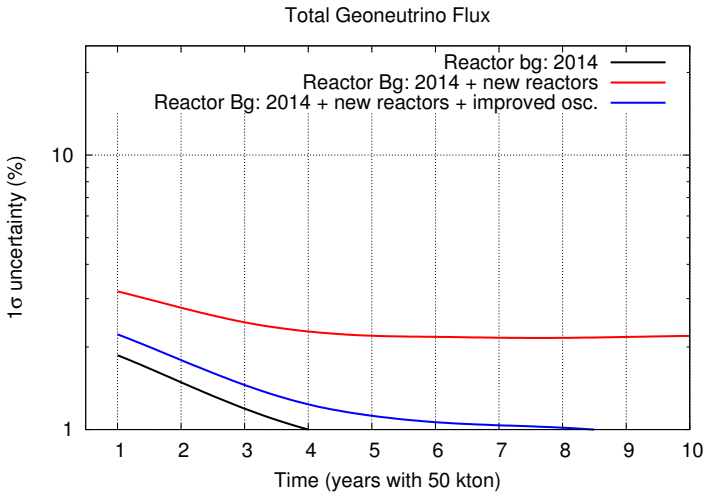

Figure 8.9.: The 1σ sensitivity of 50 kton liquid scintillator detector for the total geoneutrino flux measurement in the Pyhäsalmi mine

surements concerning these two isotopes are not independent. This worsens the accuracy of the Th/U -ratio measurement. On the basis of this analysis, the accuracy of $\sim 10\%$ could be reached (see Figure 8.12). Because the most of the geoneutrino flux in Pyhäsalmi is assumed to originate in the Earth's crust, the measurement performed there can be very useful for the restricting of the crustal Th/U-ratio.

In the analysis of the present study, presented result in Figures 8.9, 8.10, 8.11, 8.12, the effects of the new reactors at Olkiluoto (360 km) and possibly in Pyhäjoki (130 km) on the uncertainty of the sensitivity have been taken into account and is shown in the plots. The effect of the present uncertainties of the parameters of neutrino oscillations on the spectral shape and rate of the reactor neutrinos is quite drastic for the geoneutrino flux determination. Fortunately, the experiments currently under construction, e.g. the JUNO experiment will improve the accuracy of the oscillation parameters considerably in the near future. This improvement would almost fully compensate the effect of the increasing of the reactor neutrino background at the Pyhäsalmi site. Our results are comparable with the ones obtained with full fitting of the background components and presented in [1]

Finally, it is worth to point out that with a single geoneutrino measurement the deconvolution of the crust and mantle contributions of geoneutrinos is currently impossible. However, LENA at Pyhäsalmi would provide a valuable high statistics

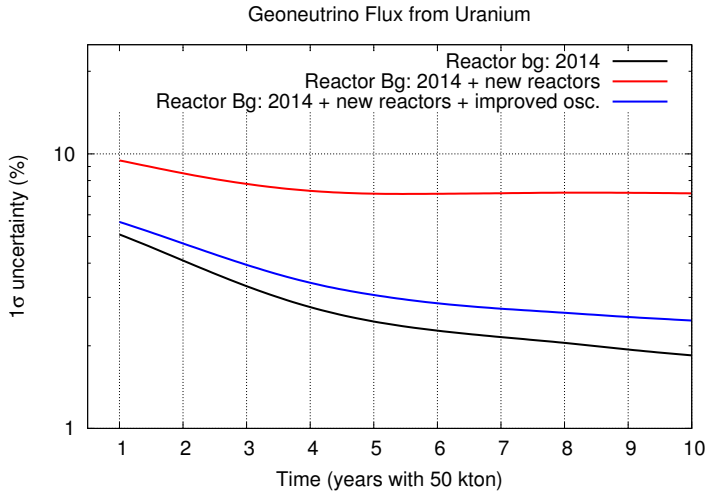

Figure 8.10.: The 1σ sensitivity of a 50 kton liquid scintillator detector for measurement of geoneutrinos from uranium chain in the Pyhäsalmi mine.

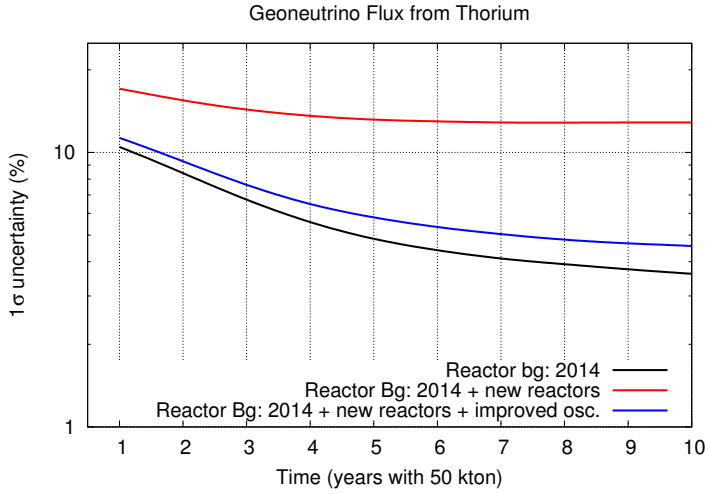

Figure 8.11.: The 1σ sensitivity of a 50 kton liquid scintillator detector for measurement of geoneutrinos from thorium chain in the Pyhäsalmi mine.

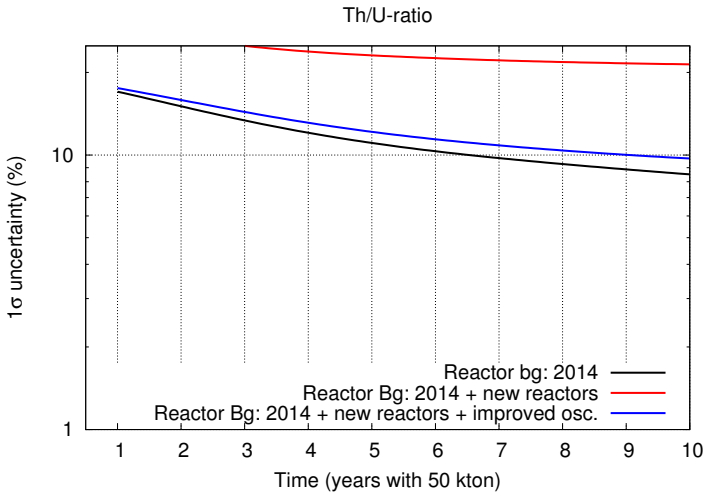

Figure 8.12.: The 1σ sensitivity of a 50 kton liquid scintillator detector for measurement of the Th/U -ratio the in Pyhäsalmi mine.

measurement at continental crust location. The results could be compared to those of KamLAND, Borexino and SNO+ which also are located at the crustal locations. The measurement of geoneutrinos at the location where the crust is thinner than in the present locations would be important to maximise the geoneutrino signal from the mantle. For this purpose the Hanohano Collaboration have proposed the order of 10 kiloton detector to be deployed in a locations at oceanic crust near the mid-oceanic ridge of Atlantic or Pacific ocean [175].

9. Detection of Sterile Neutrinos with LENA

The anomalies in experimental data with respect to the three neutrino flavor paradigm could be be explained by introducing sterile neutrino flavor(s). The next steps in search of them are the liquid scintillator experiment Borexino-SOX [120] and the short baseline beam program in Fermilab [51]. These issues have been discussed in Section 4.4.

Whatever the outcome of these experiments is, it is important to verify the sterile neutrino hypothesis applying the full discovery potential of next generation of the large liquid scintillator detectors. The additional mass and the physical size of these detectors would allow for a high statistics oscillometric measurement and determine the oscillation parameters governing the oscillation from electron type neutrino to sterile flavor. At the same time we would probe the conservation of CPT and CP symmetry by comparing the obtained oscillation parameters from the measurement with neutrino and antineutrino sources [176].

In this chapter the experimental scheme and the resulting sensitivities are presented in context of LENA. For comparison the sensitivities have been calculated also for a spherical detector with reconstruction capabilities comparable to JUNO. This would be a setup providing the best possible experimental sensitivity.

9.1. Experimental Scheme for LENA

The proposed long and mid-baseline oscillation experiments measure the oscillation curve at the near and far locations while in the oscillometric approach a significant part of the oscillation curve is sampled with a single detector. This approach is adequate thus only for oscillations with a short oscillation lengths, of the order of the physical dimensions of the detector, therefore suitable only for studying oscillations between active and sterile neutrinos. The method has been introduced in refs. [177] [178] [179] and [180].

In the short baseline approximation of the electron neutrinos the oscillation length and neutrino energy are linearly related (see Equation 4.12) and dependent on the mass squared difference Δm^2_{41}. Global fits indicate that the parameters governing the electron neutrino oscillation to sterile flavor are of the order of $\Delta m^2_{41} \approx 1$ eV^2 and $\sin^2 2\theta_{14} \approx 0.1$. (see Section 4.4). For example, an oscillation lengths of 1

and 10 meter correspond to ∼0.4 MeV and ∼4 MeV neutrino energy, respectively. Hence low neutrino energies and large detectors with sufficient position and energy reconstruction capabilities are required.

As the name indicates, LENA (Low Energy Neutrino Astronomy) has been designed for the optimum performance for non-men-made neutrinos at low energies. To take the full advantage of that feature LENA, must be located far away from the active power reactors. The main advantage of LENA for oscillomteric studies over existing detectors like Borexino is its size. Active length of 100 m will make LENA the quite an ideal detector for oscillometric measurements. For instance, the typical oscillation length in active-sterile neutrino oscillation of low electron neutrino ($\approx$ 1 MeV) is expected to be in the range from few centimetres to couple of meters. This allows the search for several oscillation lengths within the longitudinal dimension of LENA.

To maximize the sensitivity reach of the experiment for oscillometric measurement, the neutrino source should be located directly on the top of the active volume or even submerged into the scintillator. However, the latter "ultimate" scenario has many disadvantages: introduction of external impurities to the scintillator would weaken the performance, additional release of heat may change the properties of the scintillator and also increased gamma background nearby the source. Therefore, for practical reasons, the realistic location of the source in the case of LENA would be on the upper deck, shown on Figure 9.1, some 2-3 m above the top surface of the scintillator. The distance of 2 meters was assumed for all the oscillometry calculations presented in this thesis work for LENA.

For the neutrino sources two feasible candidates have been proposed namely ^{51}Cr producing electron neutrinos via electron capture reaction and ^{144}Ce–^{144}Pr mother-daughter combination generating electron antineutrino via β-decays. Usually the natural abundance of the desired isotope is not sufficiently high for the purpose but the enrichment or the artificial production of the source isotope is necessary.

^{51}Cr a the source of electron neutrinos

The simplified scheme of ^{51}Cr decay via electron capture into ^{51}V is depicted in Figure 9.2. In principle, the emitted neutrino has four possible energies, but as the two energy levels in both branches are so close in energy that those are indistinguishable in the experiment like LENA. Hence, two neutrino energies of $\sim$ 750 keV (90%) and ∼430 keV (10%) are considered.

A ^{51}Cr source can be produced by irradiating a sample of highly enriched ^{50}Cr in nuclear reactor with a high thermal neutron flux ($\approx 10^{15}\mathrm{cm}^{-2}\mathrm{s}^{-1}$). The weight and volume of produced ^{51}Cr source will depend on the desired isotopic enrichment level varying from 38% up to maximum 95%, totalling to 10-35 kg of weight. Therefore,

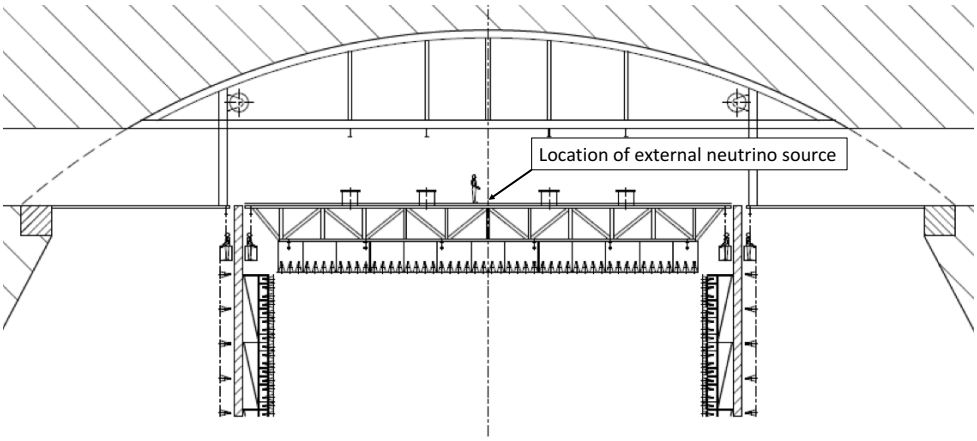

Figure 9.1.: The design of the top deck of LENA detector and assumed location of the external neutrino source.

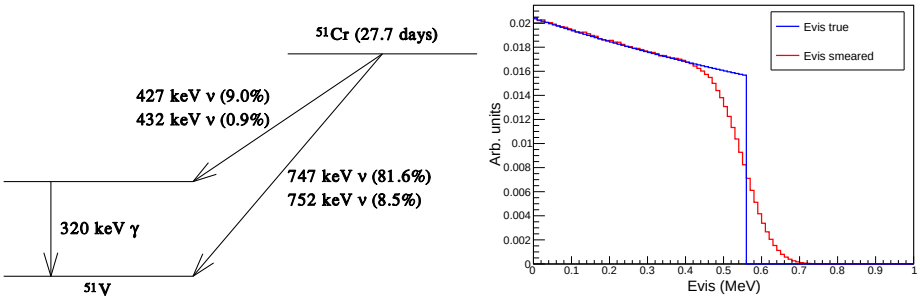

Figure 9.2.: Neutrino production of ^{51}Cr. Left: Decay scheme of ^{51}Cr. Right: Visible energy spectrum of recoil electron from 750 keV $\nu_e - e$ scattering

the source will have spatial dimensions of ∼15-23 cm which would be close to the position reconstruction resolution of the electron scattering events from 750 keV electron neutrinos in the LENA detector. This kind of electron neutrino source has been used in the calibrations of GALLEX [107] and SAGE [7] solar neutrino experiments, and is also proposed in the Borexino-SOX [120] in which the activity of 10 MCi could be reached. In this present work we assume conservatively the activity of the source to be 8 MCi.

^{144}Ce–^{144}Pr as the source of electron antineutrinos

For an electron antineutrino source we propose β-decaying isotope ^{144}Ce. The decay scheme of ^{144}Ce is shown in the left panel of Figure 9.3. The emitted antineutrino are detected via the inverse β decay reaction, and due to the 1.8 MeV threshold, the detectable electron antineutrinos are not created those in the decay of ^{144}Ce but they originate in from the subsequent beta decays of ^{144}Pr to ^{144}Nd. Figure 9.3 shows the shapes of the energy spectrum of neutrinos from the decay of ^{144}Pr. From that decay, roughly half of the neutrinos are detectable via inverse β decay. Furthermore, the energy resolution smears the observed energy spectrum of neutrinos. The shape of the energy spectrum of inverse β decay channel with and without the expected energy resolution of the LENA detector are also illustrated in the right panel of Figure 9.3.

A ^{144}Ce-^{144}Pr source can be prepared by a chemical extraction from exhausted nuclear fuel. Such a source has been proposed for the first phase of the Borexino-SOX experiment [120]. In the present work the initial activity of 0.12 MCi is assumed. The ^{144}Ce-^{144}Pr source needed, for measurement considered in this work, could be made of just few hundreds of grams of Ce and its size will be small enough to be treated as a point-like source reducing the uncertainty of the location of the neutrino emission.

9.1.1. Sources of Background

Concerning low-energy neutrinos from ^{51}Cr the major background is expected from the solar neutrinos. The visible energy spectra, i.e. the spectra of deposited energy by the final state electrons from neutrino electron scattering process, for different solar neutrino components are shown in Figure 9.4 . Especially those of ^{7}Be -neutrinos are fully overlapping with the visible energies observed from the ^{51}Cr source ($E_{\mathrm{vis}} < 560$ MeV). The count rate of ^{7}Be-neutrinos is approximately 300 $\frac{1}{\mathrm{day \cdot kton}}$.

Gamma-rays from radioactive impurities outside the target volume can also enter the scintillator volume and produce background signals. The dominant sources of background are the concrete tank, photomultiplier tubes and light concentrators.

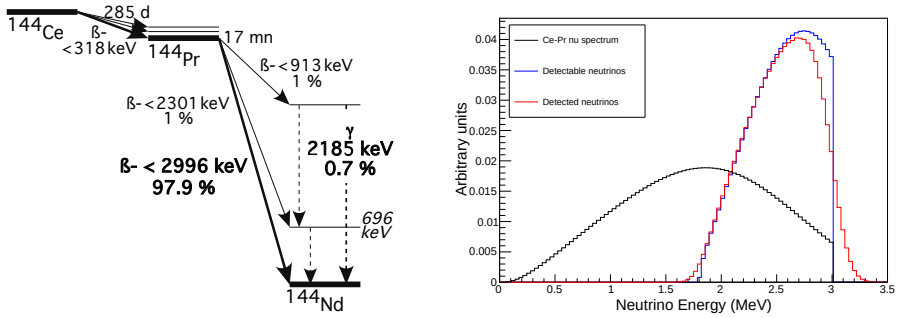

Figure 9.3.: Neutrino production of ^{144}Ce-^{144}Pr source. Left panel shows the decay scheme of ^{144}Ce to ^{144}Nd. The energy spectra of neutrinos from latter decay ^{144}Pr to ^{144}Nd (black) , the expected event spectra of neutrinos without (blue) and with (red) the energy smearing induced by the expected resolution of LENA are show in right panel. All curves are normalised to unity.

In order to reduce and reject this gamma background, a fiducial cut for the events entering the analysis is used. According to the gamma-ray background rejection described in Chapter 6, applying a fiducial cut of 1 m from the PMT support, the gamma-ray background with the relevant energy range ($<$ 560 keV) can be neglected.

The cosmogenic radioactive isotopes that are produced inside the target volume by muon-induced spallation reactions on the carbon nuclei can also raise the level of background. As the majority of these radioisotopes have a lifetime $\sim$ 1 s or shorter, they can be easily tagged by looking for a delayed coincidence with a cosmic muon, without introducing a large dead time to the measurement. Remaining cosmogenic radioisotopes are ^{11}C (β^+, τ = 29.4 min), ^{10}C (β^+, τ = 27.8 min) and ^{11}Be (β^-, τ = 19.9 min). The rates of cosmogenic isotopes in LENA have been studied in [138]. Only ^{11}C has the visible energy spectrum overlapping the one of ^{51}Cr. Furthermore, the count rate is only order of 10 counts per day in the analysis window (250-560 keV). Hence cosmogenic background will be neglected in this analysis.

Besides cosmogenic radioisotopes, there is also an intrinsic background from radioactive impurities in the scintillator material itself. The level of radiopurity in LENA depends on many factors and is hard to estimate in detail. Hence, in the following it is assumed that the levels of radiopurity similar to Borexino are reached. In context of sterile neutrino search this background can be considered negligible. The main background is caused by the ^{210}Po emitting alpha particle with energy of 5.3 MeV. Due to the quenching effect the visible energy of about 0.36 MeV. This overlaps the visible energy spectrum originating from ^{51}Cr. The expected level of ^{210}Po (τ = 199.6

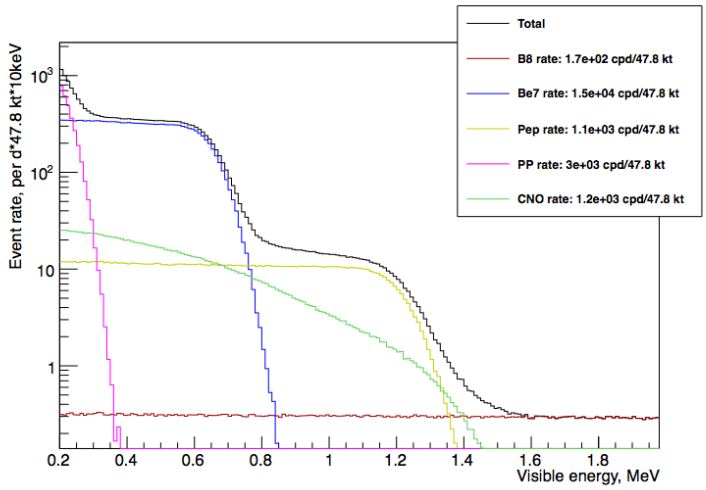

Figure 9.4.: Expected visible energy spectrum of solar neutrinos above 0.200 MeV in LENA. The rates are in counts per day. [138]

days) totals to approximately 90 counts per day per kiloton and can be further rejected by pulse shape discrimination to few counts per day per kiloton. When the signal level is of the order of few tens per day per kiloton on average.

The possible background sources in the ^{144}Ce-^{144}Pr measurement are antineutrinos from nuclear reactors and geoneutrinos from the Earth. As calculated in Chapter 7 and Chapter 8 using the event rates in Pyhäsalmi from reactors and geoneutrinos within their full energy range total to ∼90 and ∼50 events, respectively, per 10^{32} free protons per year. Applying the energy cut of 1.8-3 MeV taken from the energy range of neutrinos from ^{144}Ce-^{144}Pr the remaining background from reactors and geoneutrinos are at the per mille level compared to that of proposed the source (activity ∼0.12 MCi). Hence, in this analysis the measurement with ^{144}Ce-^{144}Pr is considered background free.

9.2. Simulations and Analysis

The sensitivity reach of the oscillation parameters from the two sources described above has been studied using the Monte Carlo method. The source is located at the centre of the top deck of the LENA and the distance to the scintillator is

approximately 2 m. The isotropically emitted events from the source and the evenly distributed background signals are generated within the detector volume.

For the ^{51}Cr experiment we assume to achieve 1% uncertainty in the measurement of the source activity. In the GALLEX experiment in 1995 the uncertainty in the source activity was estimated to be 2%, but in the Borexino-SOX 1% level is estimated to be reached [120]. The error in the fiducial volume is due to the energy and position reconstruction of the events and is approximately 1%. In simulations the true events are distributed over the whole detector volume and energy and position uncertainty is added. The fiducial volume cut is applied introducing the uncertainty to the normalisation of the signal. In this analysis the energy and position resolutions described in Chapter 6 are used. For the ^{144}Ce-^{144}Pr measurement the 1.5% accuracy of source intensity is assumed. The events entering the analysis must pass the following selection cuts:

- In the ^{51}Cr analysis the 1 m fiducial volume cut from the walls is applied to reject external gamma-ray background. The events in the energy window of 0.400 - 0.560 MeV were selected to guarantee the sufficient accuracy of the reconstructed position.
- In the ^{144}Ce-^{144}Pr analysis the 1 m fiducial volume cut from the walls is applied and the full energy window of 1.8 - 3.0 MeV is used.

For the both sources two exposure scenarios were evaluated. In the ^{51}Cr analysis the exposure of 55 days (∼two half-lifes) was selected for one irradiation-measurement cycle. The results for 1×55 days and 3×55 days exposures are presented. An example of the measurement with ^{51}Cr source is shown in Figure 9.5. The imprint of the survival probability P_{ee} on the spatial distribution of the detected events is clearly visible and provides a hints for appropriate values of θ_{14} and Δm^2_{41}. In the ^{144}Ce-^{144}Pr analysis the selected exposure cycle was 300 days and the result of 1×300 days and 3×300 days are presented. As the energy of the interacting antineutrinos can be reconstructed, the measured spectrum with respect to the L/E ratio can be obtained. This is shown in Figure 9.6. The neutrino production rates and the data of simulated events and impact of fiducial cuts are summarised in Table 9.1.

9.3. Results

9.3.1. Simple Event Rate Analysis

The most robust data analysis is to study solely the total event rate. This approach does not reveal anything about the value of the Δm^2_{41} but shows the possible deficit of the number of observed events. This is related to mixing ($\sin^2 2\theta_{14}$) i.e. the

	^{51}Cr	^{144}Ce-^{144}Pr
Neutrino flavor	ν_e	$\bar{\nu}_e$
Neutrino energy	mono-energetic; E=750 keV	continuous; E<3 MeV
Exposure	55 days	300 days
Neutrinos produced	6.9×10^{23}	8.2×10^{22}
Total events from source	7.82×10^{5}	1.39×10^{5}
Events passing cuts	1.36×10^{5}	9.3×10^{4}
Background events	5.7×10^{4}	60

Table 9.1.: The event rates of neutrinos and antineutrinos from a ^{51}Cr and ^{144}Ce-^{144}Pr source, respectively, for given exposure times.

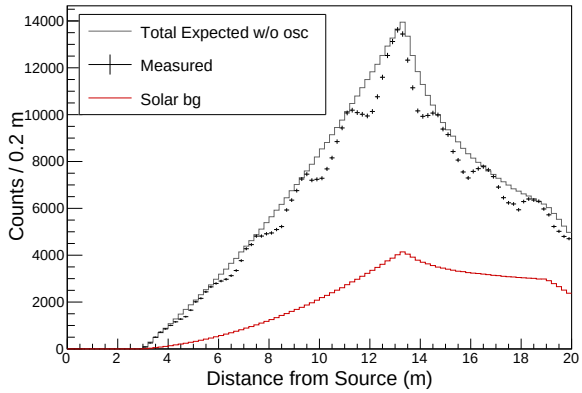

Figure 9.5.: The spatial distribution of events in a 3×55 day measurement with a 8 MCi ^{51}Cr source. The black dots denote the total events collected, the black continuous line events without additional sterile neutrino flavors and red line the solar background events.

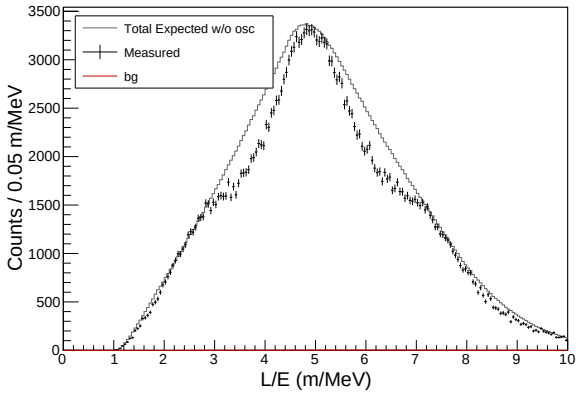

Figure 9.6.: The event rate from a ^{144}Ce-^{144}Pr source with respect to L/E ratio, where L and E are the reconstructed position of interaction and reconstructed energy of the neutrino, respectively. Black dots denote the measured rates and black continuous line the rate without additional sterile neutrino flavors.

oscillation amplitude. The result of this approach is shown in Figure 9.7, where the red area denotes the variation of the expected count rates without oscillation and the blue area the measured rates. With the ^{51}Cr source the bound of $\sin^2 2\theta_{14} > 0.1$ is reached with 5σ C.L. within one 55 day exposure cycle. For a ^{144}Ce-^{144}Pr-source the accuracy is slightly worse due to larger a uncertainty of neutrino production rate and lower statistics.

9.3.2. Spectral analysis

As shown in Figure 9.5 and Figure 9.6, information of the oscillation parameters is in the spatial distribution (^{5}1Cr), and spatial and energy distributions (^{144}Ce-^{144}Pr) of events. In this analysis the expected background spectrum, shown also in Figure 9.5 and Figure 9.6, is first subtracted from the observed measurement and then obtained signal spectrum is divided with the expected spectrum without oscillation. The results are shown in Figure 9.8 and Figure 9.9 where the oscillatory behaviour of the probability function is clearly visible. When the oscillation probability function is fitted to these observations, one can extract the value of Δm^2_{14}. The amplitude of the observation/expected -ratio which resembles the amplitude of probability function smeared with the position and energy resolution of the detector, provides only a lower limit for the amplitude.

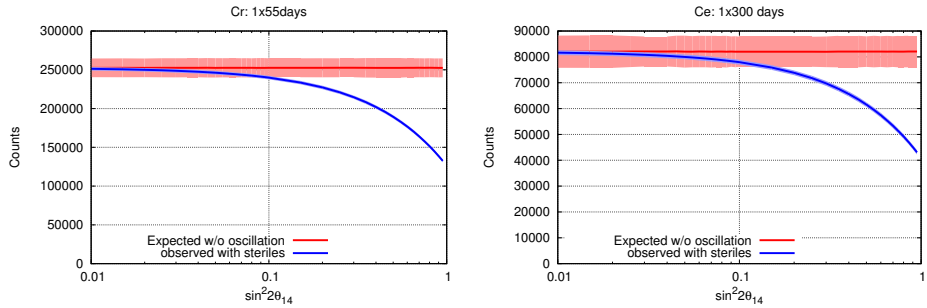

Figure 9.7.: Result of the event rate analysis. Based on measured event rates the deficit of the neutrino events becomes visible (5σ C.L.) with $\sin^2 2\theta$ values greater than 0.1. This is illustrated in rates measured with ^{51}Cr source (1x55 days, left) and with ^{144}Ce–^{144}Pr (1x300 days, right).

To obtain the final sensitivities, both parameters ($\sin^2 2\theta_{14}$ and Δm^2_{41}) are extracted by smearing the original probability function and fitting it to the observed ratio. The minimization is done with the ROOT-Minuit2 minimizer [181]. The Monte Carlo measurement is generated 2000 times for each parameter pair which guarantees a sufficient variation for the extracted results. The results are shown in Figure 9.10 and Figure 9.11.

In the most interesting region of $\sim 1\text{eV}^2$ and $\sin^2 2\theta_{14} \sim 0.1$ with the ^{51}Cr source the measurement of Δm^2_{41} with better than 3 (2) % (5σ C.L.) is possible with 1x55 days (3x55 days) exposure. With ^{144}Ce–^{144}Pr source the measurement better than 5 (3) % (5σ C.L.) with 300 (3x300) days seems feasible. For both sources the accuracy of the oscillation amplitude determination is considerably worse ($\sim 10\%$), mainly due to the normalisation (activity of the source).

Especially in the ^{51}Cr measurement, lower values of Δm^2_{14} lead to a lower oscillation frequency and hence an increased "horizontal" uncertainty when fitting the frequency part. On the other hand, at larger values of Δm^2_{14}, the position resolution of the detector starts to affect the accuracy and the smearing of the oscillations begin to play a crucial role and hampers the extraction of Δm^2_{14}. Similarly in the case of ^{144}Ce-^{144}Pr source a higher neutrino energy leads to a relatively slow change of the probability function for low values of Δm^2_{14}. This decreases the sensitivity. At the higher values Δm^2_{14} the changes in the L/E ratio become faster, but the poorer statistics per bin begin to worsen the sensitivity reach.

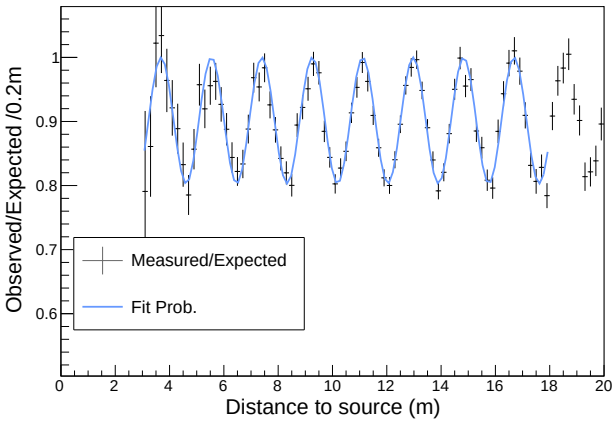

Figure 9.8.: Measured spatial distribution of events divided by the expected one without oscillation for the measurement with ^{51}Cr. Fitted probability function is shown in light-blue.

9.3.3. Sensitivity reach with Spherical Detector

For comparison, a similar analysis has been conducted for a 20 kton spherical detector with a source at the centre of the sphere. In this scenario the design values of JUNO [2] for energy and position resolutions of 3% for energy (at 1 MeV) and 5 cm (at 1 MeV), respectively, have been used. With the current knowledge this presents the best achievable performance for a large liquid scintillator detector.

The background conditions are assumed to be similar as in the case of LENA, except for the reactor neutrino background. The reactor neutrino background is assumed to follow the level and shape estimated for JUNO (see Figure 8.8). The fiducial volume cut have been applied so that the events with reconstructed radius less than 2 m from the source and with radius greater than 15 m are rejected.

The higher statistics and better energy and position resolution of the spherical detector than in the case of LENA lead to the extraction of Δm^2_{14} with better than 1% accuracy with 5σ C.L. by using ^{51}Cr source and better than 3% with ^{144}Cr-^{144}Pr source. The extraction of $\sin^2 2\theta_{14}$ remains rather poor due to the uncertainty of the source activity (absolute normalisation of the neutrino production). The sensitivity reach of Δm^2_{14} for a single exposure cycles for both of the sources (^{51}Cr and ^{144}Cr-^{144}Pr) are shown in Figure 9.12.

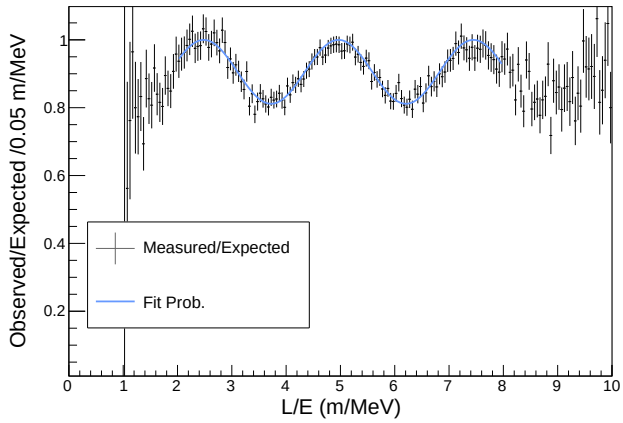

Figure 9.9.: Observed L/E distribution divided by the expectation without active-sterile oscillation for the measurement with ^{144}Ce-^{144}Pr. The fitted probability function is shown in light-blue.

We can summarise and conclude the results of the two scenarios presented above as follows:

- Using LENA and a ^{51}Cr source the sensitivity better than 2% can be expected for the determination of Δm^2_{41}. This covers the most interesting region for the reactor neutrino anomaly around $\Delta m^2_{41} \approx 1$ eV^2. In the case of ^{144}Ce-^{144}Pr source the sensitivity is better than 5% (5σ). By conducting more irradiation–measurement -cycles the measurement with $\sim$1% accuracy can be reached.
- With a spherical JUNO-like detector the sensitivity of a few per mille in the determination of Δm^2_{41} can be reached with ^{51}Cr source and with the ^{144}Ce-^{144}Pr the accuracy of $\sim$1% is expected.
- The accuracy of the determination of the oscillation amplitude depends on the normalisation of the signal and is considerably poorer compared with the accuracy of the determination of the Δm^2_{41}.

If we observe a difference in Δm^2_{41} governing the active-sterile neutrino oscillations associated with electron neutrinos and electron antineutrinos, it would be a certain sign of CPT and CP violation. However, the reverse would not be true. From the lack of the difference in Δm^2_{41}, one can not deduce non-existence of the CPT violation, as it can be manifested in several different ways.

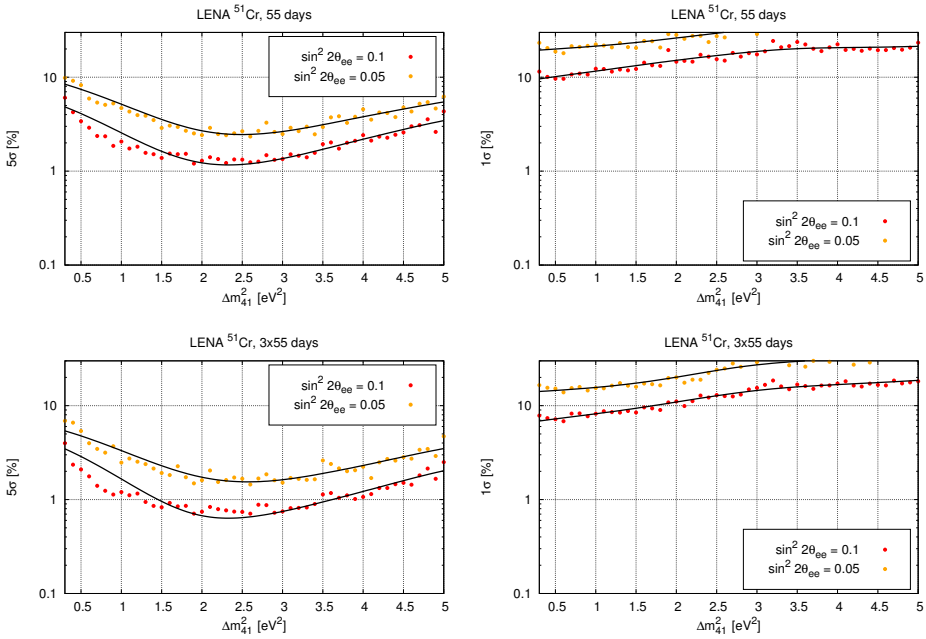

Figure 9.10.: Sensitivity reaches for Δm^2_{14} (left) and $\sin^2 2\theta_{14}$ (right) in the case of a ^{51}Cr source with exposures of 1×55 days (top) and 3×55 days (bottom). The black curves are only to guide the eye.

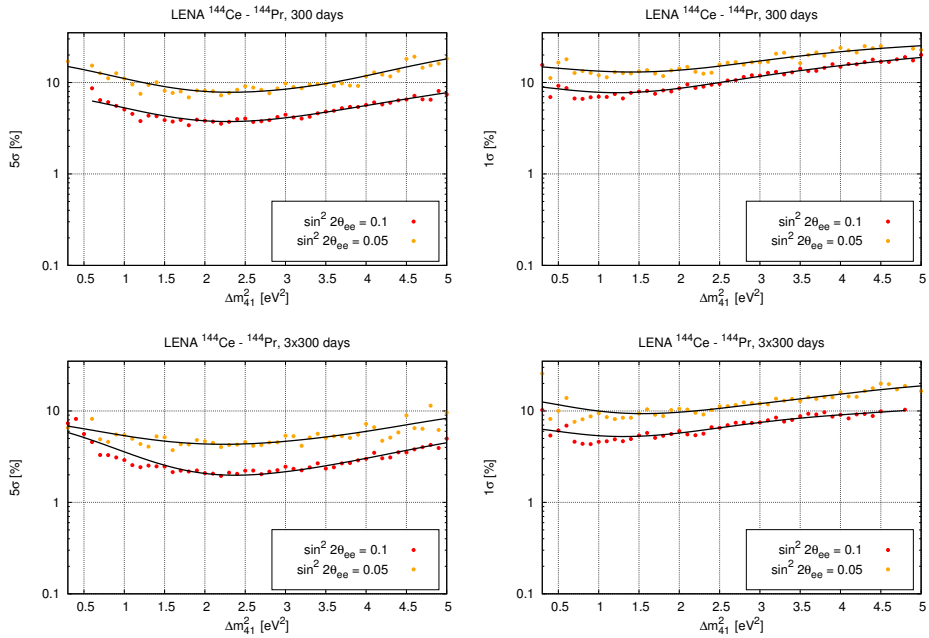

Figure 9.11.: Sensitivity reaches for Δm^2_{14} (left) and $\sin^2 2\theta_{14}$ (right) in the case of a ^{144}Ce-^{144}Pr source with exposures of 1×300 days (top) and 3×300 days (bottom). The black curves are only to guide the eye.

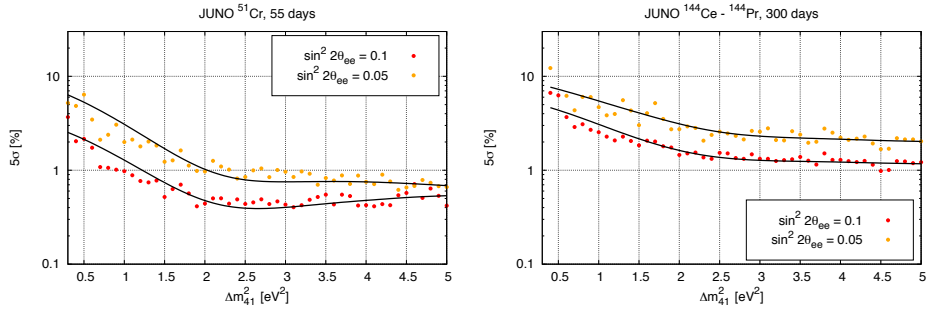

Figure 9.12.: Sensitivity of a spherical detector for Δm^2_{14} in the case of ^{51}Cr (left) and ^{144}Ce–^{144}Pr (right) with exposures of 1×55 days and 1×300 days, respectively. The black curves are only to guide the eye.

10. Flavor Discrimination with Elementary Tracking

The liquid scintillator detectors are considered as excellent tools for low energy neutrino studies, since the scintillation is an isotropic phenomenon the energy deposition at low energies (< 100 MeV) can be considered as point-like and the reconstruction of the energy, position and time of the event is possible with a point fitting algorithm. When the energy deposition increases to the GeV-level, the reconstruction of events becomes more complicated. The reconstruction relies then on Monte Carlo data and the fitting procedure requires a good initial knowledge of the event.

In this Chapter a robust first-stage track reconstruction and flavor discrimination of electron and muon events are discussed and the signatures of muon- and electron-like single particle events are illustrated. A rather robust algorithm to search for the temporal and spacial light emission to extract initial parameters for more advanced particle track fitting is introduced. It utilises the first photons arriving at the PMTs from any point of the particle track. Based on the extracted parameters, the discrimination power between electron and muon events is derived.

10.1. Signatures of Electron and Muon Events

In neutrino oscillation experiments the measurement of the energy and flavor of neutrinos is usually required. In liquid scintillator detectors, the energy measurement is based on the energy deposited by secondary particles induced by the initial neutrino interaction. Correspondence between the initial neutrino energy and the observed deposited energy is valid for the charged current interactions. However, the proper energy determination requires, still, that the secondary particles deposit their energy inside the active detector volume i.e. the event is fully contained. On the other hand, in the case of neutral current interactions, the leading final state lepton is neutrino and it carries a substantial amount of energy out from the detector. That makes the reconstruction of the initial neutrino energy impossible for neutral current events. Hence, only fully contained charged current events can be used in the analysis of high-energy neutrino experiments and neutral current interactions should be rejected.

In high-energy neutrino beam experiments muon neutrinos are produced in the accelerator. Their oscillation to the electron neutrinos are observed in far detector. Only small fraction of the produced muon neutrinos are observed as electron neutrinos, while the majority of observed events are induced by the surviving muon neutrinos.

This makes a flavor discrimination a mandatory feature of the far detector. In the charged current interactions the leading lepton in the final state is the charged one. Due to the lepton number conservation this lepton carries the same flavor as the incident neutrino. In the case of high-energy neutrino beams, these final state leptons are electrons and muons. Hence, the understanding of the detector response to the high-energy electrons and muons is crucial to make the discrimination. The oscillation to tau neutrinos may also happen and, if the neutrino energy is high enough, the leading lepton in the final state of the neutrino interaction can be also tau lepton. The tau lepton has very short mean life-time (2.9×10^{-13} s) and its decays produce a pure muon, a pure electron or, in the case of hadronic decay channels, both muon and electron via hadronic channel with branchings of 17.39%, 17.82%, and 64.79%, respectively. These reactions pose a background to both muon and electron neutrino events.

Due to their different masses, the muon and electron with the same energy deposit their energy to the medium differently. Typically the muon produces a narrow pencil-like track while the electron forms an electromagnetic shower, which is due to greater energy transfers to the medium and larger scattering angles in a single collision. In Figure 10.1 the range (track length) in polyethylene with respect to the energy of the particle is presented for electron and muon events. The elemental composition and the density of polyethylene are close to the ones of scintillator liquid LAB. The event lengths from the Monte Carlo event sample, to be described later, is also shown and are found to correspond relatively well to the approximated lengths with continuous slowing down approximation for muons [182] and estimated depth of the electromagnetic shower for electrons [42]. The difference in energy deposition pattern between electrons and muons is shown in Figure 10.2, where the longitudinal and the transversal positions of the Monte Carlo vertices along the direction of the incident muon or electron are shown. These differences forms a basis for the discrimination between muons and electrons.

As shown in Figure 10.1 and Figure 10.2, the length of the electron and muon induced tracks are typically few metres. To reconstruct the deposited energy in the event, the number of photons emitted along the track of the particle is needed. This is done by a likelihood fit to the results of Monte Carlo simulation on the detector response for different particles. The advanced event reconstruction have been studied in [129]. For the fitting, the initial values for the parameters have to be extracted from the recorded data. Such parameters can be initial vertex $\bar{x}_0$, interaction time t_0, the direction of the event $\bar{d}$, estimate for energy deposition E_0 or length of the track and the type of the particle.

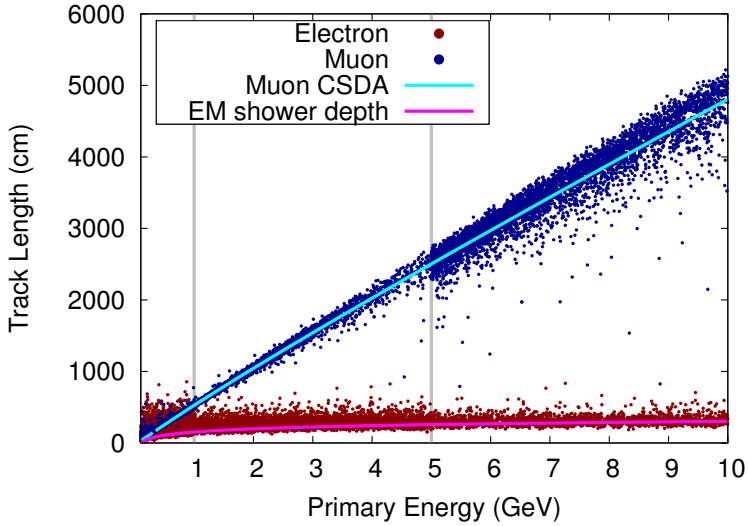

Figure 10.1.: Track lengths of a muon and the length of the electromagnetic showers initiated by electrons according the Monte Carlo simulation of the LENA detector. The vertical grey lines separate the simulated event samples with initial particle energies in the bins 0.1-1 GeV, 1-5 GeV, and 5-10 GeV. The cyan and magenta lines denote the track length of a muon with continuos slowing down approximation and calculated depth of an EM shower induced by an electron in polyethylene, respectively.

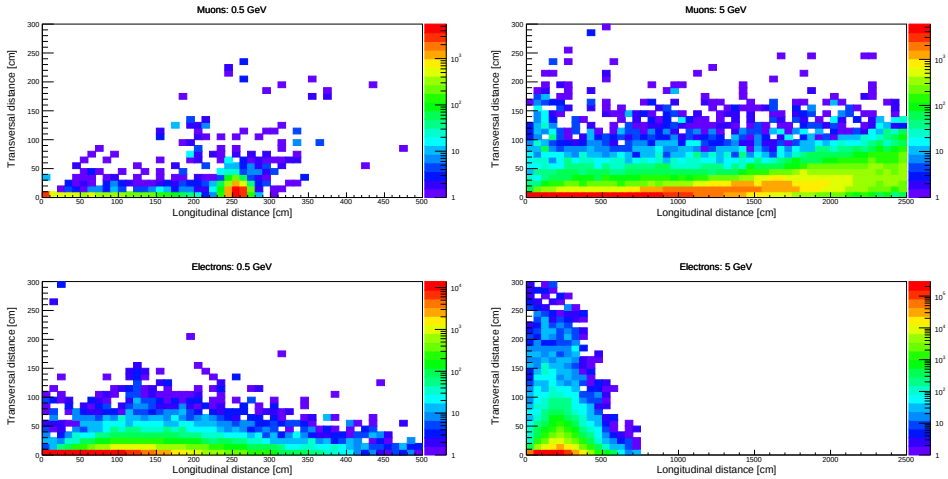

Figure 10.2.: Longitudinal and transversal distribution of the MC vertices with respect to initial vertex and direction of the incident particle. The top panels show show the muons with energies of 0.5 GeV (left) and 5 GeV (right). Lower panels illustrates the electrons with similar energies, respectively.

10.2. Search for the Origin of the Observed Light

The main aim of the algorithm developed and presented here is to study whether there has been emission of light in the selected location inside the detector. In our approach the grid of points is constructed over the detector volume and the quantity called backtracking value is calculated for all grid points. The grid points having a high backtracking values are considered as a origin of scintillation light. Furthermore, these points can be analysed to obtain rudimentary topology of the event.

To obtain a backtracking value for a selected grid point, we start with the first photon hit times in each photomultiplier tube t_i^{hit}. These hit times are the basic quantity registered in liquid scintillator experiments. For each of the hit times the so-called time-of-flight corrected time is calculated. It is a difference between the registered hit time at pmt and the time the light needs to travel from selected grid point to the photomultiplier tube. A vector of all the time-of-flight corrected times are formed and it is given by:

$$\vec{t}^{\,\text{tof}} = (t_i^{\text{tof}}) = (t_i^{\text{hit}} - \frac{n}{c}|\vec{x} - \vec{x}_i^{\,\text{pmt}}|), \tag{10.1}$$

where t_i^{hit} and $\vec{x}_i^{\,\text{pmt}}$ are the photon hit time and position of the ith photomultiplier and n and c are the refractive index of the target medium and the speed of light

in vacuum, respectively. The distribution of the time-of-flight corrected hit times (t_i^{tof}) gives a hint, whether there has been a light emission in that particular point or not. If there have been photon emission, the values in $\vec{t}_{\mathrm{tof}}$ tend to cluster around specific moment of time. This is illustrated in the top panel of Figure 10.3 for the initial vertex, one on-track point and one off-track point of a simulated event. The clustering of the time-of-flight corrected hit times, i.e. the peak in the distribution, is clearly visible for the initial vertex and on-track point, but not for the off-track point. The location of the peak gives also a handle to the time of the light emission.

According to our studies, the changes in the peak structure of the time-of-flight hit time distribution for on-track points to off-track points are slow. This is a consequence of the the decay time structure of scintillation light emission and the time resolution of the photomultiplier tubes. Hence, the distribution need to be modified to enhance the signal at the moment where the times t_i^{tof} are more clustered together. This is done by applying the differentiated gaussian function to every element of the $\vec{t}^{\mathrm{tof}}$. The gaussian shape is selected as the time resolution of the PMTs can be approximated to be gaussian. The differentiation of the gaussian function gives a larger enhancement of the clustering than the pure gaussian. At a given time t and for a given grid point $\vec{x}$ the contributions of all the time-of-flight corrected hit times are summed and it is given by

$$h(\vec{x},t) = \sum_{i=1}^{N_{\mathrm{pmts}}} h_i(\vec{x},t) = \sum_{i=1}^{N_{\mathrm{pmts}}} (t - t_i^{\mathrm{tof}}) \exp\left(-(\frac{t_i^{\mathrm{tof}} - t)^2}{2\sigma_{tts}^2}\right), \tag{10.2}$$

where, the N_{pmts} is the number of pmts taken into account, reminding that every PMT is counted once and σ_{tts} is the width of the gaussian describing the time resolution of the PMTs and is typically 1-2 ns. The obtained function $h(\vec{x},t)$ for one simulated event is shown in the middle panel of Figure 10.3 for the initial vertex, one on-track point and one off-track point. The signal enhancement is visible in the case of initial vertex and the on-track point, while in the case of off-track point enhancement relative to the previous points is suppressed. The width of the gaussian depends on the time resolution of the PMT (σ_{tts}). This step is shown in the middle panel of Figure 10.3.

Finally, to get a single value, called backtracking value, for the selected grid point and further enhance the difference between the on-track points and off-track points the integral of the $|h_i(\vec{x},t)|^2$ over time is calculated:

$$I(\bar{x}) = \int_{-\infty}^{\infty} |h_i(\vec{x},t)|^2 dt. \tag{10.3}$$

This is illustrated in the bottom panel in Figure 10.3. The backtracking value is the area of the between the curve and the time-axis. The enhanced distributions of initial

vertex and on-track point are enhanced a lot while the distribution for the off-track point is barely visible. When this algorithm is calculated for all the grid points, the points with high backtracking value can be considered as a potential locations of the light emission and selected for further analysis.

10.3. Simulation

To study the performance of LENA for high-energy particles, the two simulation event samples were produced. For simplicity, and because the flavor sensitivity is the key issue in many GeV-region neutrino phenomena, single electron and muon events were simulated resembling the main part of the light production in charged current neutrino interactions. The event samples consist of two samples with discrete energies (0.5 GeV and 5 GeV) and three samples with continuos flat energy spectrum: low (0.1-1 GeV), intermediate (1-5 GeV), and high energies (5-10 GeV). The major part of the simulations have been conducted in the Taito supercluster at the CSC computer centre.

The initial vertex and the direction of the primary charged particle were selected randomly within the detector volume. As the scintillation photon yield is typically of the order of 10 000 photons per 1 MeV of deposited energy, in high-energy particle events the number of photons to be simulated will be enormous. To reduce the required computation time only 20% of the generated photons were transported and were registered with 100% efficiency when hitting the PMT. This would correspond to the measurement with, nowadays rather conservative, assumption of the 20% quantum efficiency of PMTs and reduces the computation time by a factor of five. The registered times of the photon hits at the PMTs were smeared with the assumed time resolution function (gaussian distribution with 1 ns standard deviation).

For the analysis, only the fully contained events, i.e. the events where all energy is deposited inside the scintillating volume, were included. The desired statistics of the simulation campaign was selected so that for discrete energies at least 1000 fully contained events is achieved and for continuous spectra every would have at least 100 events in every 1 GeV bin. The full statistics of each energy category obtained in simulation campaign are summarised Table 10.1.

10.3.1. Parameter Extraction

To extract the parameters describing a given event, the backtracking values along with the corresponding estimate of the emission time, were calculated over the rectangular grid of points with 20 cm spacing. To select the most interesting points and to obtain the time evolution of the event, the highest backtracking point within time

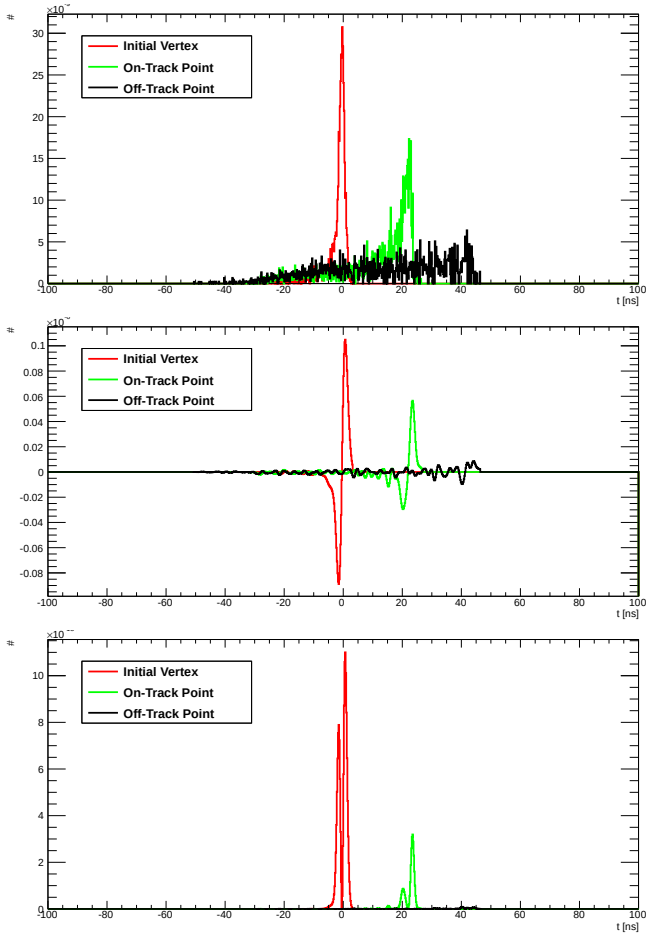

Figure 10.3.: Illustration of the steps of the backtracking algorithm. The top panel shows the clustering of the time-of-flight corrected hit times at each PMT for inital vertex (red), one on-track point (green) and one off-track point (black). The enhancement of the clustering by applying the differentiated gaussian function to each hit time is shown in mid panel. The backtracking estimator for vertex, on-track point and off-track point is the area of between the curve and horizontal axis shown in the bottom panel.

Energy	Electrons	Muons
Continuous, Flat		
0.1-1 GeV	4000	4000
1-5 GeV	2300	2400
5-10 GeV	1800	4480
Discrete		
0.5 GeV	2300	2400
5 GeV	1900	2200

Table 10.1.: Number of fully contained simulated events in different energy categories entering to our analysis.

intervals of 1 ns was selected. The average time evolution of the backtracking value of the muon and electron events corresponding to the energies of 0.5 and 5 GeV are shown in Figure 10.4. The estimates for the duration of the light emission and for the start of time of the event can be obtained from the time evolution. The development of the scintillation light takes some time, hence the peak of the pulse is shifted by 1-2 ns on average. The distribution of the start time estimates obtained by subtracting, 2 ns from the time location of the peak for each individual event, are shown in Figure 10.5 for muons and electrons with energies of 0.5 GeV and 5 GeV. The majority of the reconstructed start times for electrons are within the 2 ns from true start time, being $t = 0$ in the Figure 10.5. Nevertheless, especially in the case of muons, the reconstructed time is greater than true start time and this behaviour is even enhanced when the muon energy increases. In these particular mis-reconstructed events the initial vertex is further away from the detector walls (PMTs) and the direction of the particle is towards the wall. The similar behaviour holds for the distance of the backtracking point with the highest backtracking value from the location of the initial vertex as shown in Figure 10.6.

To obtain the direction of particle, the 3-dimension line is fitted to the selected grid points with weighting each point with its backtracking values. Then all the points are projected to that line and the longitudinal length estimate is obtained from the two most distant points on the fitted line. The comparison of the reconstructed direction to the initial direction of the incident particle for event samples with discrete energy is shown in Figure 10.7 and for samples with continuous energy in Figure 10.8. As expected, the higher the energy the better the directional accuracy since the longitudinal size of the event grows.

One can try to estimate also the location of the initial vertex from the projected grid points. The results are shown in Figure 10.9. The results are comparable with the ones obtained just by selecting the grid point with the highest backtracking value.

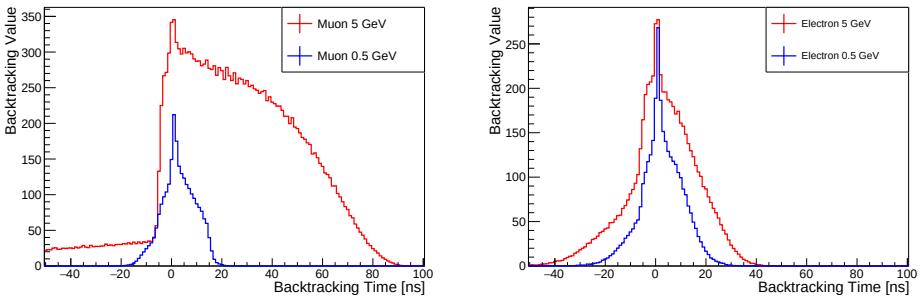

Figure 10.4.: Time evolution of the event according to the points with highest backtracking value in every 1 ns time bin for initial particle energy of 0.5 GeV and 5 GeV. The left panel shows the result for muons and the right panel for electrons.

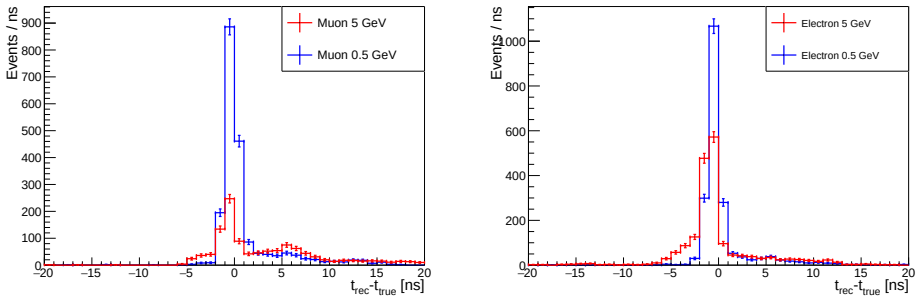

Figure 10.5.: Reconstructed time of the highest backtracking point in the case of single muon events (left) and single electron events (right) for different energy categories

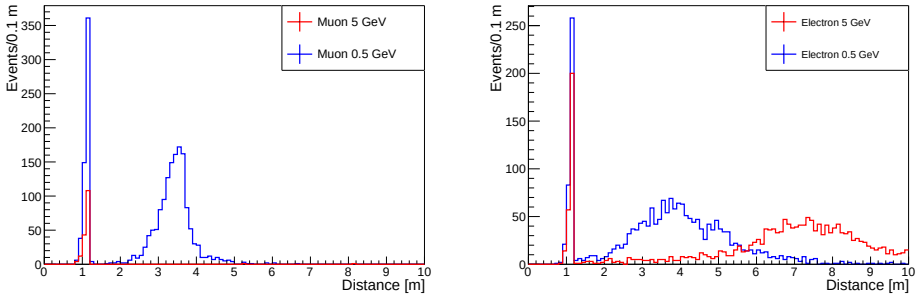

Figure 10.6.: Extracted location of the point with the highest backtracking value with respect to the location of the initial vertex for particles with energy of 0.5 GeV and 5 GeV . The left panel shows the result for muons and the right panel for electrons.

This is due to initial selection of the grid points entering to the analysis. From the simulations the closest distance from fit line to the initial vertex position can be also calculated. This shown in Figure 10.10. Relatively small distances from the reconstructed fitted line and true initial vertex shows that the initial vertex can be found from the vicinity of the fitted line. To do this more advanced, second stage, algorithm should be developed and it was beyond the scope of this work.

Finally, from the grid points projected to the fitted line, one can get an estimate for the longitudinal length of the event. The illustrations of the extracted longitudinal length of the muon and electron events with initial energies of 0.5 GeV and 5 GeV are shown in Figure 10.11. It shows that there is some possibility to make discrimination between the muon induced and electron induced events already at relatively low energies.

10.4. Discrimination Based on Extracted Event Length

The extracted length of the events as a function of true energy of the initial particle for the simulated event samples of muons and electrons with continuous energy spectra is shown in Figure 10.12. It shows that the extracted lengths from the backtracking values of the grid points follow the similar behaviour as was presented in Figure 10.1. In both Figures 10.12 and 10.1, the lengths are presented as a function of true energy of the initial particle. The true energy is available in the simulation, but not directly in the case of real experiment. Hence, the true energy have to be replaced with some measurable quantity describing the deposited energy. In scintillators the number

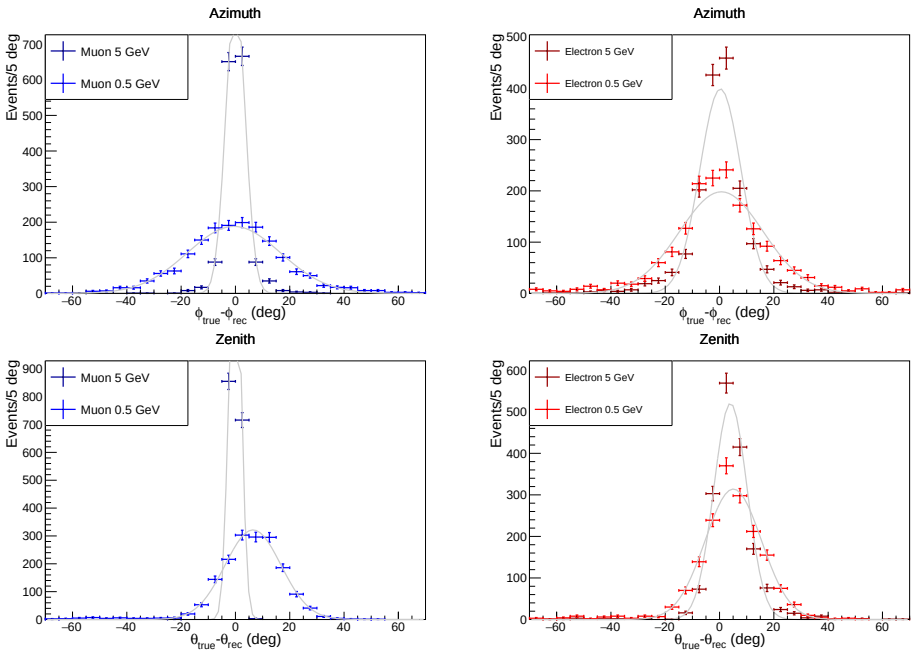

Figure 10.7.: Reconstruction accuracy of the direction of the incident particle. The top panels show the reconstruction result for azimuth angle and bottom panels for the zenith angle of the direction of the track. The left panels show the results for muons and the right panels for electrons.

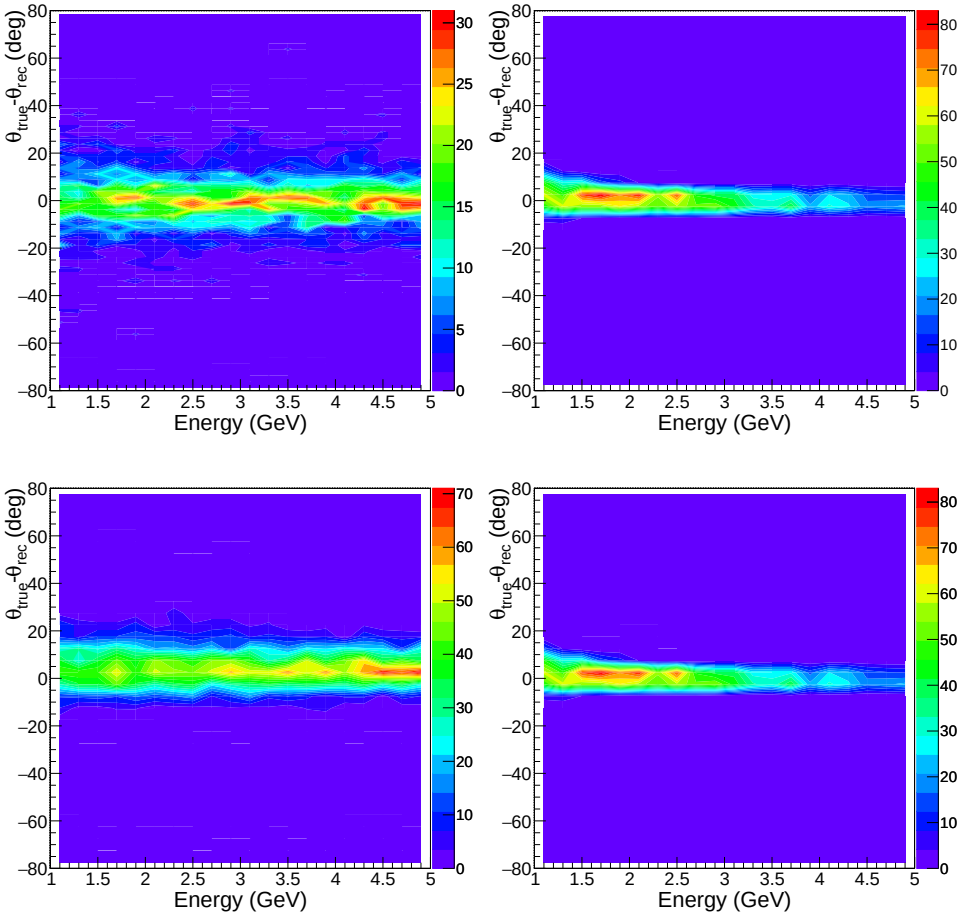

Figure 10.8.: Distribution of the reconstructed direction of the incident particle with the continuous energy spectra from 1 GeV to 5 GeV. The top panels show the distribution of the reconstructed azimuth angle and bottom panels the distributions of the reconstructed zenith angle. In the left panels the incident particles are electrons and in the right panels muons.

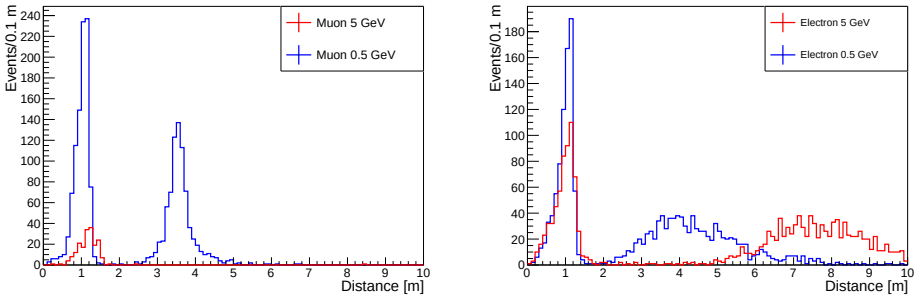

Figure 10.9.: Extraction of initial vertex of the event from the end point on fitted line with respect to the true initial vertex. The left panel shows the results for muon with energy of 0.5 GeV and 5 GeV. The right panel is for electrons with same energies.

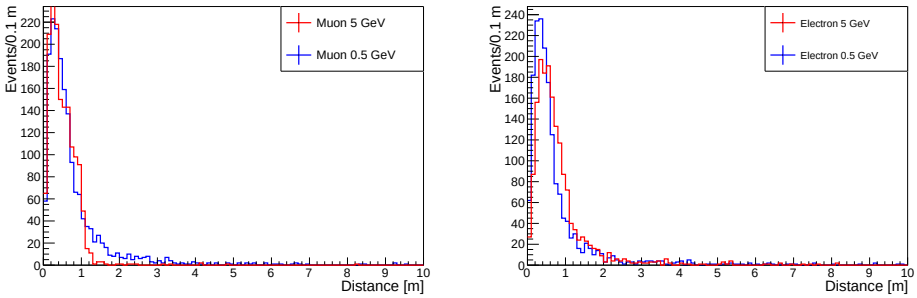

Figure 10.10.: The closest distance from fitted line to the true initial vertex position. The left panel shows the results for muon with energy of 0.5 GeV and 5 GeV. The right panel is for electrons with same energies.

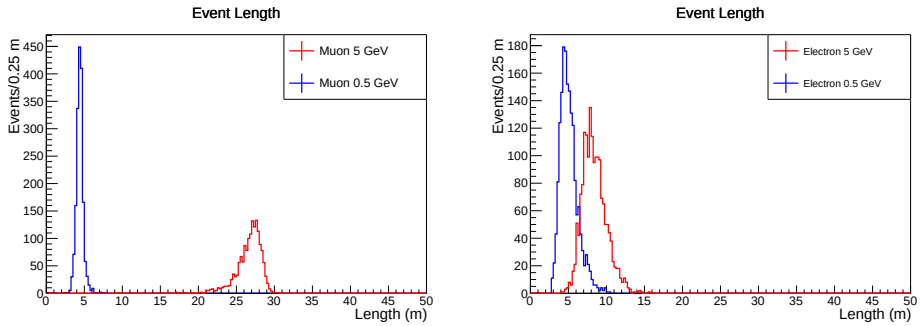

Figure 10.11.: The extracted longitudinal length of the event. The left panel shows the results for muon with energy of 0.5 GeV and 5 GeV. The right panel is for electrons with same energies.

of scintillation photons emitted corresponds the amount of energy deposited to the target.

In principle, the number of registered photons is also a measure of deposited energy. Actually, the photomultiplier tubes measure the number of photoelectrons (p.e.) released from the photocathode, usually called the charge collected. In real experiment the energy deposition is obtained with an event reconstruction algorithm. In the case of low energy events, the point-fitting algorithm is used. However, the point-fitting is not applicable to high-energy events, as the light emission is not point-like. Here we use the total number of registered photons i.e. the total number of photoelectrons (charge) collected from the event as a measure of energy. Figure 10.13 shows the relation between true energy and the total charge collected from the event. It shows that the charge collected is roughly same from the events induced by muons and by electrons with same initial energy. Now we can relate our measure of energy and the extracted length of the event. That is shown in Figure 10.14 for muons and electrons. The difference between the muon and electron events is clearly visible above 0.03×10^7 photoelectrons showing that the discrimination is possible above the 1 GeV of the deposited energy.

To evaluate the power of discrimination, a condition when the event is considered as muon event or electron event must be set. For that purpose we introduce a linear discrimination function denoted by black line in Figure 10.14 (note the logarithmic scale of the horizontal axis). The events that have extracted length longer for the amount of charge collected than given by the discrimination function are considered as muons, otherwise they are considered as electrons. The discrimination efficiency depends then on two components. They are the efficiency how well the the desired

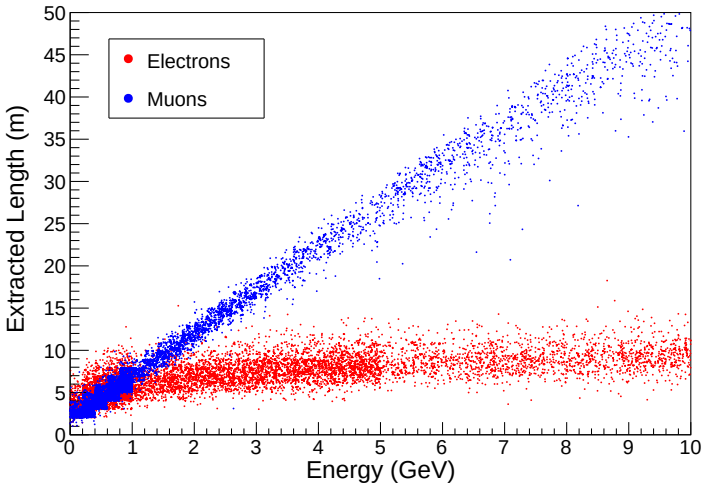

Figure 10.12.: The extracted length of the event with respect to the true energy of the primary particle for muon (blue) and electrons (red).

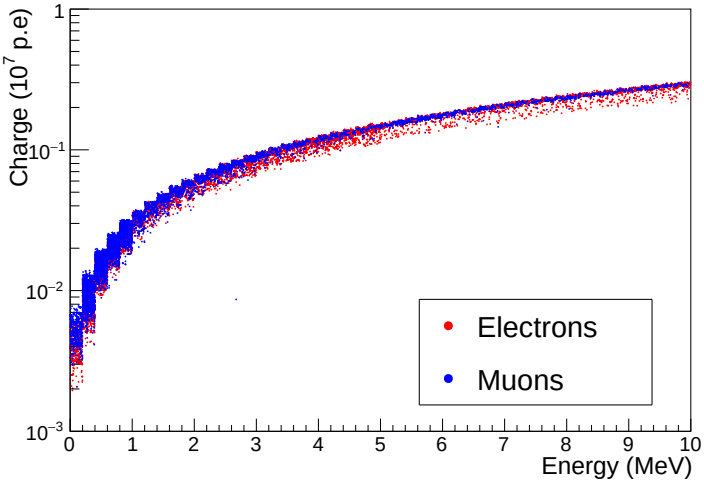

Figure 10.13.: The relation between the energy of the primary particle and the charge (number of photoelectrons) collected from the event.

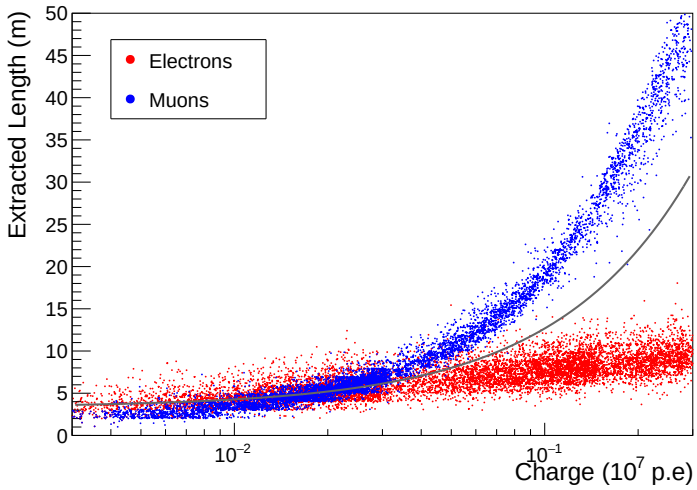

Figure 10.14.: The extracted event length with respect to the the charge (number of photoelectrons) collected from the event. Muons are shown in blue and electrons in red. The black line is the example of the discrimination function (see text).

particle type can be selected and what is the level of contamination of the other events from the other particle type. Figure 10.15 shows these two cases for both muons and electrons for our selection of the discrimination function. In the left panel of Figure 10.15, the muons are considered as the desired signal. It shows that the muons are effectively selected, but at low energies the amount of mis-identified electron events increases drastically. The right panel of Figure 10.15 shows the result in the case where, the desired signal is the electron events. With our discrimination function the efficiency to select only the electron events is worse at the low energies compared with the muon signal. Due to the limited statistics of the event samples in each 1 GeV bin, the discrimination presented here is more illustration than the properly determined values.

10.5. Conclusions

When the physics programme of the large liquid scintillator detector like LENA is extended from MeV-level to GeV-level energy depositions, the light emission can not be considered to be point-like. The event reconstruction have to be modified to look

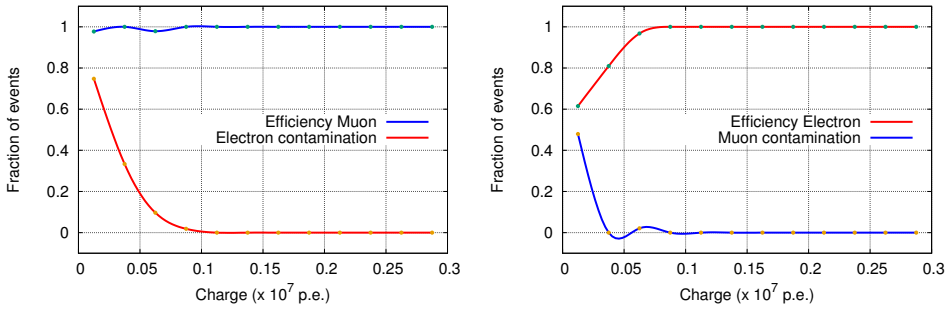

Figure 10.15.: The discrimination efficiency and the contamination of mis-identified wrong-type events for muon-like events (left) and electron-like events (right).

for the light emission locations inside the detector active volume. In this chapter the algorithm utilising the clustering of the back-projected photon hit times of the PMTs to the locations inside the detector volume has been introduced. The most reliable outcome of the algorithm is the direction of particle track (muons) or the direction of electromagnetic shower induced by electron. This is represented as a fitted line which restricts the location of the event inside the detector. By projecting the obtained most probable light emission points to that line, the measure of the longitudinal size of the events can be obtained. Furthermore, the length estimate combined with total charge collected from the event can be used to make the discrimination between the muon-like and electron-like events. Our results show that the effective discrimination should be possible above 0.05×10^7 p.e. of charge collected corresponding roughly 1.5 GeV of deposited energy. At lower energies the discrimination would give additional parameter for other reconstruction methods.

11. Study of Leptonic CP-violation in Daeδalus and LENA-type Detectors

In neutrino oscillation studies using high-energy neutrino beams the liquid argon detectors, like GLACIER [6], is found to be more effective than the scintillator detectors like LENA. In the LAGUNA-LBNO design study the sensitivity of LENA for CP violation was estimated to be below 3σ level in general. The main reason for this is insufficient statistics of the fully contained events. A different radius vs. height ratio of the cylindrical detector could help with that, but this would compromise the low energy physics program of the detector. Also the insufficient background rejection capability, mainly due to the electron-π_0 discrimination weakens the sensitivity. As the liquid scintillator detectors are more suitable for the detection of the low energy neutrinos, using low-energy neutrinos would result better sensitivities.

The use of low energy neutrinos from the pion decay-at-rest (DAR) beams produced with cyclotrons has been proposed as an alternative and complementary method to a search for leptonic CP-violation [105]. This so-called Daeδalus approach turns the typical scenario of the neutrino oscillation experiment with one single neutrino source and at least two detectors at different distances from the source upside-down. In Daeδalus the neutrinos produced in three cyclotron-driven pion decay-at-rest beams with different baselines are detected with a single large liquid scintillator detector.

In this chapter we shall estimate the sensitivity of Daeδalus and LENA detector to measure the CP violation taking into account the current knowledge of the detector performance.

11.1. Basic Scheme of Daeδalus Approach

Due to the kinematics the DAR beam produces flux of low energy neutrinos (ν_μ, $\bar{\nu}_\mu$, ν_e) with energy below 52.8 MeV. The energy spectra of different neutrino flavors are shown in Figure 11.1. The muon neutrino originates in the decay $\pi^+ \rightarrow \mu^+ + \nu_\mu$ and it is mono-energetic with energy of 29.8 MeV. The subsequent decay of stopped muon, $\mu+ \rightarrow \bar{\nu}_\mu + e^+ + \nu_e$, emits muon antineutrino and electron neutrino with a well defined shapes of the energy spectra.

After the neutrino propagation from the beam target to the detector some kilometres away, the main observed signal will be the appearance of electron antineutrino events.

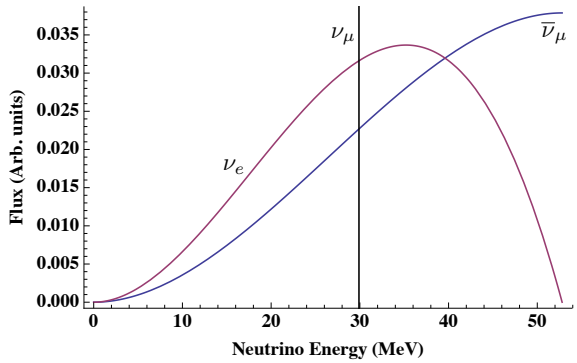

Figure 11.1.: Energy spectrum of neutrinos originating from decay-at-rest neutrino beam [105].

The conversion probability is given by

$$\begin{aligned} P(\bar{\nu}_\mu \to \bar{\nu}_e) &= \sin^2\theta_{23}\sin^2 2\theta_{13}\sin^2\Delta_{31} \\ &+ \sin\delta_{CP}\sin 2\theta_{13}\sin 2\theta_{23}\sin 2\theta_{12}\sin^2\Delta_{31}\sin\Delta_{21} \\ &+ \cos\delta_{CP}\sin 2\theta_{13}\sin 2\theta_{23}\sin 2\theta_{12}\sin\Delta_{31}\cos\Delta_{31}\sin\Delta_{21} \\ &+ \cos^2\theta_{23}\sin^2 2\theta_{12}\sin^2\Delta_{21}, \end{aligned} \tag{11.1}$$

where the θ_{ij} are neutrino mixing angles and $\Delta_{ji} = \frac{\Delta m^2_{ji} L}{2E}$ the oscillation phase. The non-zero CP violating phase (δ_{CP}) would alter the second and third term of the oscillation probability function. The effect of this phase to the shape of the probability function is illustrated in Figure 11.2. The different values of the δ_{CP} change the behaviour of the probability function in certain ranges of the L/E parameter space, while at certain L/E values (1000 and 10000 in Figure 11.2) the δ_{CP} does not affect the probability (nodes). These features of the probability function restricts the baseline-neutrino energy combinations sensitive to δ_{CP}.

To cover reasonable part of the L/E parameter space of the probability function, shown in Figure 11.2, the Daeδalus approach proposes to use three sites, with different baseline lengths, equipped with high-power accelerators (cyclotrons) producing DAR neutrino beam. Distances of the neutrino sources are selected to be 1.5 km, 8 km and 20 km from the detector site, so that they cover different ranges of the L/E parameter space. The energy range relevant in this approach starts from 15 MeV due to the background sources and extends to the end point energy of the Michel spectrum of

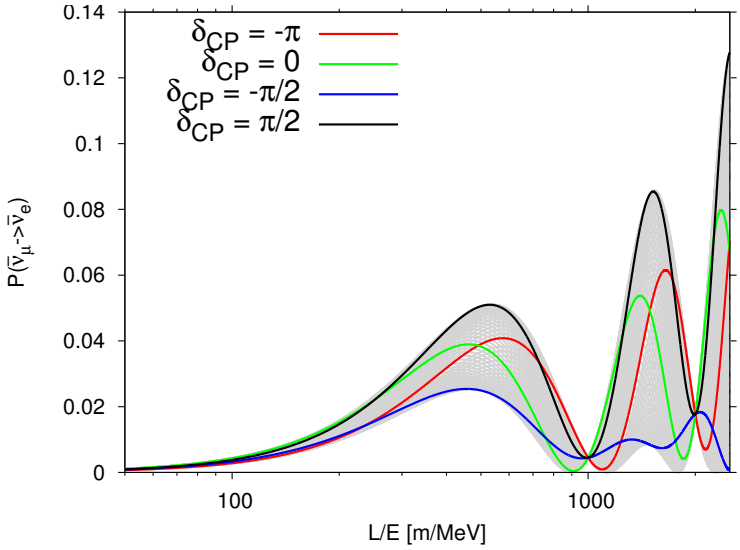

Figure 11.2.: The oscillation probability $P(\bar{\nu}_\mu \to \bar{\nu}_e)$ as a function of L/E for the CP phase values $\delta_{CP} = \pi/2, 0, -\pi/2, -\pi$. The shaded area corresponds δ_{CP} varying in the range from $-\pi$ to $+\pi$.

the muon antineutrinos at 52.8 MeV. The first cyclotron at 1.5 km distance would cover L/E -values from 28 to100, the second cyclotron at 8 km L/E values from 150 to 500 and the third cyclotron from 400 to 1300. With this setup one would thus cover a wide range of the probability function (see Figure 11.2).

11.2. Neutrino production

The DAR neutrino beam will be produced with the accelerator module, where the protons are accelerated and shot to a fixed target. To obtain sufficiently large beam energies, the chain of accelerators leading to neutrino production could, for example, consists of the low energy compact injector cyclotron, which accelerates H_2^+ ions to 60 MeV/n energy. That first stage accelerator is followed by the high energy, super-conducting ring cyclotron, for further acceleration, up to 800 MeV/n, exceeding the pion production threshold. After acceleration the beam hits the target, where 0.17 π^+/proton are produced and stopped. After the subsequent decays the neutrinos are produced as described in previous section.

In this work we assume the cyclotrons at the distances at 1.5 km, 8 km, and 20 km to run with 1 MW, 2 MW, and 5 MW average powers, respectively. This leads to the neutrino production rate of $\sim 1.3 \times 10^{15}$ neutrinos /flavor/s/MW. As the detection with the liquid scintillation technique does not allow the reconstruction of the direction of the incident neutrino, to know from which cyclotron a given neutrino comes, the neutrino production must be pulsed and synchronised. In this work, the following pulsing scenario have been used: 1/4 of the time the neutrinos are coming from each of the accelerator module and 1/4 of the time the background level is measured (for instance, 100 μs accelerator 1, 100 μs from accelerator 2, 100 μs from accelerator 3 and 100 μs beam off measurement). The whole setup is assumed to be operational 80% throughout the full measurement time. Recent studies show that it is feasible to build such powerful pulsed cyclotrons. The details of the accelerator designs proposed for the DAR neutrino beam in Daeδalus could be found from [183].

11.3. Neutrino Detection

The part of the produced muon antineutrino will be detected as electron antineutrinos after the flight from DAR beam target to the detector i.e. the electron antineutrino appearance signal is observed. The main channel to detect electron antineutrinos is the inverse β decay $\bar{\nu}_e + p \rightarrow e^+ + n$. The effect of different values of CP violation phase to the shape of the appearance spectrum of electron antineutrinos is shown in Figure 11.3. The shape of spectra from the accelerators at 8 km and 20 km distance changes with different values of the δ_{CP}, while the spectrum from the closest

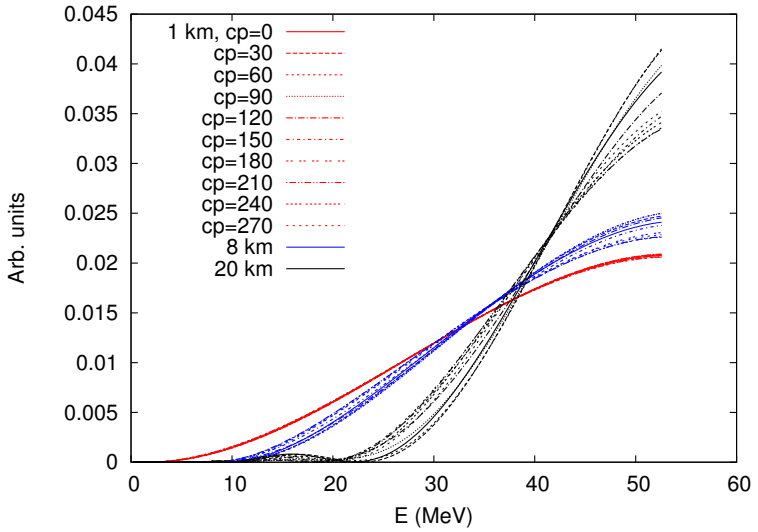

Figure 11.3.: The shape of the energy spectrum of electron antineutrino appearance event with different values of δ_{CP}. The spectra from accelerator at the distance of 1.5 km, 8 km and 20 km is shown in red, blue and black, respectively. The different values of δ_{CP} is denoted by the dashing of the lines.

accelerator does not depend on δ_{CP}. This feature is useful for normalisation of the signal. Within 10 years of measurement one expects to detect of the order of 300-500 DAR electron antineutrino events in LENA-sized detector. In addition there will be neutrino scattering events on electrons. These are possible for all flavors of neutrinos. Furthermore, both electron neutrinos and antineutrinos from the beam can interact with the carbon nuclei of the scintillator. The reactions are shown in Table 6.3. These reactions would give additional information to normalise the beam flux.

As the total number of events collected will be relatively low, the division of them to the multiple energy bins results in a large statistical uncertainty. Hence, in this work, we focus only on the robust event-rate-only analysis.

The major uncertainties affecting the determination of the δ_{CP} come from

- **The normalisation of the signal.** In the baseline design of Daeδalus, the electron-neutrino scattering events from the near accelerator are used to obtain an absolute normalisation of the flux. The other signal from interactions with oxygen (in water Cherenkov detector) is used to check the relative flux normalisations of the different accelerator sites. A similar normalisation can

be done with the scintillator detector, but instead of oxygen the reaction on carbon will be used. It has been estimated, that in Daeδalus the uncertainty in normalization will be 1.1% in the case of large water-Cherenkov detector. As LENA is considerably smaller and due to identification efficiency of the reactions on carbon, we have assumed 2.5% uncertainty for the total normalisation which includes also the fiducial volume uncertainty.

- **The uncertainty of the other oscillation parameters.** These uncertainties affect the expected behaviour oscillation probability function (Equation 11.2). That causes systematic uncertainty to the expected number of event and energy spectra of events from accelerator and hampers the determination of δ_{CP}. The effect of the uncertainties induced by the other oscillation parameters except δ_{CP} is illustrated in Figure 11.4. The spread is largest for the most distant accelerator at 20 km distance from the detector.
- **The Low event rate.** Rather poor statistics of few hundred events introduces relatively large statistical uncertainty to the measured event rates even in the case of event rate-only analysis.
- **The background levels.** As this measurement will have rather low statistics, understanding the sources of background and effective background rejection is needed. However, even a low remaining background event rate after the rejection introduces large effect to the level of systematic uncertainty.

11.4. The Background Signals

The background consist of the events induced by electron antineutrinos originating in sources like the neutrino beam itself, nuclear reactors and the β radioactivity in the Earth. Other component of the background is the events that mimic the delayed coincidence signal of the inverse beta decay induced by atmospheric neutrinos, fast neutrons. The Daeδalus approach allows the measurement of the levels of background during the off-line period of the cyclotrons. This verifies the background levels and the performance of background rejection methods. In following, the rejection of the background signals and level of the left-over background entering to our analysis is introduced.

11.4.1. Electron Antineutrino Background

The DAR beam contains a small flux of electron antineutrinos from negatively $\pi^- \to e^- + \bar{\nu}_e$ decays. Fortunately π^- and μ^- are efficiently captured by the atoms

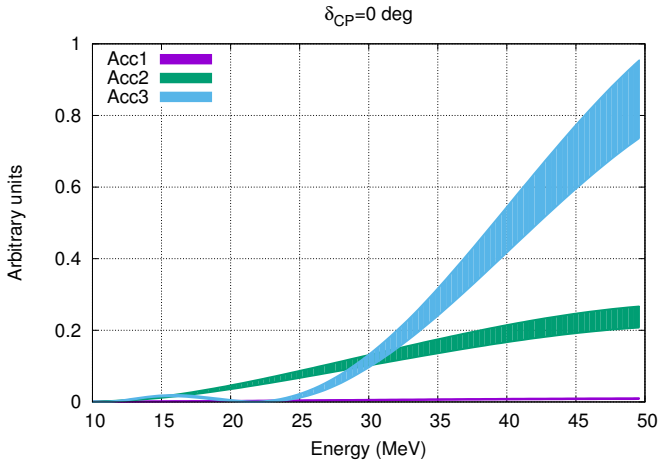

Figure 11.4.: The spread in the energy spectra of the events caused by the uncertainties of other oscillation parameters than the CP violation phase ($\delta_{CP} = 0$). Different bands shows the spread associated to cyclotrons with baselines of 1.5 km (magenta), 8 km (green) and 20 km (cyan), respectively.

of the target medium and the total contamination of this intrinsic background is at the level of 5×10^{-4} compared with the muon antineutrino flux and can be neglected.

Other sources of electron antineutrinos taken into consideration are the decays of radioactive isotopes in the Earth, nuclear reactors, cosmogenic β-active radioisotopes and cosmic-ray induced processes in the atmosphere. The first three are rejected by applying a 15 MeV low-energy cut for the energy window used in the analysis. The atmospheric neutrinos entering to the analysis window can not be avoided. The shape of the spectrum of atmospheric CC interaction events is shown in blue in Figure 11.5. In ten-year measurement with one accelerator (20% duty factor) the remaining background rate in 15-50 MeV window is about 7-8 events.

11.4.2. Other Backgrounds

The signals that mimic the delayed coincidence signature of the inverse beta decay reaction are the fast neutrons originating from the cosmic muon traversing in rock and the neutral current interaction of atmospheric neutrinos. Without applying any discrimination method, the level of the background events in ten years of measurement with one accelerator (20% duty factor) would be $\sim$ 2500 events in a 47.8 kton of

	Atmospheric NC	Fast neutrons
100% acceptance	1860	654
95% acceptance	206	45
90% acceptance	81	14
80% acceptance	44	6

Table 11.1.: The effect of different acceptance cuts of the inverse β decay to the background events from neutral current interactions of atmospheric neutrinos and fast neutrons induced by cosmic muons traversing in surrounding rock. The event rates corresponds to the measurement with single cyclotron with assumed 20% duty cycle in ten years.

scintillator. Compared with the signal from cyclotrons, which is about 500-700 events in ten years, this background is huge. The major part of these background events can be rejected by accepting only the events, where the assumed prompt signal from positron annihilation is followed by the signal from neutron capture with narrower time and energy windows around the expected expected capture time (250 μs) and energy deposit (2.2 MeV). The detailed description of the discrimination methods can be found in [138]. The event selection cuts out also a part of the events from cyclotrons, but on the other hand it increases the signal to background ratio significantly. The Figure 11.5 illustrates the influence of IBD acceptance to the different background sources. The effective rejection of the neutral current events of atmospheric neutrinos and events induced by fast neutrons is possible, especially. Table 11.1 show the remaining background after rejection. In this analysis the 80% IBD acceptance is used providing relatively low background rates without cutting the signal too much.

11.5. Simulation and Results

The Monte Carlo method is used to construct the events from the different accelerators and events induced by the remaining background after the rejection for 10 years of measurement time. To obtain the event rate corresponding the signal from accelerators the expected background is subtracted. The background events are constructed from the spectrum with 80% inverse beta decay acceptance (bottom left plot in Figure 11.5). The statistical uncertainty of the observed background events is taken into account. The expected number of events from the mid accelerator at 8 km and far accelerator at 20 km distance for different values of the CP violating phase δ_{CP} is shown in Figure 11.6 with 10 degree spacing in the values of δ_{CP}. The values of the δ_{CP} alter the event rates so, that they form a circular pattern.

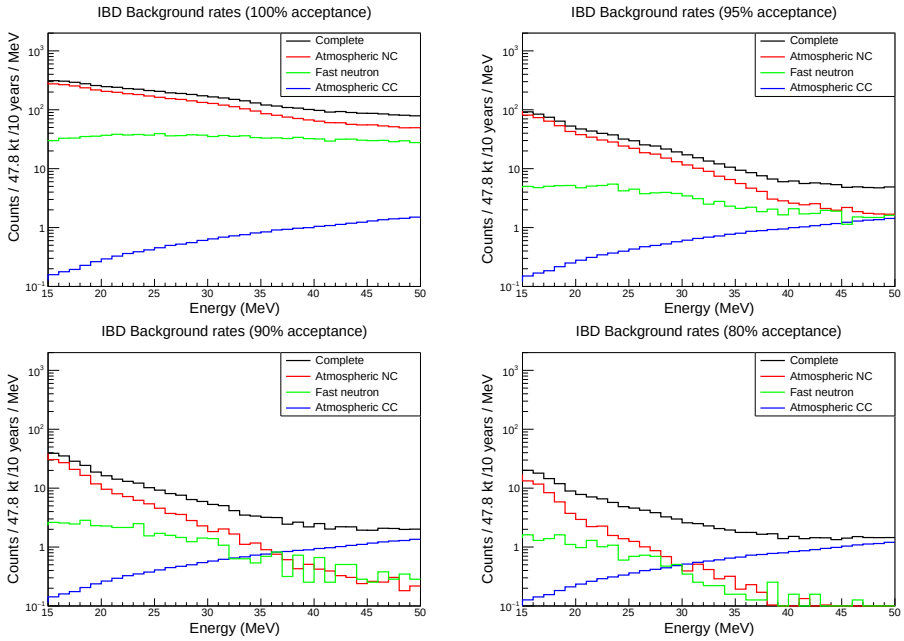

Figure 11.5.: The energy spectra of neutral current events (red) and charged current events (blue) of atmospheric neutrinos, and fast neutrons (green) for 100% (top left), 95% (top right), 90% (bottom left), and 80% (bottom right) acceptance of inverse β decay events. The black line shows the sum of all components.

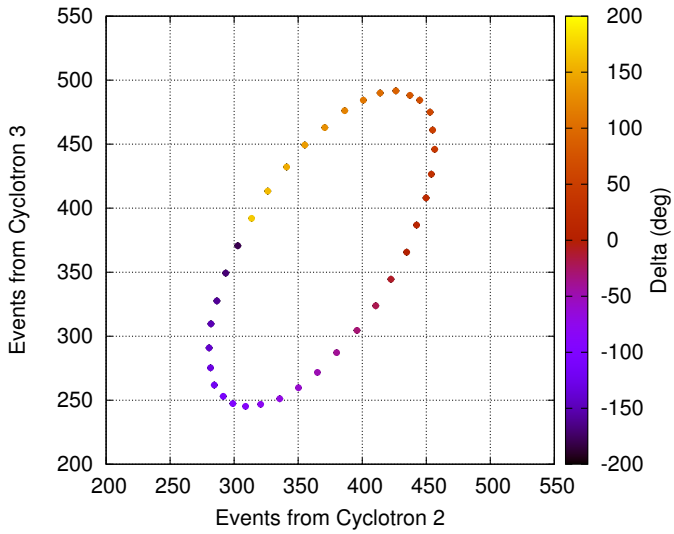

Figure 11.6.: Event rates from cyclotrons at the distances of 8 km (vertical axis) and 20 km (horizontal axis) without uncertainties. The colour coding shows the value of the CP value violation phase δ_{CP}.

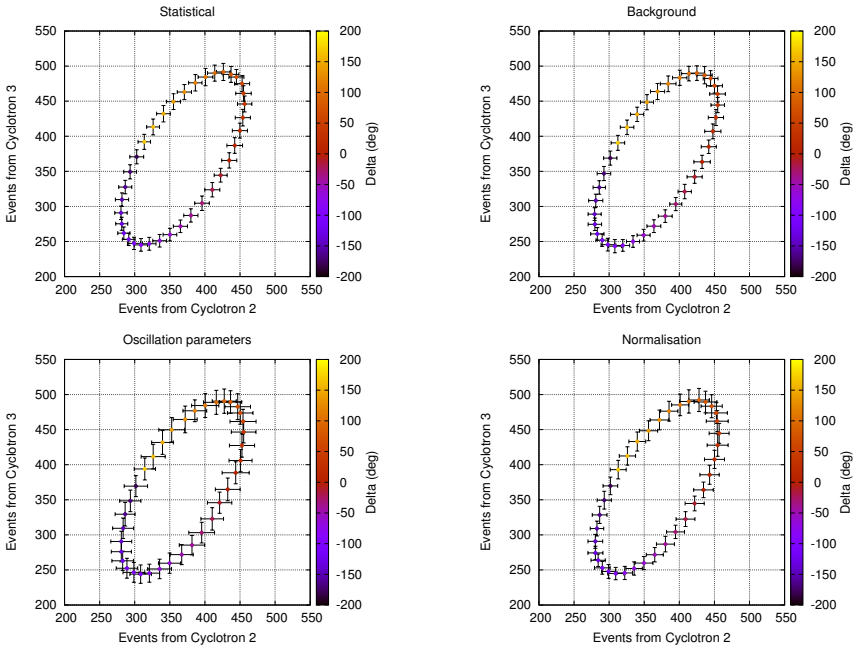

Figure 11.7.: The effect of different sources of uncertainty on the event rates from cyclotrons at the distances of 8 km (Cyclotron 2) and 20 km (Cyclotron 3): the statistical fluctuation (upper left), uncertainty caused by background rejection (upper right), other oscillation parameters (lower left) and normalisation (lower right).

To evaluate the effect of the uncertainties, the measurement is constructed 20000 times with a variation of the signal normalisations and the oscillation parameters for set of δ_{CP} values covering the whole parameter space $[-\pi, \pi]$. In Figure 11.7, the effect of each considered source of uncertainties is depicted individually with 1σ errors. The all effects combined is given in Figure 11.8. In Figure 11.9 the 1σ confidence boundary is presented as a function of the CP-violation phase δ_{CP} for LENA-type detector and for a three times bigger similar detector (the largest possible detector that could be built in the Pyhäsalmi mine). These results confirm that LENA and Daeδalus alone cannot achieve high confidence level measurement of the value of CP violation phase δ_{CP}. The uncertainties introduced by the low statistics and the oscillation parameters have the highest effect.

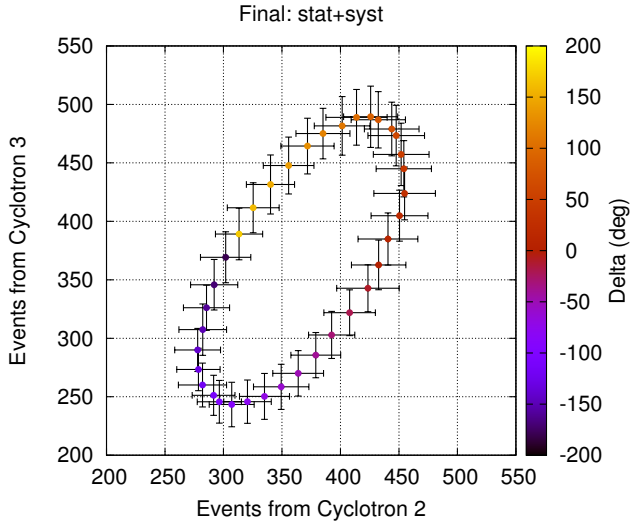

Figure 11.8.: The number of expected electron neutrino appearance events from cyclotron 2 at 8 km (vertical axis) and cyclotron 3 at 20 km distance (horizontal axis) and their uncertainties with respect to the value of δ_{CP} (colour coded).

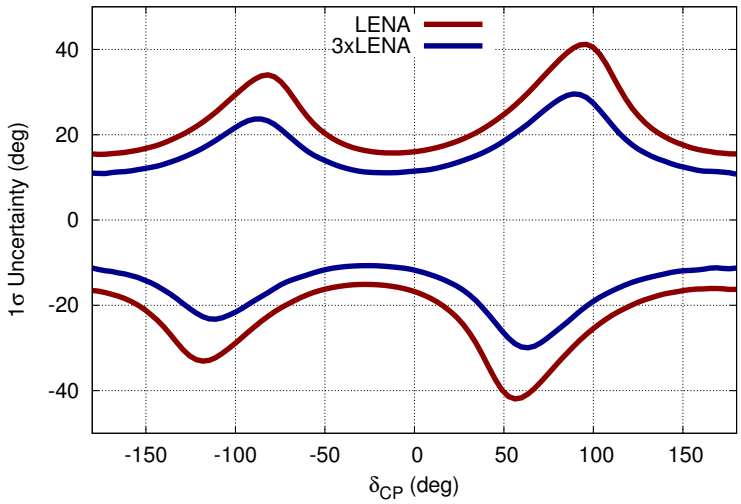

Figure 11.9.: The 1σ uncertainty for the measurement of δ_{CP} with Daeδalus and LENA based on the event rate only analysis.

12. Summary of the Thesis and Outlook

In this work, the studies related to the extending physics potential of large liquid scintillator detector have been presented. The studies have been conducted in connection to liquid scintillator working group in LAGUNA Design Studies aiming at the next-generation large neutrino observatory in Europe. Within LAGUNA, the design, construction and operation of the 50 kiloton liquid scintillator detector (LENA) have been planned.

The main content of this work applies the detailed detector response studies of the baseline design of LENA to the various neutrino related topics. Especially, the experimental scenarios studying the neutrino properties going beyond the usual astrophysics viewpoint of the large liquid scintillator detectors, are in focus.

The reactors are the main source of background for geoneutrino measurement. As the proposed location for LENA is the Pyhäsalmi mine and there are intentions to construct new nuclear power plants in Finland, the current level of the flux of reactor neutrinos and the estimate for the future flux have been calculated and the impact of the increase of the reactor neutrino flux to the geoneutrino measurement in Pyhäsalmi was evaluated. The results show that among the LAGUNA sites Pyhäsalmi has the lowest reactor neutrino background flux. The future increase of this background do not have crucial impact to the geoneutrino measurement because the neutrino production in reactors is relatively well known and possible to estimate accurate enough by fitting.

Instead of typical scenario of neutrino oscillation experiments in which the oscillation probability curve is probed with at least two separate detectors with different baselines, LENA can offer a $\sim$100 m long continuous baseline for oscillometric measurement. In this work, the sensitivities to measure the parameters governing the oscillation from electron neutrino to sterile neutrino flavor with oscillometric measurement have been evaluated in the simplest 3+1 scenario. The results show that the energy and position reconstruction resolutions of LENA are good enough to cover the interesting part of the parameter space indicated by the global fits. The sources electron neutrinos and antineutrinos have been considered. This opens the way to probe the CPT and CP symmetry with neutrinos.

When extending the physics program of large liquid scintillator detectors to higher energy depositions of few GeV, the non-isotropic light emission of the final state particle(s) must be taken into account in event reconstruction. In this thesis the algo-

rithm to search for light emission locations inside the detector to perform elementary tracking of charged particles is introduced. The algorithm can be used for especially tagging of high-energy muon events and extracting their initial directions. This is crucial for example for atmospheric neutrino measurement and if the large liquid scintillator detector is considered as far detector for high-energy neutrino beam. As an example, the method have been used to the muon-electron discrimination.

LENA has been considered also for the measurement of CP-violation phase of the neutrino mixing matrix. Instead of the high-energy neutrino beam proposed in LAGUNA-LBNO, the method using three high-power cyclotrons (Daeδalus approach) was discussed. The sensitivity to extract the value of δ_{CP} have been evaluated taking into account the current estimated background rejection capability of LENA. Due to the relatively poor statistics, it was found that the significance level of the measurement is insufficient. The results confirmed that the Daeδalus approach combined with LENA alone is not the most prominent way to probe the value of CP-violation phase.

During the time span of this work, the emphasis of the LAGUNA changed from the measurement of astrophysical neutrinos using them as messengers to the high-energy beam neutrinos probing the fundamental properties of neutrinos. That kind of development diminished the role of liquid scintillator technique inside the project. This development lead also to the merging of the European and American long-baseline community to the DUNE collaboration aiming at the long-baseline experiment utilising liquid argon technique in United States.

All in all, the results, construction methods and plans, and other information acquired in several design studies related to LENA, including LAGUNA, are applicable to the other liquid scintillator detectors like JUNO, RENO-50, and THEIA. First practical test will be JUNO, as the experiment is under construction in China. Furthermore, as the JUNO is dedicated to the reactor neutrino measurement and it is not diminishing the importance of the larger liquid scintillator detector to study the neutrinos from astrophysical sources. The plans to construct such detector in the Pyhäsalmi mine are ready.

A. List of Author's Publications and Presentions

List of most relevant publications related to the thesis

K. K. Loo, N. Yu Novikov, M. V. Smirnov, W. H. Trzaska and M. Wurm, "Omnibus experiment: CPT and CP violation with sterile neutrinos," J. Phys. Conf. Ser. **718** (2016) no.6, 062063.

W. H Trzaska on behalf of WA105 collaboration, LBNO-DEMO (WA105): a large demonstrator of the Liquid Argon double phase TPC, PoS(PhotoDet2015)054

M. V. Smirnov, K. K. Loo, Y. N. Novikov, W. H. Trzaska and M. Wurm, "A search for neutrino-antineutrino mass inequality by means of sterile neutrino oscillometry," Nucl. Phys. B **900** (2015) 104

K. K. Loo *et al.*, "Neutrino Flavor Sensitivity of Large Liquid Scintillator Detectors," Phys. Procedia **61** (2015) 488.

K. Loo, T. Enqvist, J. Hissa, D. Nesterenko, Y. N. Novikov, W. H. Trzaska, J. Vergados and M. Wurm, "Hunt for Theta(13) with LENA," J. Phys. Conf. Ser. **375** (2012) 042053.

M. Wurm *et al.* [LENA Collaboration], "The next-generation liquid-scintillator neutrino observatory LENA," Astropart. Phys. **35** (2012) 685 [arXiv:1104.5620 [astro-ph.IM]].

K. Loo, T. Enqvist and W. H. Trzaska, "Reactor neutrino background at the proposed LAGUNA sites," Nucl. Phys. Proc. Suppl. **229-232** (2012) 518.

List of publications related to LENA and LAGUNA

S. K. Agarwalla *et al.* [LAGUNA-LBNO Collaboration], "The LBNO long-baseline oscillation sensitivities with two conventional neutrino beams at different baselines," arXiv:1412.0804 [hep-ph].

S. K. Agarwalla *et al.* [LAGUNA-LBNO Collaboration], "Optimised sensitivity to leptonic CP violation from spectral information: the LBNO case at 2300 km baseline," arXiv:1412.0593 [hep-ph].

L. Agostino *et al.*, "LBNO-DEMO: Large-scale neutrino detector demonstrators for phased performance assessment in view of a long-baseline oscillation experiment," arXiv:1409.4405 [physics.ins-det].

S. K. Agarwalla *et al.* [LAGUNA-LBNO Collaboration], "The mass-hierarchy and CP-violation discovery reach of the LBNO long-baseline neutrino experiment," JHEP **1405** (2014) 094 [arXiv:1312.6520 [hep-ph]].

M. Wurm *et al.*, "Low-energy Neutrino Astronomy in LENA," Phys. Procedia **61** (2015) 376.

A. Stahl *et al.*, "Expression of Interest for a very long baseline neutrino oscillation experiment (LBNO)," CERN-SPSC-2012-021, SPSC-EOI-007.

W. H. Trzaska *et al.*, "Advantages of locating LAGUNA in Pyhaesalmi mine," Prog. Part. Nucl. Phys. **66** (2011) 463.

W. H. Trzaska *et al.*, "LAGUNA in Pyhaesalmi," Acta Phys. Polon. B **41** (2010) 1779.

Y. N. Novikov *et al.*, "Neutrino oscillometry at the next generation neutrino observatory," arXiv:1110.2983 [physics.ins-det].

J. Kisiel *et al.* [LAGUNA Collaboration], "The LAGUNA project: Towards the giant liquid based detectors for proton decay searches and for low energy neutrino astrophysics," PoS EPS **-HEP2009** (2009) 283.

D. Angus *et al.* [LAGUNA Collaboration], "The LAGUNA design study-towards giant liquid based underground detectors for neutrino physics and astrophysics and proton decay searches," arXiv:1001.0077 [physics.ins-det].

List of publications related to cosmic-ray physics

J. Sarkamo *et al.*, "EAS selection in the EMMA underground array," J. Phys. Conf. Ser. **409** (2013) 012086.

P Kuusiniemi *et al.*, "Underground cosmic-ray experiment EMMA,", J. Phys. Conf. Ser. **409** (2013) 012067.

P. Kuusiniemi *et al.*, "Underground multi-muon experiment EMMA," Astrophys. Space Sci. Trans. **7** (2011) 93.

T. Kalliokoski *et al.*, "Can EMMA solve the puzzle of the knee?," Prog. Part. Nucl. Phys. **66** (2011) 468.

T. Enqvist *et al.*, "Research options in the Pyhäsalmi Underground Facility," Nucl. Phys. Proc. Suppl. **143** (2005) 561.

List of publications related to ALICE

B. Abelev *et al.* [ALICE Collaboration], "Upgrade of the ALICE Experiment: Letter Of Intent," J. Phys. G **41** (2014) 087001.

B. B. Abelev *et al.* [ALICE Collaboration], "Long-range angular correlations of π, K and p in p-Pb collisions at $\sqrt{s_{\rm NN}}$ = 5.02 TeV," Phys. Lett. B **726** (2013) 164 [arXiv:1307.3237 [nucl-ex]].

B. Abelev *et al.* [ALICE Collaboration], "Multiplicity dependence of two-particle azimuthal correlations in pp collisions at the LHC," JHEP **1309** (2013) 049 [arXiv:1307.1249 [nucl-ex]].

B. B. Abelev *et al.* [ALICE Collaboration], "Multiplicity dependence of the average transverse momentum in pp, p-Pb, and Pb-Pb collisions at the LHC," Phys. Lett. B **727** (2013) 371 [arXiv:1307.1094 [nucl-ex]].

B. B. Abelev *et al.* [ALICE Collaboration], "Energy Dependence of the Transverse Momentum Distributions of Charged Particles in pp Collisions Measured by ALICE," Eur. Phys. J. C **73** (2013) 12, 2662 [arXiv:1307.1093 [nucl-ex]].

B. Abelev *et al.* [ALICE Collaboration], "Directed Flow of Charged Particles at Midrapidity Relative to the Spectator Plane in Pb-Pb Collisions at $\sqrt{s_{NN}}$=2.76 TeV," Phys. Rev. Lett. **111** (2013) 23, 232302 [arXiv:1306.4145 [nucl-ex]].

E. Abbas *et al.* [ALICE Collaboration], "Performance of the ALICE VZERO system," JINST **8** (2013) P10016 [arXiv:1306.3130 [nucl-ex]].

B. Abelev *et al.* [ALICE Collaboration], "D meson elliptic flow in non-central Pb-Pb collisions at $\sqrt{s_{\rm NN}}$ = 2.76TeV," Phys. Rev. Lett. **111** (2013) 102301 [arXiv:1305.2707 [nucl-ex]].

E. Abbas *et al.* [ALICE Collaboration], "Mid-rapidity anti-baryon to baryon ratios in pp collisions at $\sqrt{s}$ = 0.9, 2.76 and 7 TeV measured by ALICE," Eur. Phys. J. C **73** (2013) 2496 [arXiv:1305.1562 [nucl-ex]].

E. Abbas *et al.* [ALICE Collaboration], "Charmonium and e^+e^- pair photoproduction at mid-rapidity in ultra-peripheral Pb-Pb collisions at $\sqrt{s_{\rm NN}}$=2.76 TeV," Eur. Phys. J. C **73** (2013) 11, 2617 [arXiv:1305.1467 [nucl-ex]].

E. Abbas *et al.* [ALICE Collaboration], "Centrality dependence of the pseudorapidity density distribution for charged particles in Pb-Pb collisions at $\sqrt{s_{\rm NN}}$ = 2.76 TeV," Phys. Lett. B **726** (2013) 610 [arXiv:1304.0347 [nucl-ex]].

E. Abbas *et al.* [ALICE Collaboration], "J/Psi Elliptic Flow in Pb-Pb Collisions at $\sqrt{s_{\rm NN}}$ = 2.76 TeV," Phys. Rev. Lett. **111** (2013) 162301

B. Abelev *et al.* [ALICE Collaboration], "Centrality dependence of π, K, p production in Pb-Pb collisions at $\sqrt{s_{NN}} = 2.76$ TeV," Phys. Rev. C **88** (2013) 044910 [arXiv:1303.0737 [hep-ex]].

B. Abelev *et al.* [ALICE Collaboration], "Centrality determination of Pb-Pb collisions at $\sqrt{s_{NN}} = 2.76$ TeV with ALICE," Phys. Rev. C **88** (2013) 4, 044909 [arXiv:1301.4361 [nucl-ex]].

B. Abelev *et al.* [ALICE Collaboration], "Charge correlations using the balance function in Pb-Pb collisions at $\sqrt{s_{NN}} = 2.76$ TeV," Phys. Lett. B **723** (2013) 267 [arXiv:1301.3756 [nucl-ex]].

B. Abelev *et al.* [ALICE Collaboration], "Measurement of the inclusive differential jet cross section in *pp* collisions at $\sqrt{s} = 2.76$ TeV," Phys. Lett. B **722** (2013) 262 [arXiv:1301.3475 [nucl-ex]].

B. Abelev *et al.* [ALICE Collaboration], "Charged kaon femtoscopic correlations in *pp* collisions at $\sqrt{s} = 7$ TeV," Phys. Rev. D **87** (2013) 5, 052016 [arXiv:1212.5958 [hep-ex]].

B. Abelev *et al.* [ALICE Collaboration], "Long-range angular correlations on the near and away side in *p*-Pb collisions at $\sqrt{s_{NN}} = 5.02$ TeV," Phys. Lett. B **719** (2013) 29 [arXiv:1212.2001 [nucl-ex]].

B. Abelev *et al.* [ALICE Collaboration], "Transverse momentum distribution and nuclear modification factor of charged particles in *p*-Pb collisions at $\sqrt{s_{NN}} = 5.02$ TeV," Phys. Rev. Lett. **110** (2013) 8, 082302 [arXiv:1210.4520 [nucl-ex]].

B. Abelev *et al.* [ALICE Collaboration], "Pseudorapidity density of charged particles in p + Pb collisions at $\sqrt{s_{NN}} = 5.02$ TeV," Phys. Rev. Lett. **110** (2013) 3, 032301 [arXiv:1210.3615 [nucl-ex]].

B. Abelev *et al.* [ALICE Collaboration], "Coherent J/ψ photoproduction in ultra-peripheral Pb-Pb collisions at $\sqrt{s_{NN}} = 2.76$ TeV," Phys. Lett. B **718** (2013) 1273 [arXiv:1209.3715 [nucl-ex]].

B. Abelev *et al.* [ALICE Collaboration], "Production of $K^*(892)^0$ and $\phi(1020)$ in *pp* collisions at $\sqrt{s} = 7$ TeV," Eur. Phys. J. C **72** (2012) 2183 [arXiv:1208.5717 [hep-ex]].

B. Abelev *et al.* [ALICE Collaboration], "Measurement of inelastic, single- and double-diffraction cross sections in proton–proton collisions at the LHC with ALICE," Eur. Phys. J. C **73** (2013) 6, 2456 [arXiv:1208.4968 [hep-ex]].

B. Abelev *et al.* [ALICE Collaboration], "Centrality Dependence of Charged Particle Production at Large Transverse Momentum in Pb–Pb Collisions at $\sqrt{s_{\rm NN}} = 2.76$ TeV," Phys. Lett. B **720** (2013) 52 [arXiv:1208.2711 [hep-ex]].

B. Abelev *et al.* [ALICE Collaboration], "Pion, Kaon, and Proton Production in Central Pb–Pb Collisions at $\sqrt{s_{NN}} = 2.76$ TeV," Phys. Rev. Lett. **109** (2012) 252301 [arXiv:1208.1974 [hep-ex]].

B. Abelev *et al.* [ALICE Collaboration], "D_s^+ meson production at central rapidity in proton–proton collisions at $\sqrt{s} = 7$ TeV," Phys. Lett. B **718** (2012) 279 [arXiv:1208.1948 [hep-ex]].

B. Abelev *et al.* [ALICE Collaboration], "Measurement of electrons from beauty hadron decays in *pp* collisions at $\sqrt{s} = 7$ TeV," Phys. Lett. B **721** (2013) 13 [arXiv:1208.1902 [hep-ex]].

B. Abelev *et al.* [ALICE Collaboration], "Net-Charge Fluctuations in Pb-Pb collisions at $\sqrt{s}_{NN} = 2.76$ TeV," Phys. Rev. Lett. **110** (2013) 15, 152301 [arXiv:1207.6068 [nucl-ex]].

B. Abelev *et al.* [ALICE Collaboration], "Charge separation relative to the reaction plane in Pb-Pb collisions at $\sqrt{s_{NN}} = 2.76$ TeV," Phys. Rev. Lett. **110** (2013) 1, 012301 [arXiv:1207.0900 [nucl-ex]].

B. Abelev *et al.* [ALICE Collaboration], "$K_s^0 - K_s^0$ correlations in *pp* collisions at $\sqrt{s} = 7$ TeV from the LHC ALICE experiment," Phys. Lett. B **717** (2012) 151 [arXiv:1206.2056 [hep-ex]].

B. Abelev *et al.* [ALICE Collaboration], "Production of muons from heavy flavour decays at forward rapidity in pp and Pb-Pb collisions at $\sqrt{s_{NN}} = 2.76$ TeV," Phys. Rev. Lett. **109** (2012) 112301 [arXiv:1205.6443 [hep-ex]].

B. Abelev *et al.* [ALICE Collaboration], "Measurement of prompt J/ψ and beauty hadron production cross sections at mid-rapidity in *pp* collisions at $\sqrt{s} = 7$ TeV," JHEP **1211** (2012) 065 [arXiv:1205.5880 [hep-ex]].

B. Abelev *et al.* [ALICE Collaboration], "Anisotropic flow of charged hadrons, pions and (anti-)protons measured at high transverse momentum in Pb-Pb collisions at $\sqrt{s_{NN}}$=2.76 TeV," Phys. Lett. B **719** (2013) 18 [arXiv:1205.5761 [nucl-ex]].

B. Abelev *et al.* [ALICE Collaboration], "Neutral pion and η meson production in proton-proton collisions at $\sqrt{s} = 0.9$ TeV and $\sqrt{s} = 7$ TeV," Phys. Lett. B **717** (2012) 162 [arXiv:1205.5724 [hep-ex]].

B. Abelev *et al.* [ALICE Collaboration], "Measurement of electrons from semileptonic heavy-flavour hadron decays in pp collisions at $\sqrt{s} = 7$ TeV," Phys. Rev. D **86** (2012) 112007 [arXiv:1205.5423 [hep-ex]].

B. Abelev *et al.* [ALICE Collaboration], "Measurement of charm production at central rapidity in proton-proton collisions at $\sqrt{s} = 2.76$ TeV," JHEP **1207**

(2012) 191 [arXiv:1205.4007 [hep-ex]].

B. Abelev *et al.* [ALICE Collaboration], "Transverse sphericity of primary charged particles in minimum bias proton-proton collisions at $\sqrt{s} = 0.9$, 2.76 and 7 TeV," Eur. Phys. J. C **72** (2012) 2124 [arXiv:1205.3963 [hep-ex]].

B. Abelev *et al.* [ALICE Collaboration], "Multi-strange baryon production in *pp* collisions at $\sqrt{s} = 7$ TeV with ALICE," Phys. Lett. B **712** (2012) 309 [arXiv:1204.0282 [nucl-ex]].

B. Abelev *et al.* [ALICE Collaboration], "Inclusive J/ψ production in *pp* collisions at $\sqrt{s} = 2.76$ TeV," Phys. Lett. B **718** (2012) 295 [arXiv:1203.3641 [hep-ex]].

B. Abelev *et al.* [ALICE Collaboration], "Measurement of the Cross Section for Electromagnetic Dissociation with Neutron Emission in Pb-Pb Collisions at $\sqrt{s_{NN}} = 2.76$ TeV," Phys. Rev. Lett. **109** (2012) 252302 [arXiv:1203.2436 [nucl-ex]].

B. Abelev *et al.* [ALICE Collaboration], "Suppression of high transverse momentum D mesons in central Pb-Pb collisions at $\sqrt{s_{NN}} = 2.76$ TeV," JHEP **1209** (2012) 112 [arXiv:1203.2160 [nucl-ex]].

B. Abelev *et al.* [ALICE Collaboration], "J/ψ Production as a Function of Charged Particle Multiplicity in *pp* Collisions at $\sqrt{s} = 7$ TeV," Phys. Lett. B **712** (2012) 165 [arXiv:1202.2816 [hep-ex]].

B. Abelev *et al.* [ALICE Collaboration], "J/ψ suppression at forward rapidity in Pb-Pb collisions at $\sqrt{s_{NN}} = 2.76$ TeV," Phys. Rev. Lett. **109** (2012) 072301 [arXiv:1202.1383 [hep-ex]].

B. Abelev *et al.* [ALICE Collaboration], "Heavy flavour decay muon production at forward rapidity in proton?proton collisions at $\sqrt{s} = 7$ TeV," Phys. Lett. B **708** (2012) 265 [arXiv:1201.3791 [hep-ex]].

B. Abelev *et al.* [ALICE Collaboration], "Measurement of Event Background Fluctuations for Charged Particle Jet Reconstruction in Pb-Pb collisions at $\sqrt{s_{NN}} = 2.76$ TeV," JHEP **1203** (2012) 053 [arXiv:1201.2423 [hep-ex]].

B. Abelev *et al.* [ALICE Collaboration], "Light vector meson production in *pp* collisions at $\sqrt{s} = 7$ TeV," Phys. Lett. B **710** (2012) 557 [arXiv:1112.2222 [nucl-ex]].

B. Abelev *et al.* [ALICE Collaboration], "Underlying Event measurements in *pp* collisions at $\sqrt{s} = 0.9$ and 7 TeV with the ALICE experiment at the LHC," JHEP **1207** (2012) 116 [arXiv:1112.2082 [hep-ex]].

B. Abelev *et al.* [ALICE Collaboration], "Measurement of charm production at

central rapidity in proton-proton collisions at $\sqrt{s} = 7$ TeV," JHEP **1201** (2012) 128 [arXiv:1111.1553 [hep-ex]].

B. Abelev *et al.* [ALICE Collaboration], "J/ψ polarization in pp collisions at $\sqrt{s} = 7$ TeV," Phys. Rev. Lett. **108** (2012) 082001 [arXiv:1111.1630 [hep-ex]].

K. Aamodt *et al.* [ALICE Collaboration], "Particle-yield modification in jet-like azimuthal di-hadron correlations in Pb-Pb collisions at $\sqrt{s_{NN}} = 2.76$ TeV," Phys. Rev. Lett. **108** (2012) 092301 [arXiv:1110.0121 [nucl-ex]].

K. Aamodt *et al.* [ALICE Collaboration], "Harmonic decomposition of two-particle angular correlations in Pb-Pb collisions at $\sqrt{s_{NN}} = 2.76$ TeV," Phys. Lett. B **708** (2012) 249 [arXiv:1109.2501 [nucl-ex]].

K. Aamodt *et al.* [ALICE Collaboration], "Higher harmonic anisotropic flow measurements of charged particles in Pb-Pb collisions at $\sqrt{s_{NN}}$=2.76 TeV," Phys. Rev. Lett. **107** (2011) 032301 [arXiv:1105.3865 [nucl-ex]].

K. Aamodt *et al.* [ALICE Collaboration], "Rapidity and transverse momentum dependence of inclusive J/ψ production in pp collisions at $\sqrt{s} = 7$ TeV," Phys. Lett. B **704** (2011) 442 [Phys. Lett. B **718** (2012) 692] [arXiv:1105.0380 [hep-ex]].

K. Aamodt *et al.* [ALICE Collaboration], "Elliptic flow of charged particles in Pb-Pb collisions at 2.76 TeV," Phys. Rev. Lett. **105** (2010) 252302 [arXiv:1011.3914 [nucl-ex]].

K. Aamodt *et al.* [ALICE Collaboration], "Charged-particle multiplicity density at mid-rapidity in central Pb-Pb collisions at $\sqrt{s_{NN}} = 2.76$ TeV," Phys. Rev. Lett. **105** (2010) 252301 [arXiv:1011.3916 [nucl-ex]].

List of presentations given by the author since 2010

LBNO-DEMO (WA105): a large demonstrator of the liquid Argon double phase TPC,
Neutrinos and Dark Matter in Nuclear Physics 2015, 1.-5. 6. 2015, Jyväskylä

Progress and Status of the Analysis and Simulation Packages,
EMMA Scientific Advisory Board meeting, 11.05.2015, Jyväskylä

Measurement of oscillation parameters of sterile neutrinos with large liquid scintillator detector,
Annual meeting of the Finnish Physical Society, 18.03.2015, Helsinki

Tracking with Large Scintillator Detectors,
Particle Physics Day 2014, 24. 10. 2014, Jyväskylä

Neutriino, hiukkanen jota ei pitänyt havaita,
Higgs theme week at Tietomaa Science Centre, 15.10.2014, Oulu

Hiukkasfysiikkaa kaivoksessa,
Voionmaan lukion 100-vuotis juhlaviikko, 7.10.2014, Jyväskylä

Comparison of SC16 simulation with data from 2x2 setup in station F,
EMMA Days, 25.9.2014 Pyhäjärvi

Simulation framework for EMMA: current status,
EMMA Days 08.05.2014, Pyhäjärvi

Event reconstruction of high-energy neutrino interactions in large liquid scintillator detectors (poster),
XXVI International Conference on Neutrino Physics and Astrophysics,
06.06.2014, Boston

Neutrino flavor sensitivity of large liquid scintillator detector (poster),
Annual meeting of the Finnish Physical Society, 12.03.2014, Tampere

Artificial neural networks in EMMA data analysis,
EMMA Day, 13.12.2013, Pyhäjärvi

Miksi hiukkaset kiinnostavat,
Fysiikan teemaviikko Tiedekeskus Tietomaa, 20.11.2013, Oulu

Neutrino flavor sensitivity of large liquid scintilllator detectors,
International Conference on Topics in Astroparticle and Underground Physics,
10.09.2013 , Asilomar

Research potential of the Pyhäsalmi mine in Finland (poster),
TAUP Summer School, 08.09.2013, Asilomar

LENA as a far detector for accelerator-based neutrinos,
EMMA Scientific Advisory Board meeting, 16.05.2013, Pyhäjärvi

Long Baseline oscillations
Daya Bay II - LENA meeting, 18.04.2013, Munich

Update on high energy simulations and detector performance of LSc ,
LAGUNA-LBNO General Meeting, 26.02.2013, Hamburg

LAGUNA: laitteet ja tiede,
Kansainvälisen suurhankkeen vaikutus yrittäjän arkeen -semiaari, 18.10.2012,
Pyhäjärvi

LAGUNA-project, simulation and data-analysis tools for LENA-experiment,
Seminar on HPC: Nuclear and Particle physics at CSC, 8.10.2012 Espoo

Studies for top muon veto for LSc option,
LAGUNA-LBNO General Meeting, 2.10.2012, CERN

Update on LSc High Energy performance and backtracking,
LAGUNA-LBNO General Meeting, 3.7.2012, Oxford

3D backtracking in liquid scintillator,
LAGUNA-LBNO General Meeting 13.-15.3.2012, Paris

Geo- and reactor neutrinos,
LAGUNA-LBNO Kick off meeting, 17.-19.10.2011, CERN

LENA as a far detector for neutrino beams (poster),
European Strategy for Neutrino Oscillation Physics II, 14.-16.5.2012, Cern
XXV International Conference of Neutrino Physics and Astrophysics (Neutrino 2012), 3.-9. 6. 2012, Kyoto

Hunt for theta13 with LENA (poster),
12th International Conference on Topics in Astroparticle and Underground Physics (TAUP 2011), 5.-9.9.2011, Munich

Hunting theta13 in Very Short Baseline Neutrino Oscillations (poster),
Annual meeting of the Finnish Physical Society,
The second Nordic physics meeting, 29-31. 3. 2011, Helsinki

Reactor Neutrinos as a Background for Low Energy Neutrino Astronomy in The LAGUNA -Project (poster),
Annual meeting of the Finnish Physical Society, 11.-13. 3. 2010, Jyväskylä

LENA as a far detector for accelerator-based neutrinos
EMMA Scientific Advisory Board meeting,15.5.-17.5.2013, Pyhäjärvi

Staus of LAGUNA-LBNO,
EMMA Days, 22.-23.11.2012, Pyhäjärvi

Status of LENA Simulation,
EMMA Days, 4.-5.9.2012, Pyhäjärvi

LENA simulations for high-energy neutrinos,
EMMA Days, 25.-26.4.2012, Pyhäjärvi

FYSH370 Astroparticle Physics Course,
EMMA Scientific Advisory Board meeting, 3.-5.5.2011, Pyhäjärvi

LAGUNA-sites: Reactor Background and Gamma-ray measurements,
EMMA Days, 5-6.2.2010, Pyhäjärvi

Bibliography

[1] Michael Wurm et al. The next-generation liquid-scintillator neutrino observatory LENA. *Astropart. Phys.*, 35:685–732, 2012.

[2] Fengpeng An et al. Neutrino Physics with JUNO. *J. Phys.*, G43(3):030401, 2016.

[3] R. Acciarri et al. Long-Baseline Neutrino Facility (LBNF) and Deep Underground Neutrino Experiment (DUNE). 2015.

[4] LAGUNA-LBNO Consortium. LAGUNA/LAGUNA-LBNO - Design of a pan-European infrastructure for Large Apparatus for Grand Unification, Neutrino Astrophysics, and Long Baseline Neutrino Oscillations, 2011-2105. [Online; accessed 30-June-2016].

[5] A. de Bellefon et al. MEMPHYS: A Large scale water Cerenkov detector at Frejus. 2006.

[6] A. Rubbia. Underground Neutrino Detectors for Particle and Astroparticle Science: The Giant Liquid Argon Charge Imaging ExpeRiment (GLACIER). *J. Phys. Conf. Ser.*, 171:012020, 2009.

[7] J.N. Abdurashitov et al. Solar neutrino flux measurements by the Soviet-American Gallium Experiment (SAGE) for half the 22 year solar cycle. *J.Exp.Theor.Phys.*, 95:181–193, 2002.

[8] W. Hampel et al. Final results of the Cr-51 neutrino source experiments in GALLEX. *Phys. Lett.*, B420:114–126, 1998.

[9] A. Aguilar-Arevalo et al. Evidence for neutrino oscillations from the observation of anti-neutrino(electron) appearance in a anti-neutrino(muon) beam. *Phys. Rev.*, D64:112007, 2001.

[10] A. A. Aguilar-Arevalo et al. Improved Search for $\bar{\nu}_\mu \to \bar{\nu}_e$ Oscillations in the MiniBooNE Experiment. *Phys. Rev. Lett.*, 110:161801, 2013.

[11] W. Pauli. Dear radioactive ladies and gentlemen. *Phys.Today*, 31N9:27, 1978.

[12] E. Fermi. Versuch einer theorie der β-strahlen. i. *Zeitschrift für Physik*, 88(3):161–177, 1934.

[13] C.L. Cowan, F. Reines, F.B. Harrison, H.W. Kruse, and A.D. McGuire. Detection of the free neutrino: A Confirmation. *Science*, 124:103–104, 1956.

[14] Abdus Salam and John Clive Ward. Electromagnetic and weak interactions. *Phys. Lett.*, 13:168–171, 1964.

[15] S. Weinberg. A model of leptons. *Phys. Rev. Lett.*, 19:1264–1266, 1967.

[16] F. Englert and R. Brout. Broken Symmetry and the Mass of Gauge Vector Mesons. *Phys. Rev. Lett.*, 13:321–323, 1964.

[17] Peter W. Higgs. Broken Symmetries and the Masses of Gauge Bosons. *Phys. Rev. Lett.*, 13:508–509, 1964.

[18] G. S. Guralnik, C. R. Hagen, and T. W. B. Kibble. Global Conservation Laws and Massless Particles. *Phys. Rev. Lett.*, 13:585–587, 1964.

[19] J. H. Christenson, J. W. Cronin, V. L. Fitch, and R. Turlay. Evidence for the 2π decay of the k_2^0 meson. *Phys. Rev. Lett.*, 13:138–140, 1964.

[20] Bernard Aubert et al. Measurement of CP violating asymmetries in B^0 decays to CP eigenstates. *Phys. Rev. Lett.*, 86:2515–2522, 2001.

[21] Kazuo Abe et al. Observation of large CP violation in the neutral B meson system. *Phys. Rev. Lett.*, 87:091802, 2001.

[22] M. Goldhaber, L. Grodzins, and A. W. Sunyar. Helicity of neutrinos. *Phys. Rev.*, 109:1015–1017, 1958.

[23] Y. Fukuda et al. Evidence for oscillation of atmospheric neutrinos. *Phys.Rev.Lett.*, 81:1562–1567, 1998.

[24] Peter Minkowski. $\mu \to e\gamma$ at a Rate of One Out of 10^9 Muon Decays? *Phys. Lett.*, B67:421–428, 1977.

[25] G. Danby, J. M. Gaillard, Konstantin A. Goulianos, L. M. Lederman, Nari B. Mistry, M. Schwartz, and J. Steinberger. Observation of High-Energy Neutrino Reactions and the Existence of Two Kinds of Neutrinos. *Phys. Rev. Lett.*, 9:36–44, 1962.

[26] K. Kodama et al. Observation of tau neutrino interactions. *Phys. Lett.*, B504:218–224, 2001.

[27] S. Schael et al. Precision electroweak measurements on the Z resonance. *Phys. Rept.*, 427:257–454, 2006.

[28] P. A. R. Ade et al. Planck 2015 results. XIII. Cosmological parameters. 2015.

[29] S. A. Fayans. Radiative Corrections and Recoil Effects in the Reaction $\bar{\nu}_e + P \to$

$N + e^+$ at Low-energies. (In Russian). *Sov. J. Nucl. Phys.*, 42:590, 1985. [Yad. Fiz.42,929(1985)].

[30] A. Ianni, D. Montanino, and F. L. Villante. How to observe ˆ8B solar neutrinos in liquid scintillator detectors [rapid communication]. *Physics Letters B*, 627:38–48, October 2005.

[31] B.T. Cleveland, Timothy Daily, Jr. Davis, Raymond, James R. Distel, Kenneth Lande, et al. Measurement of the solar electron neutrino flux with the Homestake chlorine detector. *Astrophys.J.*, 496:505–526, 1998.

[32] Y. Fukuda et al. Solar neutrino data covering solar cycle 22. *Phys.Rev.Lett.*, 77:1683–1686, 1996.

[33] M. Altmann et al. GNO solar neutrino observations: Results for GNO I. *Phys. Lett.*, B490:16–26, 2000.

[34] E. G. Adelberger et al. Solar fusion cross sections II: the pp chain and CNO cycles. *Rev. Mod. Phys.*, 83:195, 2011.

[35] John N. Bahcall and Carlos Pena-Garay. Solar models and solar neutrino oscillations. *New J. Phys.*, 6:63, 2004.

[36] R. M. Bionta, G. Blewitt, C. B. Bratton, D. Casper, A. Ciocio, R. Claus, B. Cortez, M. Crouch, S. T. Dye, S. Errede, G. W. Foster, W. Gajewski, K. S. Ganezer, M. Goldhaber, T. J. Haines, T. W. Jones, D. Kielczewska, W. R. Kropp, J. G. Learned, J. M. LoSecco, J. Matthews, R. Miller, M. S. Mudan, H. S. Park, L. R. Price, F. Reines, J. Schultz, S. Seidel, E. Shumard, D. Sinclair, H. W. Sobel, J. L. Stone, L. R. Sulak, R. Svoboda, G. Thornton, J. C. van der Velde, and C. Wuest. Observation of a neutrino burst in coincidence with supernova 1987a in the large magellanic cloud. *Phys. Rev. Lett.*, 58:1494–1496, Apr 1987.

[37] K. Hirata, T. Kajita, M. Koshiba, M. Nakahata, Y. Oyama, N. Sato, A. Suzuki, M. Takita, Y. Totsuka, T. Kifune, T. Suda, K. Takahashi, T. Tanimori, K. Miyano, M. Yamada, E. W. Beier, L. R. Feldscher, S. B. Kim, A. K. Mann, F. M. Newcomer, R. Van, W. Zhang, and B. G. Cortez. Observation of a neutrino burst from the supernova sn1987a. *Phys. Rev. Lett.*, 58:1490–1493, Apr 1987.

[38] E. N. Alekseev, L. N. Alekseeva, V. I. Volchenko, and I. V. Krivosheina. Possible detection of a neutrino signal on 23 february 1987 at the baksan underground scintillation telescope of the institute of nuclear research. *JETP Lett.*, 45:589–592, 1987. [Pisma Zh. Eksp. Teor. Fiz. 45, 461-464 (1987)].

[39] T. Totani, K. Sato, H. E. Dalhed, and J. R. Wilson. Future detection of

supernova neutrino burst and explosion mechanism. *Astrophys. J.*, 496:216–225, 1998.

[40] Shin'ichiro Ando and Katsuhiko Sato. Relic neutrino background from cosmological supernovae. *New J. Phys.*, 6:170, 2004.

[41] K. Bays et al. Supernova Relic Neutrino Search at Super-Kamiokande. *Phys. Rev.*, D85:052007, 2012.

[42] K.A. Olive and Particle Data Group. Review of particle physics. *Chinese Physics C*, 38(9):090001, 2014.

[43] Rikard Enberg, Mary Hall Reno, and Ina Sarcevic. Prompt neutrino fluxes from atmospheric charm. *Phys. Rev.*, D78:043005, 2008.

[44] M. Sajjad Athar, M. Honda, T. Kajita, K. Kasahara, and S. Midorikawa. Atmospheric neutrino flux at INO, South Pole and Pyhasalmi. *Phys. Lett.*, B718:1375–1380, 2013.

[45] M. G. Aartsen et al. Evidence for Astrophysical Muon Neutrinos from the Northern Sky with IceCube. *Phys. Rev. Lett.*, 115(8):081102, 2015.

[46] A. Avrorin et al. The gigaton volume detector in Lake Baikal. *Nucl. Instrum. Meth.*, A639:30–32, 2011.

[47] P. Bagley et al. KM3NeT: Technical Design Report for a Deep-Sea Research Infrastructure in the Mediterranean Sea Incorporating a Very Large Volume Neutrino Telescope. 2009.

[48] Teppei Katori. MicroBooNE, A Liquid Argon Time Projection Chamber (LArTPC) Neutrino Experiment. *AIP Conf. Proc.*, 1405:250–255, 2011.

[49] D. S. Ayres et al. The NOvA Technical Design Report. 2007.

[50] K. Abe et al. Indication of Electron Neutrino Appearance from an Accelerator-produced Off-axis Muon Neutrino Beam. *Phys. Rev. Lett.*, 107:041801, 2011.

[51] M. Antonello et al. A Proposal for a Three Detector Short-Baseline Neutrino Oscillation Program in the Fermilab Booster Neutrino Beam. 2015.

[52] G. Tzanankos et al. MINOS+: a Proposal to FNAL to run MINOS with the medium energy NuMI beam. 2011.

[53] L. Aliaga et al. Design, Calibration, and Performance of the MINERvA Detector. *Nucl. Instrum. Meth.*, A743:130–159, 2014.

[54] S. K. Agarwalla et al. The mass-hierarchy and CP-violation discovery reach of the LBNO long-baseline neutrino experiment. *JHEP*, 05:094, 2014.

[55] P. Zucchelli. A novel concept for a anti-nu/e / nu/e neutrino factory: The beta beam. *Phys. Lett.*, B532:166–172, 2002.

[56] M. Benedikt, A. Bechtold, F. Borgnolutti, E. Bouquerel, L. Bozyk, J. Bruer, A. Chancé, P. Delahaye, A. Fabich, S. Hancock, C. Hansen, E. Jensen, A. Källberg, M. Kirk, A. Lachaize, M. Lindroos, M. Loiselet, M. Magistris, S. Mitrofanov, A. C. Mueller, J. Payet, H. Podlech, P. Puppel, M. Silari, A. Simonsson, P. Spiller, J. Stadlmann, T. Stora, A. Tkatchenko, S. Trovati, V. Vlachoudis, and E. Wildner. Conceptual design report for a beta-beam facility. *The European Physical Journal A*, 47(2):1–32, 2011.

[57] Jean-Eric Campagne, M. Maltoni, M. Mezzetto, and T. Schwetz. Physics potential of the CERN-MEMPHYS neutrino oscillation project. *JHEP*, 04:003, 2007.

[58] S. Geer. Neutrino beams from muon storage rings: Characteristics and physics potential. *Phys. Rev. D*, 57:6989–6997, Jun 1998.

[59] S. Choubey et al. International Design Study for the Neutrino Factory, Interim Design Report. 2011.

[60] Steve Geer, Olga Mena, and Silvia Pascoli. A Low energy neutrino factory for large θ_{13}. *Phys. Rev.*, D75:093001, 2007.

[61] B. Pontecorvo. Mesonium and anti-mesonium. *Sov. Phys. JETP*, 6:429, 1957. [Zh. Eksp. Teor. Fiz.33,549(1957)].

[62] Q. R. Ahmad et al. Direct evidence for neutrino flavor transformation from neutral current interactions in the Sudbury Neutrino Observatory. *Phys. Rev. Lett.*, 89:011301, 2002.

[63] Ziro Maki, Masami Nakagawa, and Shoichi Sakata. Remarks on the unified model of elementary particles. *Prog.Theor.Phys.*, 28:870–880, 1962.

[64] F.P. An et al. Observation of electron-antineutrino disappearance at Daya Bay. *Phys.Rev.Lett.*, 108:171803, 2012.

[65] Soo-Bong Kim. New results from RENO and prospects with RENO-50. In *Neutrino Oscillation Workshop (NOW 2014) Conca Specchiulla, Otranto, Lecce, Italy, September 7-14, 2014*, 2014.

[66] Y. Abe et al. Improved measurements of the neutrino mixing angle θ_{13} with the Double Chooz detector. *JHEP*, 10:086, 2014. [Erratum: JHEP02,074(2015)].

[67] S. P. Mikheev and A. Yu. Smirnov. Resonance Amplification of Oscillations in Matter and Spectroscopy of Solar Neutrinos. *Sov. J. Nucl. Phys.*, 42:913–917, 1985. [Yad. Fiz.42,1441(1985)].

[68] L. Wolfenstein. Neutrino Oscillations in Matter. *Phys. Rev.*, D17:2369–2374, 1978.

[69] Patrick Huber, M. Lindner, and W. Winter. Simulation of long-baseline neutrino oscillation experiments with GLoBES (General Long Baseline Experiment Simulator). *Comput. Phys. Commun.*, 167:195, 2005.

[70] Patrick Huber, Joachim Kopp, Manfred Lindner, Mark Rolinec, and Walter Winter. New features in the simulation of neutrino oscillation experiments with GLoBES 3.0: General Long Baseline Experiment Simulator. *Comput. Phys. Commun.*, 177:432–438, 2007.

[71] Adam M. Dziewonski and Don L. Anderson. Preliminary reference earth model. *Physics of the Earth and Planetary Interiors*, 25(4):297 – 356, 1981.

[72] F. D. Stacey. *Physics of the Earth*. Brookfield Press, Brisbane, Australia, 1992.

[73] M. G. Aartsen et al. Letter of Intent: The Precision IceCube Next Generation Upgrade (PINGU). 2014.

[74] U. F. Katz. The ORCA Option for KM3NeT. *ArXiv e-prints*, February 2014.

[75] Moon Moon Devi, Tarak Thakore, Sanjib Kumar Agarwalla, and Amol Dighe. Enhancing sensitivity to neutrino parameters at INO combining muon and hadron information. *JHEP*, 10:189, 2014.

[76] K. Abe et al. Letter of Intent: The Hyper-Kamiokande Experiment — Detector Design and Physics Potential —. 2011.

[77] Liang Zhan, Yifang Wang, Jun Cao, and Liangjian Wen. Determination of the Neutrino Mass Hierarchy at an Intermediate Baseline. *Phys. Rev.*, D78:111103, 2008.

[78] Yu-Feng Li, Jun Cao, Yifang Wang, and Liang Zhan. Unambiguous Determination of the Neutrino Mass Hierarchy Using Reactor Neutrinos. *Phys. Rev.*, D88:013008, 2013.

[79] Liang Zhan, Yifang Wang, Jun Cao, and Liangjian Wen. Experimental Requirements to Determine the Neutrino Mass Hierarchy Using Reactor Neutrinos. *Phys. Rev.*, D79:073007, 2009.

[80] E. Kh. Akhmedov, Soebur Razzaque, and A. Yu. Smirnov. Mass hierarchy, 2-3 mixing and CP-phase with Huge Atmospheric Neutrino Detectors. *JHEP*, 02:082, 2013. [Erratum: JHEP07,026(2013)].

[81] C. Adams et al. The Long-Baseline Neutrino Experiment: Exploring Fundamental Symmetries of the Universe. 2013.

[82] Cecilia Lunardini and Alexei Yu. Smirnov. Probing the neutrino mass hierarchy and the 13 mixing with supernovae. *JCAP*, 0306:009, 2003.

[83] Huaiyu Duan, George M. Fuller, J. Carlson, and Yong-Zhong Qian. Neutrino Mass Hierarchy and Stepwise Spectral Swapping of Supernova Neutrino Flavors. *Phys. Rev. Lett.*, 99:241802, 2007.

[84] Pasquale D. Serpico, Sovan Chakraborty, Tobias Fischer, Lorenz Hüdepohl, Hans-Thomas Janka, and Alessandro Mirizzi. Probing the neutrino mass hierarchy with the rise time of a supernova burst. *Phys. Rev. D*, 85:085031, Apr 2012.

[85] A. Gando et al. Search for Majorana Neutrinos near the Inverted Mass Hierarchy Region with KamLAND-Zen. 2016.

[86] C. Cuesta et al. Status of the MAJORANA DEMONSTRATOR. *AIP Conf. Proc.*, 1686:020005, 2015.

[87] K. H. Ackermann et al. The GERDA experiment for the search of $0\nu\beta\beta$ decay in ^{76}Ge. *Eur. Phys. J.*, C73(3):2330, 2013.

[88] W. Zhao et al. First results on low-mass WIMPs from the CDEX-1 experiment at the China Jinping underground laboratory. *Phys. Rev.*, D88(5):052004, 2013.

[89] Joachim Ebert et al. Results of a search for neutrinoless double-beta decay using the COBRA demonstrator. 2015.

[90] S. Umehara et al. CANDLES. *EPJ Web Conf.*, 66:08008, 2014.

[91] V. Alenkov et al. Technical Design Report for the AMoRE $0\nu\beta\beta$ Decay Search Experiment. 2015.

[92] T. Shima, P.J. Doe, H. Ejiri, S.R. Elliot, J. Engel, et al. Moon for a next-generation neutrino-less double-beta decay experiment: Present status and perspective. *J.Phys.Conf.Ser.*, 120:052055, 2008.

[93] J. B. Albert et al. Improved measurement of the $2\nu\beta\beta$ half-life of ^{136}Xe with the EXO-200 detector. *Phys. Rev.*, C89(1):015502, 2014.

[94] J. J. Gomez-Cadenas et al. Present status and future perspectives of the NEXT experiment. *Adv. High Energy Phys.*, 2014:907067, 2014.

[95] XiGuang Cao et al. PandaX: A Liquid Xenon Dark Matter Experiment at CJPL. *Sci. China Phys. Mech. Astron.*, 57:1476–1494, 2014.

[96] A. Gando et al. Limit on Neutrinoless $\beta\beta$ Decay of ^{136}Xe from the First Phase of KamLAND-Zen and Comparison with the Positive Claim in ^{76}Ge. *Phys. Rev. Lett.*, 110(6):062502, 2013.

[97] A. S. Barabash. SeperNEMO double beta decay experiment. *J. Phys. Conf. Ser.*, 375:042012, 2012.

[98] D. R. Artusa et al. Searching for neutrinoless double-beta decay of ^{130}Te with CUORE. *Adv. High Energy Phys.*, 2015:879871, 2015.

[99] G. Wang et al. CUPID: CUORE (Cryogenic Underground Observatory for Rare Events) Upgrade with Particle IDentification. 2015.

[100] S. Andringa et al. Current Status and Future Prospects of the SNO+ Experiment. *Adv. High Energy Phys.*, 2016:6194250, 2015.

[101] Alessandro Strumia and Francesco Vissani. Implications of neutrino data circa 2005. *Nucl. Phys.*, B726:294–316, 2005.

[102] J. Angrik et al. KATRIN design report 2004. 2005.

[103] Benjamin Monreal and Joseph A. Formaggio. Relativistic Cyclotron Radiation Detection of Tritium Decay Electrons as a New Technique for Measuring the Neutrino Mass. *Phys. Rev.*, D80:051301, 2009.

[104] M. Faverzani et al. The HOLMES Experiment. *J. Low. Temp. Phys.*, 184(3-4):922–929, 2016.

[105] C. Aberle et al. Whitepaper on the DAEdALUS Program. In *Community Summer Study 2013: Snowmass on the Mississippi (CSS2013) Minneapolis, MN, USA, July 29-August 6, 2013*, 2013.

[106] O. Adriani et al. Determination of the number of light neutrino species. *Phys. Lett.*, B292:463–471, 1992.

[107] W. Hampel et al. GALLEX solar neutrino observations: Results for GALLEX IV. *Phys.Lett.*, B447:127–133, 1999.

[108] J.N. Abdurashitov, E.L. Faizov, V.N. Gavrin, A.O. Gusev, A.V. Kalikhov, T.V. Knodel, I.I. Knyshenko, V.N. Kornoukhov, I.N. Mirmov, A.M. Pshukov, A.M. Shalagin, A.A. Shikhin, P.V. Timofeyev, E.P. Veretenkin, V.M. Vermul, G.T. Zatsepin, T.J. Bowles, J.S. Nico, W.A. Teasdale, D.L. Wark, J.F. Wilkerson, B.T. Cleveland, T. Daily, R. Davis, K. Lande, C.K. Lee, P.W. Wildenhain, S.R. Elliott, M.L. Cherry, and R.T. Kouzes. Results from sage (the russian-american gallium solar neutrino experiment). *Physics Letters B*, 328(1):234 – 248, 1994.

[109] J. N. Abdurashitov et al. Measurement of the response of a Ga solar neutrino experiment to neutrinos from an Ar-37 source. *Phys. Rev.*, C73:045805, 2006.

[110] G. Mention, M. Fechner, Th. Lasserre, Th. A. Mueller, D. Lhuillier, M. Cribier, and A. Letourneau. The Reactor Antineutrino Anomaly. *Phys. Rev.*, D83:073006, 2011.

[111] B. Armbruster et al. Upper limits for neutrino oscillations muon-anti-neutrino —> electron-anti-neutrino from muon decay at rest. *Phys. Rev.*, D65:112001, 2002.

[112] K. Abe et al. Search for short baseline ν_e disappearance with the T2K near detector. *Phys. Rev.*, D91:051102, 2015.

[113] Davide Meloni, Jian Tang, and Walter Winter. Sterile neutrinos beyond LSND at the Neutrino Factory. *Phys. Rev.*, D82:093008, 2010.

[114] Carlo Giunti and Marco Laveder. Implications of 3+1 Short-Baseline Neutrino Oscillations. *Phys. Lett.*, B706:200–207, 2011.

[115] D. Adey et al. nuSTORM - Neutrinos from STORed Muons: Proposal to the Fermilab PAC. 2013.

[116] M. Elnimr et al. The OscSNS White Paper. In *Community Summer Study 2013: Snowmass on the Mississippi (CSS2013) Minneapolis, MN, USA, July 29-August 6, 2013*, 2013.

[117] Andi S. Cucoanes. Status of the Nucifer experiment. *J. Phys. Conf. Ser.*, 375:042063, 2012.

[118] V. Hélaine. Sterile neutrino search at the ILL nuclear reactor: the STEREO experiment. In *NuPhys2015: Prospects in Neutrino Physics (NuPhys) London, UK, December 16-18, 2015*, 2016.

[119] I. Alekseev et al. DANSS: Detector of the reactor AntiNeutrino based on Solid Scintillator. 2016.

[120] G. Bellini et al. SOX: Short distance neutrino Oscillations with BoreXino. *JHEP*, 08:038, 2013.

[121] K. Eguchi et al. First results from KamLAND: Evidence for reactor anti-neutrino disappearance. *Phys.Rev.Lett.*, 90:021802, 2003.

[122] G. Alimonti et al. The Borexino detector at the Laboratori Nazionali del Gran Sasso. *Nucl. Instrum. Meth.*, A600:568–593, 2009.

[123] C. Athanassopoulos et al. The Liquid scintillator neutrino detector and LAMPF neutrino source. *Nucl. Instrum. Meth.*, A388:149–172, 1997.

[124] Y. Abe et al. Reactor electron antineutrino disappearance in the Double Chooz experiment. *Phys.Rev.*, D86:052008, 2012.

[125] J.K. Ahn et al. Observation of Reactor Electron Antineutrino Disappearance in the RENO Experiment. *Phys.Rev.Lett.*, 108:191802, 2012.

[126] H. M. O'Keeffe, E. O'Sullivan, and M. C. Chen. Scintillation decay time and

pulse shape discrimination in oxygenated and deoxygenated solutions of linear alkylbenzene for the SNO+ experiment. *Nucl. Instrum. Meth.*, A640:119–122, 2011.

[127] G. Bellini et al. Final results of Borexino Phase-I on low energy solar neutrino spectroscopy. *Phys. Rev.*, D89(11):112007, 2014.

[128] H. M. O'Keeffe, E. O'Sullivan, and M. C. Chen. Scintillation decay time and pulse shape discrimination in oxygenated and deoxygenated solutions of linear alkylbenzene for the SNO+ experiment. *Nuclear Instruments and Methods in Physics Research A*, 640:119–122, June 2011.

[129] Dominikus Hellgartner. *Advanced Event Reconstruction in LENA and Precision Attenuation-Length Measurements in Liquid Scintillators*. PhD thesis, Munich, Tech. U., 2015.

[130] T. Araki et al. Experimental investigation of geologically produced antineutrinos with KamLAND. *Nature*, 436:499–503, 2005.

[131] G. Bellini et al. Observation of Geo-Neutrinos. *Phys. Lett.*, B687:299–304, 2010.

[132] G. Bellini et al. Precision measurement of the ^{7}Be solar neutrino interaction rate in borexino. *Phys. Rev. Lett.*, 107:141302, 2011.

[133] G. Bellini et al. First evidence of pep solar neutrinos by direct detection in borexino. *Phys. Rev. Lett.*, 108:051302, 2012.

[134] Borexino Collaboration. Neutrinos from the primary proton-proton fusion process in the sun. *Nature*, 512(7515):383–386, 08 2014.

[135] M. Yeh, S. Hans, W. Beriguete, R. Rosero, L. Hu, R. L. Hahn, M. V. Diwan, D. E. Jaffe, S. H. Kettell, and L. Littenberg. A new water-based liquid scintillator and potential applications. *Nucl. Instrum. Meth.*, A660:51–56, 2011.

[136] Gabriel D. Orebi Gann. Physics Potential of an Advanced Scintillation Detector: Introducing THEIA. 2015.

[137] J. R. Alonso et al. Advanced Scintillator Detector Concept (ASDC): A Concept Paper on the Physics Potential of Water-Based Liquid Scintillator. 2014.

[138] Randolph Mollenberg. *Monte Carlo Study of Solar ^{8}B Neutrinos and the Diffuse Supernova Neutrino Background in LENA*. PhD thesis, Munich, Tech. U., 2013.

[139] J. Brack et al. Characterization of the Hamamatsu R11780 12 inch Photomultiplier Tube. *Nucl. Instrum. Meth.*, A712:162–173, 2013.

[140] W. H. Trzaska et al. Advantages of locating LAGUNA in Pyhaesalmi mine. *Prog. Part. Nucl. Phys.*, 66:463–467, 2011.

[141] W. H. Trzaska et al. LAGUNA in Pyhaesalmi. *Acta Phys. Polon.*, B41:1779–1788, 2010.

[142] W. H. Trzaska. Site selection for the new generation of giant neutrino detectors. *J. Phys. Conf. Ser.*, 375:042060, 2012.

[143] W. H. Trzaska. Will Finland Become the Center of European Neutrino Physics? In Y. E. Penionzhkevich and Y. G. Sobolev, editors, *Exotic Nuclei: EXON-2012 - Proceedings of the International Symposium. Edited by Penionzhkevich Yu E, Sobolev Yu G. Published by World Scientific Publishing Co. Pte. Ltd., 2013. ISBN #9789814508865, pp. 391-400*, pages 391–400, June 2013.

[144] Randolph Möllenberg, Franz von Feilitzsch, Dominikus Hellgartner, Lothar Oberauer, Marc Tippmann, Jürgen Winter, Michael Wurm, and Vincenz Zimmer. Detecting the Upturn of the Solar ^{8}B Neutrino Spectrum with LENA. *Phys. Lett.*, B737:251–255, 2014.

[145] E. Richard et al. Measurements of the atmospheric neutrino flux by Super-Kamiokande: energy spectra, geomagnetic effects, and solar modulation. 2015.

[146] Pran Nath and Pavel Fileviez Perez. Proton stability in grand unified theories, in strings and in branes. *Phys. Rept.*, 441:191–317, 2007.

[147] H. Nishino et al. Search for Proton Decay via p —> e+ pi0 and p —> mu+ pi0 in a Large Water Cherenkov Detector. *Phys. Rev. Lett.*, 102:141801, 2009.

[148] K. Kobayashi et al. Search for nucleon decay via modes favored by supersymmetric grand unification models in Super-Kamiokande-I. *Phys. Rev.*, D72:052007, 2005.

[149] Teresa Marrodán Undagoitia. *Measurement of light emission in organic liquid scintillators and studies towards the search for proton decay in the future large-scale detector LENA*. PhD thesis, Munich, Tech. U., 2008.

[150] S. Agostinelli, J. Allison, K. Amako, J. Apostolakis, H. Araujo, P. Arce, M. Asai, D. Axen, S. Banerjee, G. Barrand, F. Behner, L. Bellagamba, J. Boudreau, L. Broglia, A. Brunengo, H. Burkhardt, S. Chauvie, J. Chuma, R. Chytracek, G. Cooperman, G. Cosmo, P. Degtyarenko, A. Dell'Acqua, G. Depaola, D. Dietrich, R. Enami, A. Feliciello, C. Ferguson, H. Fesefeldt, G. Folger, F. Foppiano, A. Forti, S. Garelli, S. Giani, R. Giannitrapani, D. Gibin, J.J. Gómez Cadenas, I. González, G. Gracia Abril, G. Greeniaus, W. Greiner, V. Grichine, A. Grossheim, S. Guatelli, P. Gumplinger, R. Hamatsu, K. Hashimoto, H. Hasui, A. Heikkinen, A. Howard, V. Ivanchenko, A. Johnson, F.W. Jones, J. Kallenbach, N. Kanaya, M. Kawabata, Y. Kawabata, M. Kawaguti, S. Kelner, P. Kent,

A. Kimura, T. Kodama, R. Kokoulin, M. Kossov, H. Kurashige, E. Lamanna, T. Lampén, V. Lara, V. Lefebure, F. Lei, M. Liendl, W. Lockman, F. Longo, S. Magni, M. Maire, E. Medernach, K. Minamimoto, P. Mora de Freitas, Y. Morita, K. Murakami, M. Nagamatu, R. Nartallo, P. Nieminen, T. Nishimura, K. Ohtsubo, M. Okamura, S. O'Neale, Y. Oohata, K. Paech, J. Perl, A. Pfeiffer, M.G. Pia, F. Ranjard, A. Rybin, S. Sadilov, E. Di Salvo, G. Santin, T. Sasaki, N. Savvas, Y. Sawada, S. Scherer, S. Sei, V. Sirotenko, D. Smith, N. Starkov, H. Stoecker, J. Sulkimo, M. Takahata, S. Tanaka, E. Tcherniaev, E. Safai Tehrani, M. Tropeano, P. Truscott, H. Uno, L. Urban, P. Urban, M. Verderi, A. Walkden, W. Wander, H. Weber, J.P. Wellisch, T. Wenaus, D.C. Williams, D. Wright, T. Yamada, H. Yoshida, and D. Zschiesche. Geant4?a simulation toolkit. *Nuclear Instruments and Methods in Physics Research Section A: Accelerators, Spectrometers, Detectors and Associated Equipment*, 506(3):250 – 303, 2003.

[151] H. Kwon, F. Boehm, A. A. Hahn, H. E. Henrikson, J. L. Vuilleumier, J. F. Cavaignac, D. H. Koang, B. Vignon, F. v. Feilitzsch, and R. L. Mössbauer. Search for neutrino oscillations at a fission reactor. *Phys. Rev. D*, 24:1097–1111, Sep 1981.

[152] G. Zacek et al. Neutrino Oscillation Experiments at the Gosgen Nuclear Power Reactor. *Phys. Rev.*, D34:2621–2636, 1986.

[153] A.A. Kuvshinnikov, L.A. Mikaelyan, S.V. Nikolaev, M.D. Skorokhvatov, and A.V. Etenko. Measuring the $\bar{\nu}_e + p \to n + e^+$ cross-section and beta decay axial constant in a new experiment at rovno npp reactor. *JETP Lett.*, 54:253–257, 1991.

[154] G. S. Vidyakin et al. Limitations on the characteristics of neutrino oscillations. *JETP Lett.*, 59:390–393, 1994.

[155] Z. D. Greenwood et al. Results of a two position reactor neutrino oscillation experiment. *Phys. Rev.*, D53:6054–6064, 1996.

[156] Y. Declais et al. Study of reactor anti-neutrino interaction with proton at Bugey nuclear power plant. *Phys. Lett.*, B338:383–389, 1994.

[157] B. Achkar et al. Search for neutrino oscillations at 15-meters, 40-meters, and 95-meters from a nuclear power reactor at bugey. *Nucl. Phys.*, B434:503–534, 1995.

[158] M. Apollonio et al. Search for neutrino oscillations on a long baseline at the CHOOZ nuclear power station. *Eur. Phys. J.*, C27:331–374, 2003.

[159] A. Gando et al. Enhanced constraints on θ_{13} from a three-flavor oscillation analysis of reactor antineutrinos at kamland. *Phys. Rev.*, D83:052002, 2011.

[160] F. P. An et al. New Measurement of Antineutrino Oscillation with the Full Detector Configuration at Daya Bay. *Phys. Rev. Lett.*, 115(11):111802, 2015.

[161] V. Kopeikin, L. Mikaelyan, and V. Sinev. Components of antineutrino emission in nuclear reactor. *Phys. Atom. Nucl.*, 67:1963, 2004. 4th International Conference on Nonaccelerator New Physics (NANP 03), Dubna, Russia, 23-28 June 2003.

[162] V. Kopeikin, L. Mikaelyan, and V. Sinev. Reactor as a source of antineutrinos: Thermal fission energy. *Phys. Atom. Nucl.*, 67:1892–1899, 2004. [Yad. Fiz.67,1916(2004)].

[163] X. B. Ma, W. L. Zhong, L. Z. Wang, Y. X. Chen, and J. Cao. Improved calculation of the energy release in neutron-induced fission. *Phys. Rev.*, C88(1):014605, 2013.

[164] Marica Baldoncini, Ivan Callegari, Giovanni Fiorentini, Fabio Mantovani, Barbara Ricci, Virginia Strati, and Gerti Xhixha. Reference worldwide model for antineutrinos from reactors. *Phys. Rev.*, D91(6):065002, 2015.

[165] G. Bellini et al. Measurement of geo-neutrinos from 1353 days of Borexino. *Phys. Lett.*, B722:295–300, 2013.

[166] Th. A. Mueller et al. Improved Predictions of Reactor Antineutrino Spectra. *Phys. Rev.*, C83:054615, 2011.

[167] F.P. An et al. Improved measurement of the reactor antineutrino flux and spectrum at daya bay. 2016.

[168] Hyunkwan Seo. Recent result from reno. *J. Phys. Conf. Ser.*, 718(6):062053, 2016. TAUP 2015.

[169] Gianni Fiorentini, Marcello Lissia, and Fabio Mantovani. Geo-neutrinos and Earth's interior. *Phys. Rept.*, 453:117–172, 2007.

[170] J. H. Davies and D. R. Davies. Earth's surface heat flux. *Solid Earth*, 1(1):5–24, 2010.

[171] A. Gando et al. Reactor On-Off Antineutrino Measurement with KamLAND. *Phys. Rev.*, D88(3):033001, 2013.

[172] M. Agostini et al. Spectroscopy of geoneutrinos from 2056 days of Borexino data. *Phys. Rev.*, D92(3):031101, 2015.

[173] V. Strati, M. Baldoncini, I. Callegari, F. Mantovani, W. F. McDonough, B. Ricci, and G. Xhixha. Expected geoneutrino signal at JUNO. *Progress in Earth and Planetary Science*, 2:5, December 2015.

[174] Y. Huang, V. Chubakov, F. Mantovani, R. L. Rudnick, and W. F. McDonough.

A reference Earth model for the heat producing elements and associated geoneutrino flux. *ArXiv e-prints*, January 2013.

[175] John G. Learned, Stephen T. Dye, and Sandip Pakvasa. Hanohano: A Deep ocean anti-neutrino detector for unique neutrino physics and geophysics studies. In *Neutrino telescopes. Proceedings, 12th International Workshop, Venice, Italy, March 6-9, 2007*, pages 235–269, 2007.

[176] K. K. Loo, N. Yu Novikov, M. V. Smirnov, W. H. Trzaska, and M. Wurm. Omnibus experiment: CPT and CP violation with sterile neutrinos. *J. Phys. Conf. Ser.*, 718(6):062063, 2016.

[177] Yu. N. Novikov et al. Neutrino oscillometry at the next generation neutrino observatory. 2011.

[178] J. D. Vergados, Y. Giomataris, and Yu. N. Novikov. Probing the fourth neutrino existence by neutral current oscillometry in the spherical gaseous TPC. *Nucl. Phys.*, B854:54–66, 2012.

[179] K. Loo, T. Enqvist, J. Hissa, D. Nesterenko, Yu. N. Novikov, W. H. Trzaska, J. Vergados, and M. Wurm. Hunt for Theta(13) with LENA. *J. Phys. Conf. Ser.*, 375:042053, 2012.

[180] Michail V. Smirnov, Kai K. Loo, Yuri N. Novikov, Wladyslaw H. Trzaska, and Michael Wurm. A search for neutrino?antineutrino mass inequality by means of sterile neutrino oscillometry. *Nucl. Phys.*, B900:104–114, 2015.

[181] ROOT Mathematical Libraries: Minuit2 Minuit2 Minimization Package.

[182] Donald E. Groom, Nikolai V. Mokhov, and Sergei I. Striganov. Muon stopping power and range tables 10-MeV to 100-TeV. *Atom. Data Nucl. Data Tabl.*, 78:183–356, 2001.

[183] M. Abs et al. Multimegawatt DAEδALUS Cyclotrons for Neutrino Physics. 2012.